High-precision multidynamic Sr isotope analysis using thermal ionization mass spectrometer (TIMS) with correction of fractionation drift

Yankun Di*, Evgenii Krestianinov, Sonja Zink, Yuri Amelin

Research School of Earth Sciences, Australian National University, Acton, ACT 2601, Australia

*Corresponding author, email: yankun.di@anu.edu.au

Submitted to *Chemical Geology*

Abstract

High-precision and high-accuracy measurement of the natural mass-independent variations of $^{84}Sr/^{86}Sr$ using thermal ionization mass spectrometry (TIMS) is crucial for understanding the planetary volatile depletion history and the heterogeneous isotopic reservoirs in the early Solar System. The recently reported $\mu^{84}Sr$ values [defined as $10^6\times(^{84}Sr/^{86}Sr_{\mathrm{sample}}/^{84}Sr/^{86}Sr_{\mathrm{standard}} - 1)$] for terrestrial rock samples, however, show a significant discrepancy between static and multidynamic TIMS measurement results, indicating that the data from one or both measurement methods are biased by analytical artefacts. Coupled with this issue, the accurate $\mu^{84}Sr$ values of terrestrial samples are also under debate. Here we present high-precision $^{84}Sr/^{86}Sr$ and $^{87}Sr/^{86}Sr$ data for a series of natural samples and the standard NIST SRM 987 measured using a new 3-line multidynamic TIMS method, with the aims to: (1) systematically evaluate and correct the fractionation drift effect in multidynamic Sr isotope measurements, (2) investigate the origin of the discrepancy between the $\mu^{84}Sr$ values derived from static and multidynamic measurements, and (3) determine the accurate terrestrial $\mu^{84}Sr$ value. Our data show that the rapid drift of isotopic fractionation during measurement can significantly bias the multidynamic $^{84}Sr/^{86}Sr$ ratio, but has only minor influence on $^{87}Sr/^{86}Sr$. The previously observed static vs. multidynamic $\mu^{84}Sr$ discrepancy has been reproduced in our study, and can be explained by the positive biases of multidynamic $\mu^{84}Sr$ caused by the high fractionation rates of terrestrial samples compared to the standard. After correcting the fractionation drift effect using a linear interpolation method, the average multidynamic $\mu^{84}Sr$ value of the terrestrial samples is in complete agreement with the multistatic result. We confirm that the standard NIST SRM 987 possesses an apparent ^{84}Sr enrichment relative to the natural samples from the Earth, and conclude that the terrestrial samples have an average $\mu^{84}Sr$ value of –31 ± 8 ppm (2 standard error). The fractionation drift-corrected multidynamic $\mu^{87}Sr$ and $\mu^{84}Sr$ results of SRM 987 show a pronounced correlation that is likely to be a combined effect of ion counting random error, uncorrected (or overcorrected) fractionation drift effect, and mixing of Sr ions evaporated from variably fractionated sample reservoirs on the filament. The two independent multidynamic $^{87}Sr/^{86}Sr$ ratios returned by our method exhibit a stable, small but resolvable offset, which most likely reflects systematic errors generated by an insufficient amplifier idle time setting. Our measurement method has also been applied to three standard materials that have been used in the early Solar System $^{87}Sr/^{86}Sr$ chronology studies from the 1970s till present to examine the reliability of the normalization method used for inter-laboratory comparison and to assure accurate cross-calibration of these standards.

Keywords

Strontium isotope, thermal ionization mass spectrometry, multidynamic measurement, isotope fractionation

1. Introduction

For many elements with important geochemistry and cosmochemistry applications (e.g., Ca, Cr, Sr, Ba, Nd, W, Os, Pb), thermal ionization mass spectrometry (TIMS) is the most favourable technique to determine isotopic ratios at part-per-million (ppm) precision level (Carlson, 2014; Wieser and Schwieters, 2005; Makishima, 2016). The most widely used isotope analysis method of TIMS is the static multi-collection method, in which the magnetic field setting of the analyser is set to a fixed value, while the ion beams with different mass/charge ratios separated by the analyser are simultaneously collected and measured by an array of multiple detectors (Faraday cups connected to electrometer amplifiers). In static multi-collection measurements, the detection efficiency can slightly differ between the multiple Faraday cups due to the generation and escape of secondary charged particles when the ion beam hits the cup (Makishima and Nakamura, 1991), and these differences can introduce systematic errors into measured isotopic ratios. If the efficiencies of the Faraday cups remain constant, these systematic biases can be corrected by sample–standard comparison (Garçon et al., 2018; Carlson, 2014; Yokoyama et al., 2015; Albarède et al., 2004). However, many studies have reported drifts of Faraday cup efficiencies (also known as Faraday cup deterioration) in time scales from weeks to years during the isotopic analyses of Sr, Ba, Nd, Pb, and W (Thirlwall, 1991; Makishima and Nakamura, 1991; Thirlwall and Anczkiewicz, 2004; Fukai et al., 2017; Garçon et al., 2018; Yobregat et al., 2017; Archer et al., 2017; Fukami et al., 2017; Miyazaki et al., 2016; Carlson, 2014; Roth et al., 2013; Yokoyama et al., 2015). As Faraday cups deteriorate, the repetitively measured isotopic ratios of standards show systematic drifts or cyclic fluctuations, making precise and accurate standardization of the analyses of unknown samples difficult or impossible.

The problem caused by Faraday cup deterioration can be solved by applying a dynamic multi-collection (or “multidynamic”) measurement method (Lenz and Wendt, 1976). With the cup positions fixed but the magnetic field settings (called “lines”) dynamically switched within a measurement cycle, the isotopic ratio of interest and the isotopic ratio used to monitor mass fractionation can be sequentially measured using the same combination of Faraday cups, and hence most cup efficiency components can be mathematically cancelled during the fractionation correction procedure. The application of multidynamic methods can effectively improve long-term measurement precision compared to the static method (Garçon et al., 2018; Thirlwall, 1991; Fukai et al., 2017), although the required measurement time is sometimes longer (Ludwig, 1997). The multidynamic method has, however, several inherent problems of its own. In the instruments that are equipped with zoom optics to enable nearly perfect alignment of peaks in each line by changing the dispersion of the analyser, the measured isotopic ratios can be affected by the dependence of ion transmission on zoom settings

(Trinquier et al., 2008; Amelin and Huyskens, 2013). In the mass spectrometers without zoom optics, the peaks are inevitably misaligned in all lines of the multidynamic sequence except one, and the measured ratios are therefore influenced by the imperfections of peak top flatness (Thirlwall, 1991; Albarède et al., 2004). Biases caused by these problems are difficult to correct mathematically, but they could be addressed in the future improvements of the design of the ion optical systems.

Another intrinsic drawback of the multidynamic method is that the instrumental fractionation during measurement cannot be accurately corrected at real time. Given that the isotopic ratio of interest and the fractionation monitor ratio are measured in two different lines that are separated in time by a gap consisting of integration times and idle times, the fractionation-corrected isotopic ratios can be biased if the fractionation significantly changes during this time gap. The biases caused by this effect have long been supposed to be negligible, but the recent work by Roth et al. (2014) suggests that large fractionation drifts associated with high fractionation rates and prolonged time gaps can be a significant source of deteriorating accuracy and precision in multidynamic ^{142}Nd/^{144}Nd measurements. Unlike the problems described earlier, this effect can be managed by optimising data processing. This fractionation drift effect has been well recognized and corrected in the recent Nd isotope studies (e.g., Garçon et al., 2018; Horan et al., 2018), but how it affects the multidynamic analyses of other isotopic systems, such as Sr (^{84}Sr/^{86}Sr and ^{87}Sr/^{86}Sr), has not been investigated to the best of our knowledge.

Natural mass-independent variations of the ^{84}Sr/^{86}Sr ratio have been found in many extra-terrestrial materials, such as pre-solar silicon carbides (e.g., Podosek et al., 2004), Ca–Al-rich inclusions (e.g., Papanastassiou and Wasserburg, 1978; Moynier et al., 2012), and carbonaceous chondrites (e.g., Yokoyama et al., 2015). These variations are identified as isotopic anomalies relative to the bulk silicate Earth composition, and are thought to reflect the heterogeneous mixing of stellar dust of different nucleosynthetic origin at the early formation stages of the Solar System. The planet-scale $^{84}Sr/^{86}Sr$ heterogeneity may hold critical information regarding the planetary volatile depletion history (e.g., Hans et al., 2013), the genetic relation between the Solar System's earliest solids and later-formed materials (e.g., Burkhardt et al., 2019), as well as the injection and admixing of nucleosynthetic components from different stellar sources (e.g., Brennecka et al., 2013). Recent high-precision Sr isotope analyses using TIMS have achieved long-term $^{84}Sr/^{86}Sr$ precision better than 30 ppm using either a static or a multidynamic measurement method (Andreasen and Sharma, 2007; Moynier et al., 2012; Paton et al., 2013; Hans et al., 2013; Brennecka et al., 2013; Yokoyama et al., 2015; Yobregat et al., 2017; Shollenberger et al., 2018; Myojo et al., 2018; Henshall et al., 2018; Burkhardt et al., 2019; Fukai and Yokoyama, 2019b; Charlier et al., 2019). However, the $^{84}Sr/^{86}Sr$ measurement results of terrestrial rock samples reported in these studies, expressed as $\mu^{84}Sr = 10^6 \times [(^{84}Sr/^{86}Sr)_{sample}/(^{84}Sr/^{86}Sr)_{standard} - 1]$, show significant disagreements. Studies using static measurement methods provided consistent, negative $\mu^{84}Sr$ values from –30 to –20 ppm for terrestrial samples (Moynier et al., 2012; Paton et al., 2013; Yokoyama et al., 2015; Yobregat et al., 2017; Henshall et al., 2018; Fukai and Yokoyama, 2019b), while the multidynamic measurements yielded higher terrestrial $\mu^{84}Sr$ values that are unresolved from zero (Hans et al., 2013; Yobregat et al., 2017; Henshall et al., 2018). The measured $\mu^{84}Sr$ values of the same samples (e.g., BHVO–2 and BCR–2 basalts, Henshall et al., 2018) should not differ between the two measurement methods if they both produce accurate results. Therefore, the apparent discrepancy between the static and multidynamic methods reflects an analytical artefact. The magnitude of this discrepancy (20–30 ppm) is similar to the nucleosynthetic $\mu^{84}Sr$ anomalies found in many carbonaceous meteorites (Andreasen and Sharma, 2007; Moynier et al., 2012; Qin et al., 2011; Paton et al., 2013; Yokoyama et al., 2015; Fukai and Yokoyama, 2019b; Amelin et al., 2019; Burkhardt et al., 2019; Charlier et al., 2017), so it can potentially distort our understanding about the early Solar System isotopic reservoirs. Currently, two critical analytical problems need to be solved in the ^{84}Sr/^{86}Sr systematics in cosmochemistry and geochemistry: (1) what caused the μ^{84}Sr discrepancy between the static and multidynamic measurement methods? (2) what is the accurate μ^{84}Sr value of terrestrial samples?

In this study, we address these unresolved issues by analysing the Sr standard NIST SRM 987 and a series of natural samples using a 3-line multidynamic TIMS Sr isotope measurement method. This method allows us to obtain high-precision ^{84}Sr/^{86}Sr and ^{87}Sr/^{86}Sr ratios in static and multidynamic modes simultaneously, and to evaluate their performance and compare their accuracy and precision. We evaluate the fractionation drift effect in multidynamic Sr isotope analyses, and apply a method to correct the biases caused by this effect. Using the fractionation drift-corrected multidynamic ^{84}Sr/^{86}Sr results of the standard and terrestrial samples, we investigate the cause of the static–multidynamic μ^{84}Sr discrepancy, and attempt to determine the accurate μ^{84}Sr value in terrestrial samples. We also discuss a variety of other effects that potentially influence the measurement accuracy and precision and generate correlations in fractionation-corrected Sr isotopic ratios.

2. Materials and methods

2.1 Standard and samples

A solution of the National Institute of Standards and Technology Standard Reference Material 987 (SRM 987 hereafter) was analysed as the standard in this study. Several natural samples were also analysed for Sr isotopes, including three United States Geological Survey (USGS) reference materials BHVO–2 (Hawaiian basalt), BCR–2 (Columbia River basalt), and BIR–1 (Icelandic basalt), a seawater sample, and a pyroxene fraction from the Angra dos Reis (ADOR) angrite meteorite.

The BHVO–2, BCR–2, and BIR–1 rocks were supplied as fine powders. Approximately 1000 mg of each rock was digested in a Savillex Teflon beaker with 5 mL 12 mol/L HNO_3 + 10 mL 25 mol/L HF mixed acids at 120 °C on hotplate for more than 48 hours. The digested samples were evaporated to dryness, and then repetitively dissolved in 12 mol/L HNO_3 and re-evaporated for three times to reduce the volume of fluorides. The samples were finally dissolved in 50 mL 6 mol/L HCl. One mL of the solutions (corresponding to 20 mg of the original rocks) was processed in each batch of column chemistry.

A 500 mg sample of ADOR analysed here is a part of the sample set prepared for uranium isotope analyses (Huyskens et al., 2020). Examination of this fraction under binocular microscope showed the absence of any minerals other than pyroxene. The solution after U separation on Eichrom UTEVA resin containing all major and most trace elements (including Sr) was dried down and redissolved in 3 mol/L HNO_3 for Sr separation.

The seawater sample (provided by M. Ellwood) was collected from the southern Pacific Ocean, where the sampling location (32°29.54' S, 151°00.21' W, depth = 500 m) is far away from direct continental runoffs. The sample was 0.2 µm-filtered and was acidified with distilled HNO_3. One mL of the seawater sample was evaporated to dryness and redissolved in 1 mL 3 mol/L HNO_3 for Sr separation.

2.2 Chemical separation of Sr

Sr was separated from the matrix elements using a 3-step column chemistry procedure:

(1) Fe removal. Yobregat et al. (2017) showed that the separation of Sr using the Eichrom Sr resin can be interfered by the substantial existence of Fe in the matrix elements. Therefore, Fe was removed from the samples before Sr separation. Samples dissolved in 1 mL 6 mol/L HCl were loaded onto Teflon columns (inner diameter = 3.5 mm, resin bed length = 30 mm) filled with 0.2 mL cleaned Bio-Rad AG1–X8 anion exchange resin (200–400 mesh) on top of 0.1 mL Eichrom Pre-filter resin (100–150 µm size). Bulk fractions con-

taining Sr were directly eluted and collected using 1.5 mL 6 mol/L HCl, while Fe was retained on the column. The collected bulk fractions without Fe were evaporated and redissolved in 1 mL 3 mol/L HNO_3 for Sr separation. This step was used for the basalt solutions, but was not needed for seawater that has much lower concentration of Fe. For ADOR, Fe removal was a part of the U separation procedure (similar to that described by Amelin et al., 2019), and was not repeated here.

(2) Sr separation. Samples containing Sr dissolved in 1 mL 3 mol/L HNO_3 were loaded onto Teflon columns (inner diameter = 3.5 mm, resin bed length = 30 mm) filled with 0.2 mL cleaned Eichrom Sr resin (50–100 μm size) on top of 0.1 mL Eichrom Pre-filter resin (100–150 μm size). The Pre-filter resin was used for absorbing organic materials released from the overlaying Sr resin. Matrix elements were washed off using 2 mL 3 mol/L HNO_3. Subsequently, Sr was eluted and collected using 2 mL 0.02 mol/L HNO_3. The Sr fractions were evaporated and redissolved in 0.5 mL 3 mol/L HNO_3 for purification.

(3) Sr purification. Our chemistry tests show that some of the separated Sr fractions after the step (2) contain too much organic materials. Evaporated samples occasionally have had anomalous red to black muddy appearance, and would easily spread when loaded onto Re filaments. These samples also show poor emission of Sr^+, and yield severe signal instabilities when being measured in TIMS. Accordingly, a purification step was performed after Sr separation to remove the residual organic matter and further reduce the content of matrix elements (e.g., Ba). Sr fractions dissolved in 0.5 mL 3 mol/L HNO_3 were loaded onto small Teflon columns (resin bed volume = 50 μL) filled with 2/3 resin bed volume of Eichrom Sr resin (50–100 μm size) on top of 1/3 resin bed volume of Eichrom Pre-filter resin (100–150 μm size). Remaining matrix elements (if any) were washed off using 1 mL 3 mol/L HNO_3. Finally, Sr was eluted and collected using 0.5 mL 0.02 mol/L HNO_3, and was evaporated at 80 °C on hotplate with addition of 75 μL 0.007 mol/L H_3PO_4. The evaporated samples ap-

peared as clear and transparent tiny liquid drops, suggesting that the content of organic material is reduced.

The total procedure blank of the chemical separation is <3 pg Sr. The overall yield of Sr separation is better than 95% when tested using the BCR–2 basalt.

2.3 Mass spectrometry

Purified and evaporated Sr samples (containing 500–1000 ng Sr) were mixed with 1 μL TaF_5 activator (prepared following Charlier et al., 2006) and were loaded onto the centre of pre-outgassed single Re filaments. The mixture solutions were dried by supplying 0.4 A current through the filaments for 20 min in the air. Our experience shows that this low-temperature, slow drying procedure is important for getting a stable ion signal during the subsequent TIMS measurement. The filament current was then turned up to ca. 2.3 A with a rate of 0.2 A/min until a dull-red glow is seen.

Strontium isotopic analyses were performed at the Australian National University using a Thermo Scientific Triton *Plus* multicollector thermal ionization mass spectrometer. The measurement condition and cup configuration used are listed in Table 1. Before measurement, the filaments were preheated to 2500 mA (ca. 1380 °C) in 50 min with gradually decreasing heating rate from 800 mA/min to 5 mA/min. Amplifier gains were calibrated at the end of the preheating procedure with the analyser gate closed. One measurement typically included two runs which consisted of 50–70 blocks of 10 cycles (i.e., 500–700 cycles) in total. Each cycle consisted of 3 acquisition lines of 8 s integration time + 3 s idle time (Table 1). The first measurement run (ramp-up run) started immediately when the preheating was completed and small Sr signals appeared, and was operated with 5 mA/min filament heating. It was terminated after the block when the ^{88}Sr ion beam reached a steady intensity of 2×10^{-10} A (i.e., 20 V when a 10^{11} Ω amplifier is used). The measurement was then immediately switched to the second run (plateau run), which was operated with the default inter-block heating/cooling function of Triton to maintain the ion beam intensity between 80% and 120% of the initial intensity (i.e., ^{88}Sr ≈ 20 V). The reason for the separation of measurements is that the inter-block heating/cooling function cannot be activated in the middle of a run. This technique (using and combining ramp-up and plateau runs) was discussed in detail by Amelin and Merle (2021). The maximum filament current was set to 3700 mA (ca. 1710 °C filament temperature). The second run was stopped when the sample was completely exhausted. A complete measurement typically takes 7–10 hours. For both measurement runs, the amplifier matrix was rotated after each block, the baseline was measured for 30 s before each block, and the peak centre and lens focus tuning were automatically repeated before each 5 blocks. The isobaric interference of ^{87}Rb on ^{87}Sr was monitored using ^{85}Rb, and was subtracted on-line assuming ^{87}Rb/^{85}Rb = 0.386. The Rb interference was always negligible during the plateau run, and in most cases was negligible during the entire analysis.

Table 1 Measurement condition and cup configuration of the multidynamic TIMS method used in this study.

<table>
<tr><td>Room temperature (°C)</td><td colspan="11">18–22</td></tr>
<tr><td>Room humidity (%)</td><td colspan="11">20–50</td></tr>
<tr><td>Ion source pressure (mbar)</td><td colspan="11">$<8.0 \times 10^{-8}$</td></tr>
<tr><td>Ion getter pressure (mbar)</td><td colspan="11">4×10^{-9}</td></tr>
<tr><td>Filament temperature (°C)</td><td colspan="11">1380–1710</td></tr>
<tr><td>Cup</td><td>L3</td><td>L2</td><td>L1</td><td>Ax</td><td>H1</td><td>H2</td><td>H3</td><td colspan="2">Zoom optics</td><td rowspan="2">Integration time (s)</td><td rowspan="2">Idle time (s)</td></tr>
<tr><td>Amplifier (Ω)[a]</td><td>10^{11}</td><td>10^{11}</td><td>10^{11}</td><td>10^{11}</td><td>10^{11}</td><td>10^{11}</td><td>10^{11}</td><td>Focus (V)</td><td>Dispersion (V)</td></tr>
<tr><td>Line 1</td><td></td><td></td><td>^{84}Sr</td><td>^{85}Rb</td><td>^{86}Sr</td><td>^{87}Sr</td><td>^{88}Sr</td><td>–2</td><td>8</td><td>8.389</td><td>3.000</td></tr>
<tr><td>Line 2</td><td></td><td>^{84}Sr</td><td>^{85}Rb</td><td>^{86}Sr</td><td>^{87}Sr</td><td>^{88}Sr</td><td></td><td>0</td><td>0</td><td>8.389</td><td>3.000</td></tr>
<tr><td>Line 3</td><td>^{84}Sr</td><td>^{85}Rb</td><td>^{86}Sr</td><td>^{87}Sr</td><td>^{88}Sr</td><td></td><td></td><td>2</td><td>–8</td><td>8.389</td><td>3.000</td></tr>
</table>

[a] Amplifier rotation: “left”

3. Data processing

The data of the two measurement runs were combined into a single file. All subsequent data processing procedures were performed on the combined data file using an in-house Microsoft Office Excel template. Complete calculation and statistical treatment procedures, including equations, are detailed in the Appendix A in the Supplementary Materials, and are summarized below.

For each measurement cycle, $^{84}Sr/^{86}Sr$ and $^{87}Sr/^{86}Sr$ ratios were calculated using four different methods: static, multistatic (MS), multidynamic without fractionation interpolation (MD), and multidynamic with fractionation interpolation (MDFI).

The static $^{84}Sr/^{86}Sr$ and $^{87}Sr/^{86}Sr$ ratios of the 3 magnetic settings (lines) were calculated by correcting mass fractionation to $^{88}Sr/^{86}Sr = 8.375209$ using the exponential law (Thirlwall, 1991). The multistatic (MS) isotopic ratios were calculated by taking the arithmetic mean of the static isotopic ratios from the 3 lines.

The simple multidynamic (MD) $^{84}Sr/^{86}Sr$ ratio was also calculated by correcting the instrumental mass fractionation using the exponential law. The $^{84}Sr/^{86}Sr$ ratio measured at line 1 and the $^{88}Sr/^{86}Sr$ ratio measured at line 3 were used in the calculation. Our MD $^{84}Sr/^{86}Sr$ calculation equation is equivalent to the equation (2) of Henshall et al. (2018) and the equation (2) of Yobregat et al. (2017), and 97.7% of cup efficiency is mathematically cancelled during the multidynamic fractionation correction.

Two MD $^{87}Sr/^{86}Sr$ ratios can be calculated in our 3-line method using combined lines 1 + 2 and lines 2 + 3. The first MD ratio, $(^{87}Sr/^{86}Sr)_{MD\text{–}A}$, was calculated by taking the geometric mean of the measured $^{87}Sr/^{86}Sr$ ratios of line 1 and line 2, followed by mass fractionation correction using the measured $^{88}Sr/^{86}Sr$ ratio of line 2. Our calculation equation has a similar form as the multidynamic $^{145}Nd/^{144}Nd$ equation of Garçon et al. (2018), and ca. 99.6% of cup efficiency is mathematically cancelled. Our equation is a factor of 2 more effective in removing cup efficiency components than the multidynamic $^{87}Sr/^{86}Sr$ equations used in previous studies (Thirlwall, 1991; Hans et al., 2013; Yobregat et al., 2017; Wendt and Haase, 1998; Carlson, 2014). The second MD $^{87}Sr/^{86}Sr$ ratio, $(^{87}Sr/^{86}Sr)_{MD–B}$, was calculated similarly using the measured $^{87}Sr/^{86}Sr$ ratios of line 2 and line 3, and the measured $^{88}Sr/^{86}Sr$ ratio of line 3. The final MD $^{87}Sr/^{86}Sr$ ratio $[(^{87}Sr/^{86}Sr)_{MD–C}]$ was calculated by taking the geometric mean of $(^{87}Sr/^{86}Sr)_{MD–A}$ and $(^{87}Sr/^{86}Sr)_{MD–B}$, following Thirlwall (1991).

The MDFI $^{84}Sr/^{86}Sr$ and $^{87}Sr/^{86}Sr$ ratios were calculated in similar ways as the MD ratios, but with a linear interpolation applied to the $^{88}Sr/^{86}Sr$ ratios before fractionation correction. In the MDFI $^{84}Sr/^{86}Sr$ calculation for a cycle, the $^{88}Sr/^{86}Sr$ ratio used for fractionation correction was determined by interpolating the line 3 $^{88}Sr/^{86}Sr$ ratio at the 1/3 point between the current cycle and its previous cycle (i.e., 2 lines back, at the same time when $^{84}Sr/^{86}Sr$ was measured at line 1). The $^{88}Sr/^{86}Sr$ ratios used for MDFI $^{87}Sr/^{86}Sr$ calculations were calculated by interpolating the line 2 and line 3 $^{88}Sr/^{86}Sr$ ratios at the corresponding 5/6 points between the current cycle and its previous cycle (i.e., 0.5 lines back). Our interpolation method assumes that the measured $^{88}Sr/^{86}Sr$ ratios varied linearly along with time during a cycle. No fractionation interpolation and MDFI calculation were made for the first cycle of each block, because it was separated from its previous cycle by inter-block baseline measurement, lens optic and peak centre tunning, automatic filament heating, etc. The mass fractionation may not evolve linearly during this long time interval with changing ion emission, and the attempt of interpolating between blocks can introduce significant uncertainties.

Once all the cycle isotopic ratios were calculated, the block average isotopic ratios and their standard errors were derived. The average isotopic ratios of the analysed sample were then calculated by averaging the block average isotopic ratios weighted by the squared reciprocals of their standard errors. This weighting approach ensures that larger weights are assigned to more precisely measured blocks, and as a consequence, the sample average isotopic ratios are insensitive to the poorly analysed blocks associated with large standard errors, which may result from low ion beam intensities or accidental noises. When multiple repetitive analyses of the same sample are pooled together, the pooled weighted average isotopic ratios and weighted standard errors were calculated using the similar weighting approach. The consistency of the pooled repetitive analyses of the same sample were evaluated using the weighted mean square weighted deviation (WMSWD).

4. Results and discussion

4.1 Results of SRM 987 measurements

The ^{84}Sr/^{86}Sr and ^{87}Sr/^{86}Sr results of 43 repetitive analyses of the standard SRM 987 are summarized in Table 2 and Table 3 respectively. The 2 relative standard deviation (2RSD) values are used to evaluate the intermediate precision over the analytical session. From Tables 2 and 3, the MS, MD, and MDFI methods generally yield precisions 2–5 times better than the static method for both ^{84}Sr/^{86}Sr and ^{87}Sr/^{86}Sr. In addition, the MDFI method yields a better ^{84}Sr/^{86}Sr precision (29 ppm) than the MD method (36 ppm). However, such precision improvement by fractionation interpolation is not observed for ^{87}Sr/^{86}Sr; all the MD and MDFI ^{87}Sr/^{86}Sr ratios have similar precisions of 5–6 ppm. The best precisions for ^{84}Sr/^{86}Sr and ^{87}Sr/^{86}Sr (29 ppm and 5 ppm respectively) are both achieved by the multidynamic method. These precisions are similar to the recent high-precision Sr isotope studies using either static or multidynamic methods (Andreasen and Sharma, 2007; Moynier et al., 2012; Paton et al., 2013; Hans et al., 2013; Yobregat et al., 2017; Henshall et al., 2018; Fukai and Yokoyama, 2019b; Burkhardt et al., 2019; Charlier et al., 2019).

The results of individual SRM 987 measurements are plotted against the time of measurement in Fig. 1 to show the variations of isotopic ratios throughout the 6-month analytical session (April to October 2019). Fig. 1a and 1d show significant temporal drifting of static Sr isotopic ratios in the analytical session. All the temporal drifts or fluctuations are well outside the 2SE uncertainties of individual measurements, as also indicated by the MSWD values much greater than 1 (Tables 2 and 3). In contrast, such temporal drifting is absent in the MD and MDFI results (Fig. 1b, c, e, f). The observed systematic changes of static Sr isotopic ratios that are not accompanied by changes in the MD and MDFI values thus must reflect the changes of Faraday cup efficiencies during the measurements. Using the observed temporal drifting of the static ^{87}Sr/^{86}Sr and ^{84}Sr/^{86}Sr ratios from the 3 lines (Fig. 1a, d), it is possible to retrieve the deterioration degrees of the Faraday cups used in our measurements. A quantitative evaluation of Faraday cup deterioration during our analytical session is conducted by Di et al. (2021).

In addition to the drifts of static isotopic ratios (and sometimes multidynamic isotopic ratios, Garçon et al., 2018; Fukai et al., 2017) and the consequential decrease of long-term reproducibility, Faraday cup deterioration can also lead to increase of individual measurement uncertainty and deterioration of short-term analytical reproducibility. This is best seen in the static measurement results of standards over several years or when cups are replaced (e.g., Carlson, 2014; Miyazaki et al., 2016), and can be explained by the uneven distribution of deposition in the cups and the increasing sensitivity of secondary charged particle yield to the exact point of ion incidence (Sharma et al., 1996; Carlson, 2014). However, whether Faraday cup deterioration also causes precision decline for multidynamic isotopic ratios has not been clearly seen from the data of Garçon et al. (2018) and Fukai et al. (2017). We divided the MDFI ^{87}Sr/^{86}Sr and ^{84}Sr/^{86}Sr data from our analytical session into five sub-sessions (Fig. 1c, f; each sub-session contains ca. nine analyses of the standard which are temporally clustered), and calculated 2RSD precisions within each sub-session. We also do not observe a systematic precision deterioration of the multidynamic isotopic ratios with ongoing instrument usage. The lack of temporal drifting and precision deterioration strongly support that the multidynamic method can effectively minimize the effects of Faraday cup deterioration through time.

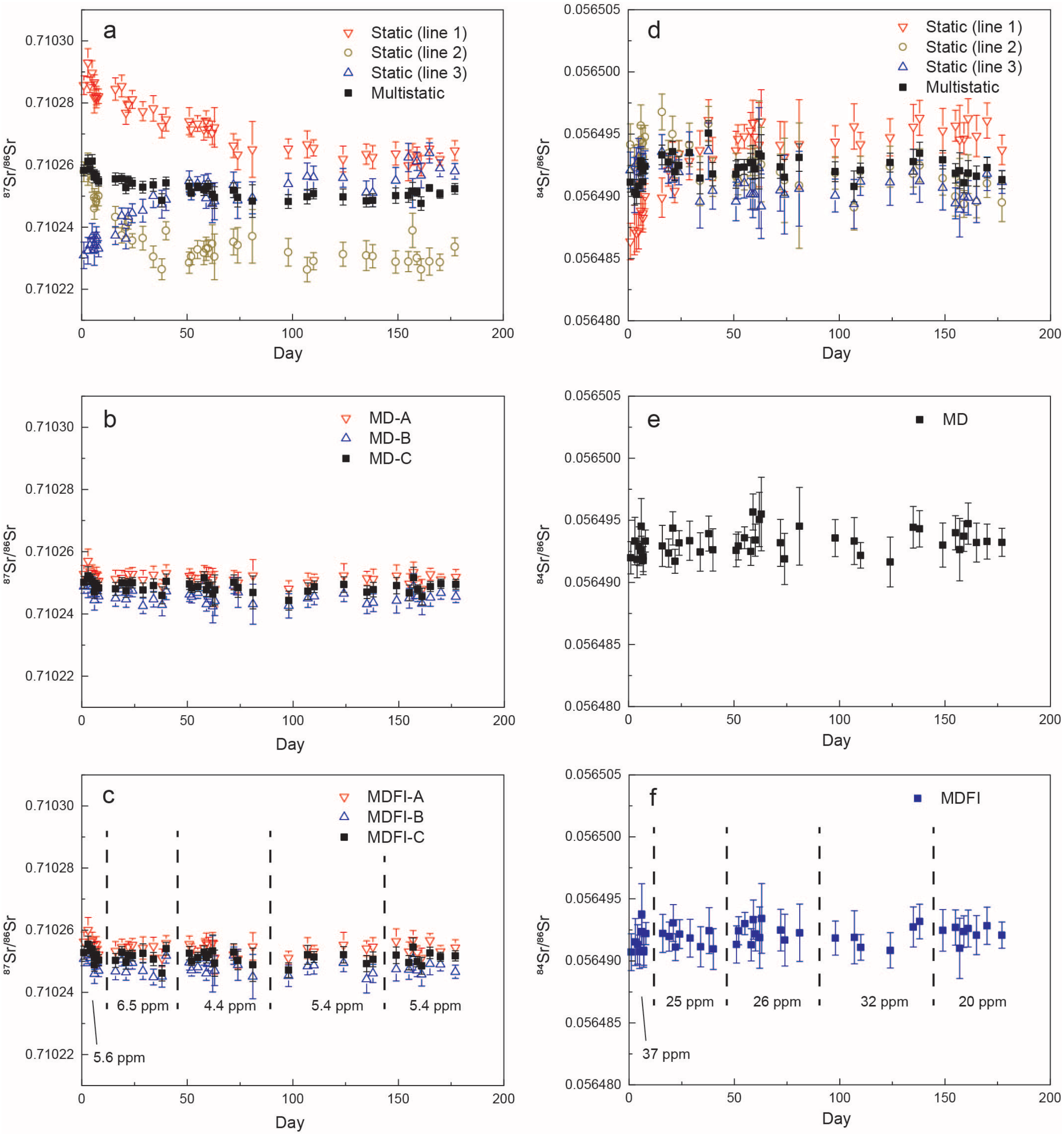

Figure 1. $^{87}Sr/^{86}Sr$ and $^{84}Sr/^{86}Sr$ measurement results of the standard SRM 987 plotted against the time of measurement (day since the beginning of the analytical session). (a)–(c): Static, multistatic (MS), multidynamic without fractionation drift correction (MD), and multidynamic with fractionation drift correction (MDFI) $^{87}Sr/^{86}Sr$ ratios; (b)–(d): static, MS, MD, and MDFI $^{84}Sr/^{86}Sr$ ratios. In (b) and (c), "A" represents the multidynamic $^{87}Sr/^{86}Sr$ ratio cal-

culated using the raw $^{87}Sr/^{86}Sr$ and $^{88}Sr/^{86}Sr$ ratios from lines 1 + 2; “B” represents the multi-dynamic $^{87}Sr/^{86}Sr$ ratio calculated using the raw $^{87}Sr/^{86}Sr$ and $^{88}Sr/^{86}Sr$ ratios from lines 2 + 3; “C” represents the geometric mean of “A” and “B”. Note that the panels of the same Sr isotopic ratios ($^{87}Sr/^{86}Sr$ or $^{84}Sr/^{86}Sr$) are presented in the same scale for direct comparison. In (c) and (f), the analytical session is divided into five sub-sessions, and 2RSD precisions of MDFI–C $^{87}Sr/^{86}Sr$ and MDFI $^{84}Sr/^{86}Sr$ are calculated within each sub-session.

Table 2 Summary of ^{84}Sr/^{86}Sr measurement results of SRM 987.

	Static (line 1)	Static (line 2)	Static (line 3)	Multistatic	MD[b]	MDFI[b]
N	43	43	43	43	43	43
Average	**0.0564931**	**0.0564924**	**0.0564912**	**0.0564922**	**0.0564932**	**0.0564920**
2SD[a]	0.0000058	0.0000035	0.0000026	0.0000019	0.0000021	0.0000016
2RSD (ppm)	103	63	46	34	36	29
Weighted average	**0.0564928**	**0.0564925**	**0.0564913**	**0.0564922**	**0.0564931**	**0.0564920**
2WSE	0.0000009	0.0000005	0.0000004	0.0000003	0.0000003	0.0000002
2RWSE (ppm)	16	9.5	6.5	4.7	5.0	4.2
WMSWD	19	7.6	3.0	4.1	2.0	1.5

[a] SD = standard deviation, RSD = relative standard deviation, WSE = weighted standard error, RWSE = relative weighted standard error, WMSWD = weighted mean square weighted deviation; abbreviations are the same in Table 3. Data are not weighted in the calculation of the average, 2SD, and 2RSD; data are weighted by the squared reciprocals of their standard errors in the calculation of the weighted average, 2WSE, 2RWSE, and WMSWD.

[b] MD = multidynamic without fractionation drift correction; MDFI = multidynamic with fractionation drift correction; abbreviations are the same in Table 3.

Table 3 Summary of $^{87}Sr/^{86}Sr$ measurement results of SRM 987.

	Static (line 1)	Static (line 2)	Static (line 3)	Multistatic	MD–A[b]	MD–B[b]	MD–C[b]	MDFI–A[b]	MDFI–B[b]	MDFI–C[b]
N	43	43	43	43	43	43	43	43	43	43
Average	**0.7102730**	**0.7102369**	**0.7102479**	**0.7102528**	**0.7102515**	**0.7102459**	**0.7102487**	**0.7102543**	**0.7102483**	**0.7102513**
2SD[a]	0.0000184	0.0000185	0.0000183	0.0000068	0.0000035	0.0000042	0.0000034	0.0000039	0.0000043	0.0000038
2RSD (ppm)	26	26	26	10	4.9	5.9	4.8	5.5	6.1	5.4
Weighted average	**0.7102735**	**0.7102376**	**0.7102475**	**0.7102534**	**0.7102516**	**0.7102463**	**0.7102490**	**0.7102543**	**0.7102486**	**0.7102514**
2WSE	0.0000028	0.0000028	0.0000029	0.0000009	0.0000005	0.0000006	0.0000004	0.0000005	0.0000006	0.0000005
2WRSE (ppm)	3.9	4.0	4.1	1.3	0.7	0.8	0.6	0.8	0.9	0.7
WMSWD	40	41	42	13	1.8	2.4	1.8	2.0	2.5	2.3

[a] The same as in Table 2.

[b] MD and MDFI are the same as in Table 2; A = multidynamic $^{87}Sr/^{86}Sr$ ratio calculated from lines 1 + 2; B = multidynamic $^{87}Sr/^{86}Sr$ ratio calculated from lines 2 + 3; C = the geometric mean of A and B.

4.2 Fractionation drift effect

Though the multidynamic measurement procedure can effectively minimize the uncertainties induced by Faraday cup deterioration, a natural drawback of the multidynamic method is its non-real time instrumental fractionation correction, or “fractionation drift” effect. In multidynamic measurements, the isotopic ratio used to monitor mass fractionation (e.g., ^{88}Sr/^{86}Sr) is measured at a different line from the isotopic ratio of interest (e.g., ^{87}Sr/^{86}Sr or ^{84}Sr/^{86}Sr). The lines dedicated to the measurements of the two isotopic ratios are temporally separated by a gap consisting of integration times and idle times. If the sample’s fractionation degree significantly changes during this time gap, the fractionation-corrected multidynamic isotopic ratio will be biased. The direction of this bias depends on the order of the acquisition of the two ratios as well as the direction of fractionation (normal vs. inverse), while its magnitude is proportional to the sample’s instantaneous fractionation rate and the length of the time gap. This can be demonstrated by taking derivative for the calculation equation of the MD ^{84}Sr/^{86}Sr ratio (i.e., equation 3*a* in the Supplementary Materials):

$$\frac{\mathrm{d}(^{84}\mathrm{Sr}/^{86}\mathrm{Sr})_{\mathrm{MD}}}{(^{84}\mathrm{Sr}/^{86}\mathrm{Sr})_{\mathrm{MD}}} = -\beta_{84} \cdot \frac{\mathrm{d}(^{88}\mathrm{Sr}/^{86}\mathrm{Sr})_{\mathrm{line\ 3}}}{(^{88}\mathrm{Sr}/^{86}\mathrm{Sr})_{\mathrm{line\ 3}}} = -\beta_{84} \cdot r \cdot \mathrm{d}t \quad (1)$$

where d*t* is the time gap between line 1 and line 3, *r* is the instantaneous drift rate of ^{88}Sr/^{86}Sr, and $\beta_{84} = -1.02325$. The relation between the relative bias in multidynamic ^{87}Sr/^{86}Sr and time gap and fractionation rate can be written similarly. The fractionation drift effect will primarily make the multidynamic isotopic ratios less accurate, and, if fractionation rate is largely variable among the repetitive measurements, also undermine the measurement precision.

This effect was first recognized and evaluated by Roth et al. (2014) in the multidynamic measurements of ^{142}Nd/^{144}Nd. They showed that the fractionation drift between lines, monitored using ^{146}Nd/^{144}Nd, can be fast enough (e.g., >0.21 ppm/s) to cause a shift in the fractionation-corrected ^{142}Nd/^{144}Nd ratio greater than the desired long-term precision (2RSD = 5 ppm). Significant precision improvement was observed after the fractionation drift effect was corrected cycle-by-cycle using locally determined instantaneous fractionation rates, and the pre-existing correlation between μ^{142}Nd and fractionation rate also disappeared (Garçon et al., 2018; Roth et al., 2014). These results suggest that correcting the fractionation drift is necessary in multidynamic ^{142}Nd/^{144}Nd measurements with precision better than 5 ppm. The fractionation drift effect in multidynamic Sr isotope analyses was previously noticed (Yobregat et al., 2017; Henshall et al., 2018), but was not corrected or evaluated in detail. Here we apply a linear interpolation method to correct the fractionation drift effect in multi-dynamic Sr isotope analyses, and derive the MDFI isotopic ratios (see section 3). Our interpolation approach is similar to that of Horan et al. (2018), and is effectively a simplified version of the methods of Roth et al. (2014) and Garçon et al. (2018). We only interpolate the measured ^{88}Sr/^{86}Sr ratio between two consecutive cycles in the same block, so that the temporal variation of ^{88}Sr/^{86}Sr in this short time interval has a better linearity (see Appendix B in the Supplementary Materials for details). Also, since only two cycles from the same block are involved in the interpolation, a complex fitting of the ^{88}Sr/^{86}Sr–time relation is avoided, and the abrupt change of ^{88}Sr/^{86}Sr caused by inter-block heating and lens focusing need not be considered (cf. Garçon et al., 2018).

The relations between the ^{84}Sr/^{86}Sr and ^{87}Sr/^{86}Sr measurement results of SRM 987 (expressed as μ^{84}Sr and μ^{87}Sr values) and the average fractionation rate of individual measurements, before and after fractionation drift correction, are shown in Fig. 2a–d. Before fractionation drift correction (Fig. 2a, c), we observed broad $\mu^{84,87}$Sr vs. fractionation rate trends that have slopes consistent with the theoretically predicted slopes from equation (1), though the observed slopes are also not clearly resolved from zero. This may be due to the limited variation range of fractionation rate in the SRM 987 measurements. After fractionation drift correction (Fig. 2b, d), the regressed $\mu^{84,87}$Sr vs. fractionation rate slopes equal to zero, the expected value, and the linear correlation coefficients (r) are also reduced. The fractionation drift correction improved the precision and MSWD value for multidynamic $^{84}Sr/^{86}Sr$ (Table 2), but such improvements are not observed for $^{87}Sr/^{86}Sr$, suggesting that fractionation drift does not significantly affect the multidynamic measurement precision of $^{87}Sr/^{86}Sr$. This can be explained by the combination of the following factors: (1) the measurements of the raw $^{87}Sr/^{86}Sr$ and $^{88}Sr/^{86}Sr$ ratios in our multidynamic method are only separated by 0.5 lines (cf. 2 lines for $^{84}Sr/^{86}Sr$, 4 times longer), and (2) the exponential fractionation law exponent (β) of $^{87}Sr/^{86}Sr$ is only ca. 0.5 (cf. $\beta \approx -1$ for $^{84}Sr/^{86}Sr$, the absolute value is twice larger). Therefore, the fractionation drift effect on $^{87}Sr/^{86}Sr$ should be a factor of 8 weaker than that on $^{84}Sr/^{86}Sr$.

The effect of fractionation drifting on $^{84}Sr/^{86}Sr$ is more prominent in the measurements of terrestrial samples (Fig. 2e, f). Without fractionation drift correction, the MD $\mu^{84}Sr$ of terrestrial samples is positively correlated with fractionation rate (Fig. 2e). The regressed slope of 19.0 ± 12.7 s is clearly resolved from zero and is consistent with the predicted slope (23.3 s) from equation (1). The theoretical slope of 23.3 s suggests that each +1 ppm/s difference in fractionation rate could cause a +23.3 ppm bias in $\mu^{84}Sr$, and the samples with higher fractionation rates have more positively biased $\mu^{84}Sr$ values. The high fractionation rates of terrestrial samples up to 3.6 ppm/s can thus lead to significant overestimations of $\mu^{84}Sr$ up to ca. 84 ppm, much higher than the desired measurement precision of ca. 30 ppm. In Fig 2f, after fractionation drift correction, the $\mu^{84}Sr$ vs. fractionation rate correlation disappeared, suggesting that this bias has been eliminated.

Many previous multidynamic Sr isotope measurement methods adopted separated measurement runs for $^{84}Sr/^{86}Sr$ and $^{87}Sr/^{86}Sr$ to minimize the fractionation drift effect on $^{84}Sr/^{86}Sr$ (e.g., Yobregat et al., 2017; Hans et al., 2013). With the fractionation interpolation method applied here, such separation is no longer necessary. Precise $^{84}Sr/^{86}Sr$ and $^{87}Sr/^{86}Sr$ ratios can be measured simultaneously using the 3-line multidynamic method reported here, and the measurement time and sample consumption can be reduced. We note that if one would like to further reduce the fractionation drifting bias on $^{84}Sr/^{86}Sr$, the line 2 and line 3 in our multidynamic method can be swapped, so that the time gap between the measurements of the raw $^{84}Sr/^{86}Sr$ and $^{88}Sr/^{86}Sr$ ratios can be shortened by a half.

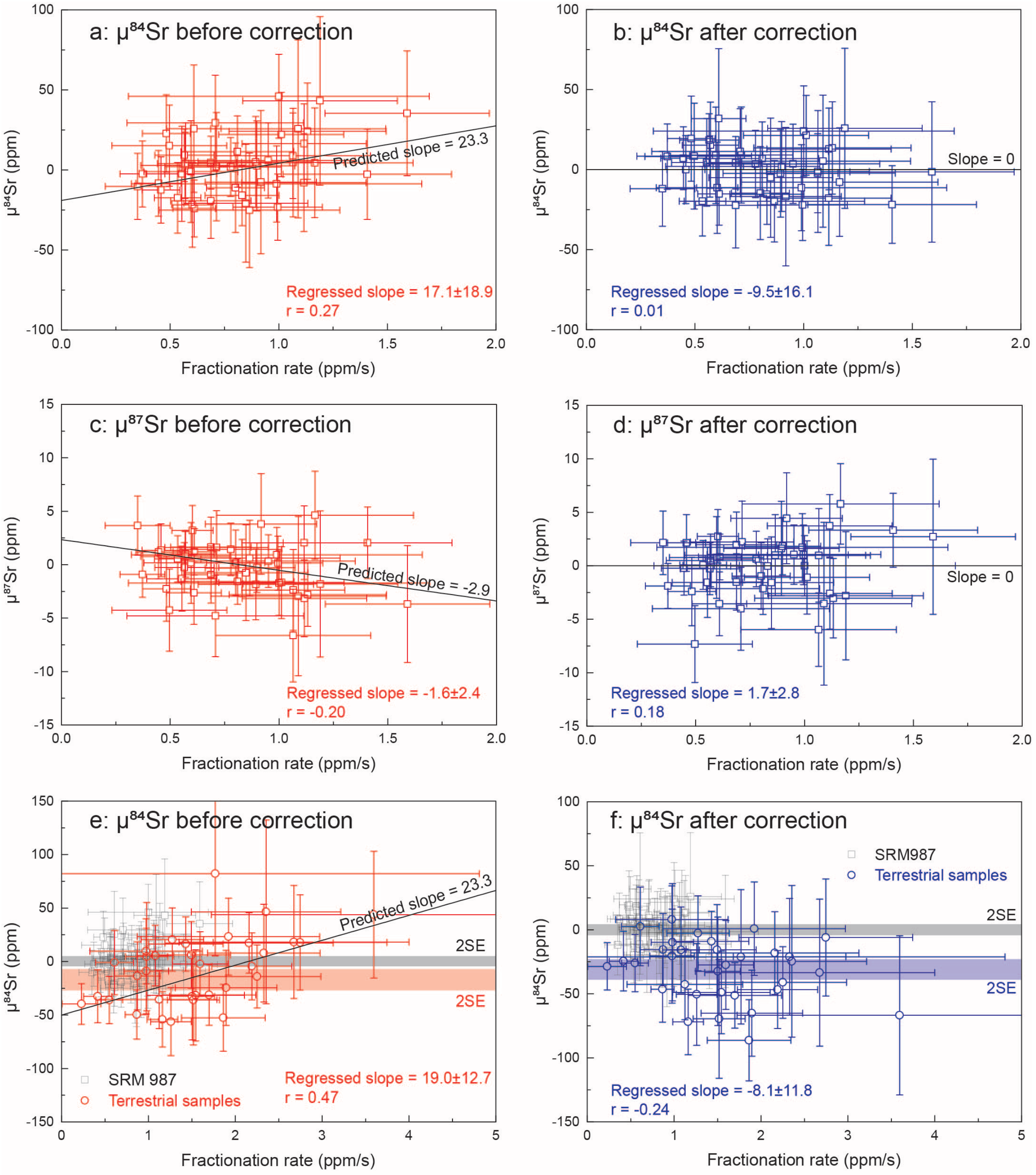

Figure 2. Multidynamic $\mu^{84}Sr$ and $\mu^{87}Sr$ values vs. average fractionation rate of individual measurements for: (a)–(d) SRM 987, and (e)–(f) terrestrial samples. In each panel, μ-values are calculated relative to the corresponding weighted average SRM 987 isotopic ratios (re-

ported in Tables 2 and 3). Uncertainties of the μ-values and fractionation rates are 2SE. The linearly fitted slopes (with 2SE uncertainties) and correlation coefficients (r) of the data points are shown in each panel. Panels on the left side (a, c, e) show data before fractionation drift correction (i.e., MD or MD–C values); theoretical trend lines with slopes predicted using equation (1) are also plotted for comparison. Panels on the right side (b, d, f) show data after fractionation drift correction (i.e., MDFI or MDFI–C values); the correlations should have an expected slope of 0. In (e) and (f), the SRM 987 data same as in (a) and (b) are plotted as grey squares for reference; the grey horizontal bars are the 2SE confidence intervals of the weighted average SRM 987 μ^{84}Sr values; the red and blue horizontal bars are the 2SE confidence intervals of the weighted average μ^{84}Sr values of the terrestrial samples.

4.3 Terrestrial μ^{84}Sr value and the static–multidynamic discrepancy

Our μ^{84}Sr measurement results of the terrestrial samples have reproduced the static–multidynamic discrepancy documented in previous studies (Yobregat et al., 2017; Henshall et al., 2018; Hans, 2013). The μ^{84}Sr results of 33 analyses of terrestrial samples, calculated using the MS, MD, and MDFI methods, are summarized in Table 4 and illustrated in Fig. 3. The results of different terrestrial samples (BHVO–2, BCR–2, BIR–1, and seawater) are pooled and averaged together because no systematic difference in μ^{84}Sr is detected between those samples. The MS method yields a weighted average terrestrial μ^{84}Sr value of –31 ± 7 ppm, which is in good agreement with the previous static or multistatic analytical results (e.g., Moynier et al., 2012; Paton et al., 2013; Yokoyama et al., 2015; Fukai and Yokoyama, 2019b). In contrast, the MD method yields a weighted average terrestrial μ^{84}Sr value of –17 ± 10 ppm, which is 14 ± 12 ppm higher than the MS result. Previously reported multidynamic terrestrial μ^{84}Sr values (Hans et al., 2013; Yobregat et al., 2017; Henshall et al., 2018) are even higher and are closer to zero (i.e., the value of the standard SRM 987), but Fukai and

Yokoyama (2019b) recently reported a multidynamic terrestrial μ^{84}Sr value (–16 ± 15 ppm) in good agreement with ours. The inconsistency between the average μ^{84}Sr value of terrestrial samples measured using the static and multidynamic methods reflects analytical artefacts existing in one (or both) of the measurement methods. Several theories have been proposed to explain the cause of this discrepancy, such as the optical aberration and ion truncation associated with non-ideal peak shapes in static measurements (Yobregat et al., 2017), but none of them can self-consistently explain all the observations (Henshall et al., 2018; Hans, 2013). Coupled with this issue, the true μ^{84}Sr value of terrestrial samples relative to the standard SRM 987 is also under debate.

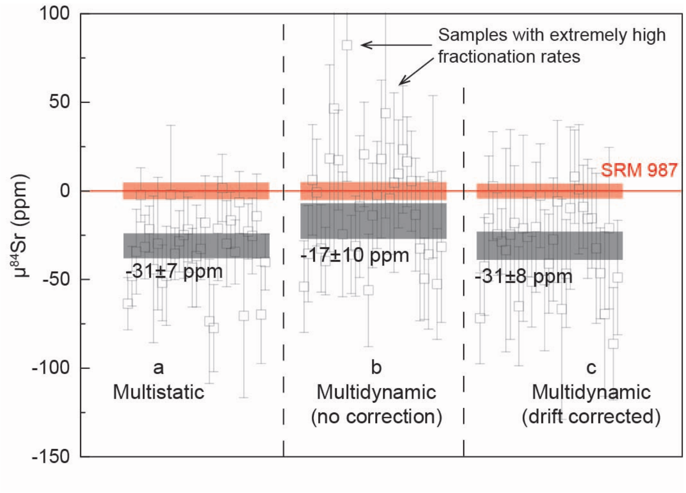

Figure 3. μ^{84}Sr results of the terrestrial samples, measured and calculated using: (a) the multistatic (MS) method, (b) the multidynamic method without fractionation drift correction (MD), and (c) the multidynamic method with fractionation drift correction (MDFI). The μ^{84}Sr values in each panel are calculated relative to the corresponding weighted average SRM 987 ^{84}Sr/^{86}Sr ratios, and uncertainties are 2SE. Red horizontal bars are the 2SE confidence intervals of the weighted average SRM 987 μ^{84}Sr values; grey horizontal bars and the numbers near them show the 2SE confidence intervals of the weighted average μ^{84}Sr values of the terrestrial samples.

Table 4 μ^{84}Sr measurement results of BIR–1, BCR–2, BHVO–2, seawater, and ADOR.

	μ^{84}Sr (MS)[a]	μ^{84}Sr (MD)[a]	μ^{84}Sr (MDFI)[a]
BIR–1 ($N = 6$)			
Weighted average (ppm)	–33 ± 19	–31 ± 17	–32 ± 19
MSWD	3.7	2.3	3.0
BCR–2 ($N = 8$)			
Weighted average (ppm)	–35 ± 9	–14 ± 22	–35 ± 13
MSWD	0.8	3.5	1.4
BHVO–2 ($N = 13$)			
Weighted average (ppm)	–27 ± 11	1 ± 13	–18 ± 11
MSWD	2.7	2.0	1.7
Seawater ($N = 6$)			
Weighted average (ppm)	–33 ± 15	–39 ± 16	–53 ± 18
MSWD	1.6	1.1	1.6
All terrestrial samples (N = 33)			
Weighted average (ppm)	*–31 ± 7*	*–17 ± 10*	*–31 ± 8*
MSWD	*3.6*	*3.6*	*2.5*
ADOR ($N = 5$)			
Weighted average (ppm)	–3 ± 20	4 ± 24	3 ± 22
MSWD	3.0	6.3	4.4

[a] MS, MD, and MDFI are the same in Table 2; uncertainties are 2 SE.

Based on the observed positive correlation between MD μ^{84}Sr and fractionation rate in the terrestrial samples (Fig. 2e), we suggest that the static–multidynamic discrepancy of terrestrial μ^{84}Sr observed in our data was generated by the fractionation drift effect in multidynamic measurements. Fig. 2e demonstrates that fractionation drift can cause overestimations of μ^{84}Sr depending on the samples' fractionation rates during measurements. The standard SRM 987 can also be biased by this effect with the same dependence on fractionation rate (i.e., slope = 23.3 s). Hence, the biases in samples can be partly compensated during the calculation of μ^{84}Sr values, and can be completely cancelled if the samples have an average fractionation rate equal to that of SRM 987. The ^{88}Sr/^{86}Sr fractionation rates in the SRM 987 measurements have an average value of 0.82 ± 0.56 ppm/s (2SD). However, the analysed terrestrial samples exhibit higher and more variable fractionation rates with a range from 0.23 to 3.60 ppm/s (Fig. 2e), so they can be more strongly biased than SRM 987. As a result, the average μ^{84}Sr value of the terrestrial samples measured using the MD method is elevated due to the existence of samples with fractionation rates substantially higher than the SRM 987 average rate. In contrast, fractionation drift has no effect on static or multistatic measurements, as all raw isotopic ratios are measured simultaneously and the isotopic fractionation is corrected real-time. Thus, the MS μ^{84}Sr results for the terrestrial samples may be more accurate than the MD results. In fact, if only the terrestrial samples with fractionation rates close to the SRM 987 average rate (e.g., fractionation rate < 1.5 ppm/s) are selected and averaged, a lower weighted average MD μ^{84}Sr value of –25 ± 13 ppm is obtained, agreeing with the MS result. From Figs. 2f and 3c, after correcting the fractionation drift effect in multidynamic measurements, the MDFI method yields a weighted average terrestrial μ^{84}Sr value of –31 ± 8 ppm, which is in perfect agreement with our MS measurement result. This apparently resolves the observed inconsistency between our MS and MD μ^{84}Sr results.

The possibility of fractionation drift causing the static–multidynamic μ^{84}Sr discrepancy was proposed in previous studies (Yobregat et al., 2017; Henshall et al., 2018). However, Yobregat et al. (2017) argued that the ^{88}Sr/^{86}Sr fractionation rates in their measurements never exceeded 0.1 ppm/s, so that the biases in their multidynamic results are unlikely to cause the static–multidynamic discrepancy. Their reported fractionation rates, however, are more than one order of magnitude lower than the fractionation rates observed in our measurements, though similar chemical procedures, mass spectrometry techniques, and sample sizes were used by us and by Yobregat et al. (2017). The reason for this difference is unclear. From our practice, the entire variation ranges of ^{88}Sr/^{86}Sr during TIMS measurements, observed from the beginning of evaporation of Sr to complete sample exhaustion, are typically 8.28–8.46 (ca. 2×10^4 ppm). A fractionation rate of 0.1 ppm/s thus corresponds to ca. 2×10^5 s (>2 days) for the sample to evaporate completely. Using the typical ^{88}Sr ion current of $12–20\times10^{-11}$ A of Yobregat et al. (2017), the theoretical ion yield of the measurements of Yobregat et al. (2017) would be 2.9–4.8% for 1 μg Sr load, approximately one order of magnitude higher than ours. Henshall et al. (2018) also obtained the conclusion that fractionation drift is not responsible for the static–multidynamic discrepancy based on the absence of correlation between fractionation rate and multidynamic ^{84}Sr/^{86}Sr ratio, as well as the elevated μ^{84}Sr value of a reversely fractionated sample inconsistent with the expectation from the fractionation drift effect. These observations suggest that factors other than fractionation drift might be responsible for the discrepancies seen in their data.

Our observation that chemically processed terrestrial samples on average have higher fractionation rates compared to the unprocessed standard when measured in TIMS is similar to the behaviour of Nd samples reported by Garçon et al. (2018) and Andreasen and Sharma

(2009). This may be attributed to the presence of organic residues or matrix elements after column chemistry (see Appendix C in the Supplementary Materials for details). Therefore, using unprocessed SRM 987 standard to evaluate the quality of multidynamic Sr isotope analyses may lead to an inaccurate estimation of measurement precision, unless the fractionation drift effect is accurately corrected.

4.4 Amplifier decay time

Similar to previous multidynamic Sr isotope analytical methods (Thirlwall, 1991; Hans et al., 2013), our 3-line method returns two independent multidynamic ^{87}Sr/^{86}Sr ratios, MD–A and MD–B, using the combinations of lines 1 + 2 and lines 2 + 3. Theoretically, no systematic difference between MD–A and MD–B is expected when all measurement conditions are ideal. However, from Fig. 1b, the two MD ^{87}Sr/^{86}Sr ratios of SRM 987 exhibit a stable, small but resolvable offset of 0.0000052 ± 0.0000007 (or 7 ± 1 ppm) throughout the entire analytical session. This offset persists after fractionation drift correction (Fig. 1c) and is not correlated with fractionation rate. Similar ca. 7 ppm offsets are also seen in the MD and MDFI ^{87}Sr/^{86}Sr ratios of the terrestrial samples (Fig. 4).

In older-generation mass spectrometers, the inequality of two multidynamic ^{87}Sr/^{86}Sr ratios becomes obvious after prolonged instrument usage, probably due to the ion truncations associated with imperfect peak alignment between magnetic settings (Thirlwall, 1991). During our measurements, all peaks were perfectly aligned using zoom optics, and no hint of anomalous peak and/or baseline shape was observed, leaving this explanation unlikely. However, the use of different zoom optic settings between multidynamic lines can possibly change the mass spectrometer transmission and induce an additional instrumental fractionation, as demonstrated by Trinquier et al. (2008) and Amelin and Huyskens (2013). This effect cannot be fully evaluated at this point, because the magnitude and mass dependence of such fractionation have not been tested yet. The observed offset is also unlikely to be generated by different Faraday cup efficiencies like in the static ^{87}Sr/^{86}Sr results (Fig. 1a), because most (ca. 99.6%) of the cup efficiency components propagated into the multidynamic ratios have been mathematically cancelled. If cup efficiency differences were responsible for the observed 7 ppm offset between the two multidynamic ^{87}Sr/^{86}Sr ratios, then a ca. 1950 ppm difference between the Faraday cup efficiencies C_{H2}/C_{Ax} and C_{H1}/C_{L1} would be required. In all our SRM 987 measurements, the relative difference between these two quantities (estimated using $[\frac{(^{87}\mathrm{Sr}/^{86}\mathrm{Sr})_{\mathrm{line\ 2}} \cdot (^{87}\mathrm{Sr}/^{86}\mathrm{Sr})_{\mathrm{line\ 3}}}{(^{87}\mathrm{Sr}/^{86}\mathrm{Sr})_{\mathrm{MDFI-A}} \cdot (^{87}\mathrm{Sr}/^{86}\mathrm{Sr})_{\mathrm{MDFI-B}}}]^2 - 1)$ never exceeded 70 ppm, which can only account for <0.25 ppm difference between the two multidynamic ^{87}Sr/^{86}Sr ratios.

Similar systematic offsets between multidynamic Sr isotopic ratios were observed in recent studies and were attributed to insufficient amplifier signal decay (Hans, 2013; Yobregat et al., 2017; Fukai and Yokoyama, 2019b). During multidynamic measurements, if the residual signals in amplifiers after an acquisition line do not recover to their normal baseline levels within the idle time (set to discharge the resistor–capacitor circuit), the new signals in the next line cannot be measured accurately. For example, assuming that an amplifier has been used for ^{88}Sr measurement in an earlier line, and that the signal in the amplifier descends to 3 ppm of its previous intensity in 3 s idle time, the succeeding ^{86}Sr measurement will be erroneously elevated by ca. 25 ppm. It has also been shown that inappropriate Decay DAC settings of amplifiers can generate negative dipping of signals shortly after cutting off the ion beams (Yobregat et al., 2017; Trinquier et al., 2013). These positive or negative residual signals left in amplifiers can ultimately lead to systematic errors in isotopic ratios.

During our measurements, we never observed a periodic fluctuation of isotopic ratios along with the rotation of the amplifier matrix (cf. Yobregat et al., 2017), suggesting that the Decay DAC settings (as well as other parameters) for all amplifiers were accurate. This also ensures that no significant additional noise was introduced by amplifier rotation. However, the idle time setting used in our measurements (3 s) is shorter than those in other recent Sr isotope studies (from 4 s to 10 s, Henshall et al., 2018; Fukai and Yokoyama, 2019b; Yobregat et al., 2017), though it is similar to those used in Nd isotope analyses (e.g., Garçon et al., 2018). Unlike Nd, which has smaller differences between the abundances of isotopes [e.g., the maximal ratio of signals from two consecutive lines in the method of Garçon et al. (2018) is ^{144}Nd/^{145}Nd ≈ 2.9], the isotopes of Sr that are consecutively measured using the same amplifier in our method have much larger abundance contrasts (e.g., ^{88}Sr/^{86}Sr ≈ 8.3, ^{86}Sr/^{84}Sr ≈ 17.6), making them more susceptible to the memory effect of amplifiers. During our measurements, the ^{84}Sr and ^{86}Sr of line 1, ^{87}Sr and ^{88}Sr of line 2, and ^{87}Sr and ^{88}Sr of line 3 are all possibly affected by the insufficient amplifier signal decay, and their synthetic effects may have generated the slight difference between the MD–A and MD–B ^{87}Sr/^{86}Sr ratios. The multidynamic ^{84}Sr/^{86}Sr ratios are also possibly affected at the same time, as demonstrated by Fukai and Yokoyama (2019b). Therefore, the ^{87}Sr/^{86}Sr and ^{84}Sr/^{86}Sr ratios reported in Tables 2 and 3 should not be taken as the accurate absolute isotopic compositions of SRM 987. More accurate absolute isotopic ratios need to be determined with an optimized selection of Decay DAC parameter (e.g., Trinquier et al., 2013) using actual ion beams, and a longer idle time, in order to minimize the effect of residual signals in amplifiers. Using a longer idle time, however, may enhance the effect of fractionation drift, and reduce the ion usage efficiency.

Though the absolute Sr isotopic ratios can be biased by the residual signals in amplifiers, this effect should systematically apply to all measurements of standards and unknown samples as long as similar ion beam intensities are used. Therefore, the biases caused by this effect, together with other systematic errors introduced during multidynamic measurements (such as the change of the mass spectrometer transmission as the function of the zoom setting), can be cancelled by calculating the μ^{84}Sr values or by normalizing the ^{87}Sr/^{86}Sr ratios using the standard SRM 987: $(^{87}\mathrm{Sr}/^{86}\mathrm{Sr})_{\mathrm{sample,N}} = (^{87}\mathrm{Sr}/^{86}\mathrm{Sr})_{\mathrm{sample}}/(^{87}\mathrm{Sr}/^{86}\mathrm{Sr})_{\mathrm{SRM\ 987}} \cdot 0.7102500$. Here “N” denotes “normalized”, and 0.7102500 is an accepted ^{87}Sr/^{86}Sr ratio of SRM 987

(Hans et al., 2013). After such normalization, no systematic difference is present between the MDFI $^{87}Sr/^{86}Sr$ ratios A and B of the terrestrial samples (Fig. 4), confirming that the biases have been eliminated. This again affirms that in high-precision (e.g., ppm-level) isotopic studies, relative isotope compositions (e.g., δ-, Δ-, ε-, and μ-values, and normalized isotopic ratios) have better accuracies and should always be reported along with absolute isotopic ratios.

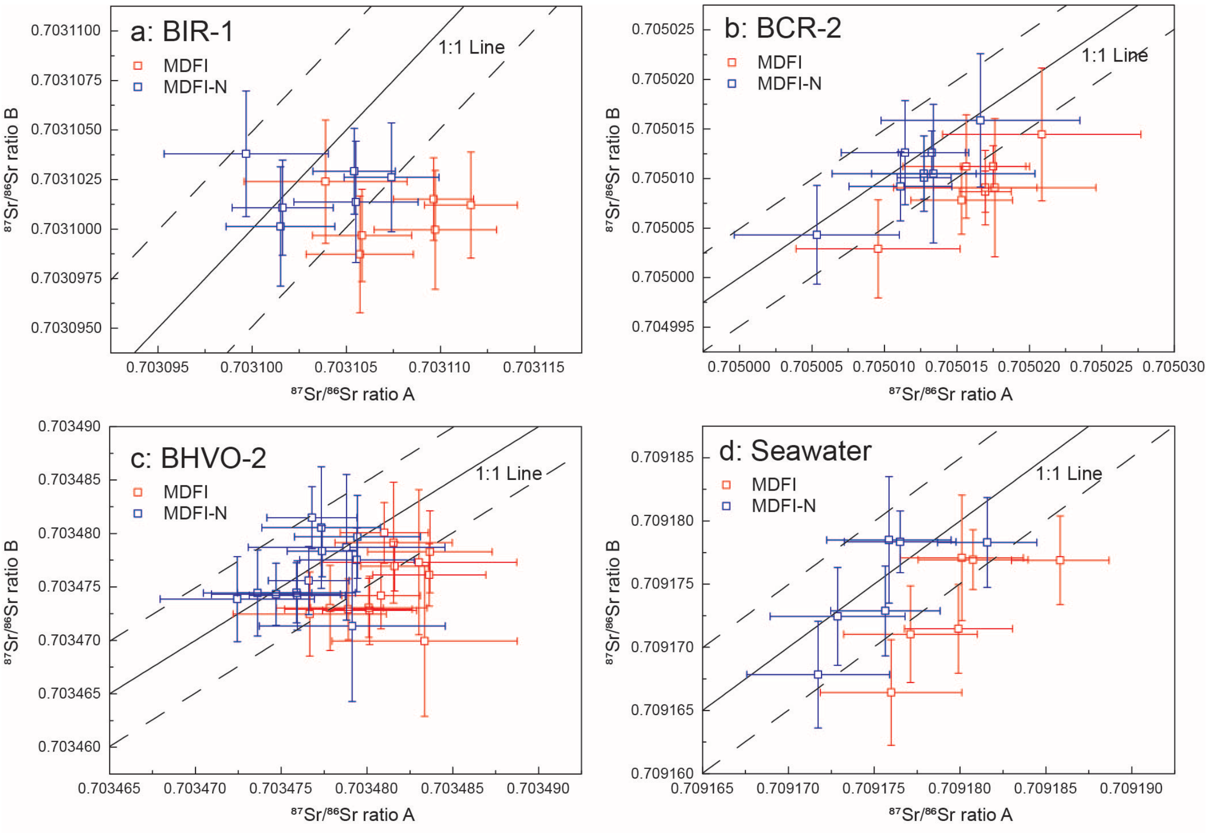

Figure 4. Plots of MDFI $^{87}Sr/^{86}Sr$ ratio B vs. ratio A for the analysed terrestrial samples: (a) BIR–1, (b) BCR–2, (c) BHVO–2, and (d) seawater. "A" represents the MDFI $^{87}Sr/^{86}Sr$ ratio calculated using the raw $^{87}Sr/^{86}Sr$ and $^{88}Sr/^{86}Sr$ ratios from lines 1 + 2; "B" represents the MDFI $^{87}Sr/^{86}Sr$ ratio calculated using the raw $^{87}Sr/^{86}Sr$ and $^{88}Sr/^{86}Sr$ ratios from lines 2 + 3. "N" denotes $^{87}Sr/^{86}Sr$ ratios normalized to SRM 987 $^{87}Sr/^{86}Sr$ = 0.7102500 (Hans et al., 2013). The black solid and dashed lines show 1:1 lines with ± 7 ppm ranges.

4.5 Correlation between μ^{87}Sr and μ^{84}Sr

A pronounced negative correlation between MDFI μ^{87}Sr and μ^{84}Sr is observed in our SRM 987 measurement results (Fig. 5). The linear fitting of the measured μ^{87}Sr vs. μ^{84}Sr data yields an intercept of 0.02 ± 0.62 and a slope of –0.084 ± 0.043 (uncertainties are 2SE). The 95% envelope ellipse of the data points also illustrates the significant correlation (ellipse major slope = –0.104). Similar correlations between fractionation-corrected isotopic ratios have been recognized as a significant factor limiting the accuracy and precision of Nd isotopic analyses (e.g., Thirlwall, 1991; Caro et al., 2003, 2006; Upadhyay et al., 2008; Andreasen and Sharma, 2009). Below, we explore several possible explanations for the observed μ^{87}Sr–μ^{84}Sr correlation trend.

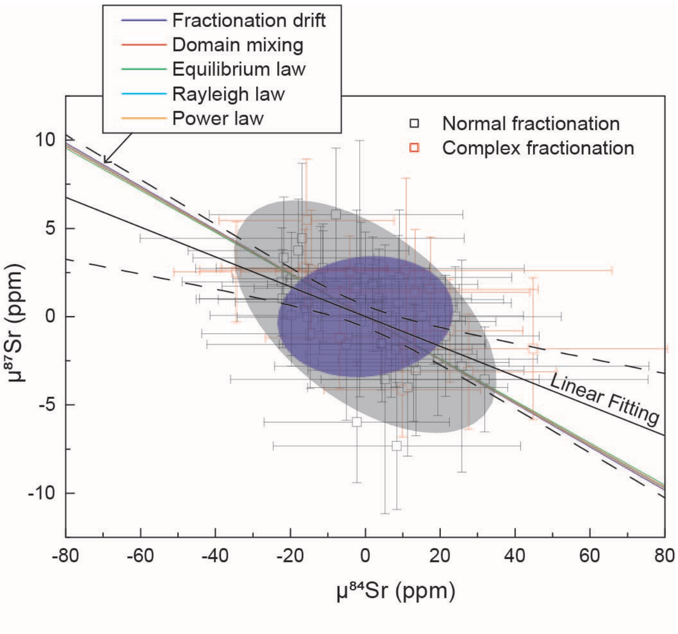

Figure 5. Plot of the MDFI μ^{87}Sr vs. μ^{84}Sr values of the SRM 987 measurements. The μ-values are calculated relative to the weighted average MDFI SRM 987 isotopic ratios, and uncertainties are 2SE. Black and red squares represent the SRM 987 measurements with "normal" and "complex" fractionation trajectories respectively (see section 4.5.5 for their definitions). The grey ellipse is the 95% envelope ellipse of the data points representing the "normal fractionation" measurements. The blue ellipse is the theoretical 95% envelope ellipse

of 1000 SRM 987 measurements simulated using an ion counting statistics model (see Appendix D in the Supplementary Materials). The theoretical μ^{87}Sr vs. μ^{84}Sr correlation trends that can be generated by fractionation drifting, domain mixing, and non-exponential mass fractionations following the equilibrium, Rayleigh, and power laws are shown (in coloured lines) for comparison with the fitted line of the "normal fractionation" data points (in black line). Black dashed curves represent the 2SE confidence interval of the black fitted line.

4.5.1 Ion counting statistics

One most evident explanation for the observed correlation trend is that it reflects the correlated random errors originated from ion counting statistics. During measurements of ion beam intensities using Faraday cups–amplifiers, random errors are produced by two major sources: (1) Poisson noise, which comes from the discrete nature of charges, and (2) Johnson–Nyquist noise, which is the thermal noise coming from the random motion of electrons inside the resistor. Random errors propagated into fractionation-corrected isotopic ratios can be effectively correlated if the calculation equations of these isotopic ratios involve common denominator isotope and/or fractionation monitoring isotope, as demonstrated by Andreasen and Sharma (2009). The magnitudes of these noises also establish the theoretical precision limits of isotopic ratios determined using Faraday cups–amplifiers at given ion beam intensities, integration times, and amplifier resistor values (Wielandt and Bizzarro, 2011; Garçon et al., 2018). The calculation equations of our MDFI ^{84}Sr/^{86}Sr and MDFI–C ^{87}Sr/^{86}Sr ratios (see Appendix A in the Supplementary Materials) both involve the ^{86}Sr intensity measured in line 1 and the ^{88}Sr intensity measured in line 3. Therefore, the fluctuations of the random errors in these two ion beam intensities may have generated the observed correlation. To test this hypothesis, we modelled the error correlation between MDFI μ^{87}Sr and μ^{84}Sr that can be caused by ion counting random errors (see Appendix D in the Supplementary Materials). The results of 1000 simulated SRM 987 measurement runs (blue ellipse in Fig. 5, also shown in Fig. S3 in the Supplementary Materials) represent the theoretical precisions and error correlation of MDFI μ^{87}Sr and μ^{84}Sr under our measurement conditions. The simulated μ^{87}Sr and μ^{84}Sr values exhibit a slightly positive correlation that is inconsistent with the observed correlation trend in terms of both direction and magnitude (see the comparison of the two ellipses in Fig. 5). The opposite correlation directions of the simulated and observed data strongly suggest that random errors originated from ion counting statistics are not the major cause of the observed correlation trend. The larger standard deviations in both μ^{87}Sr and μ^{84}Sr of the observed data imply that another source of error was introduced during our measurements, and was superimposed on the ion counting statistics errors.

4.5.2 Faraday cup efficiency

Correlations between isotopic ratios can be generated by variations of Faraday cup efficiencies if the calculation equations of the isotopic ratios involve common cup efficiency terms, as demonstrated by Garçon et al. (2018) and Yokoyama et al. (2015). In our MDFI isotopic ratio calculation equations (see Appendix A in the Supplementary Materials), most of the Faraday cup efficiency components has been cancelled out; the MDFI ^{84}Sr/^{86}Sr ratio is proportional to a residual term $(\frac{C_{L1}}{C_{H1}})^{-0.02325}$, while the MDFI–C ^{87}Sr/^{86}Sr ratio is proportional to $(\frac{C_{H2}C_{H1}}{C_{Ax}C_{L1}})^{-0.001795}$. Common cup efficiency terms C_{L1} and C_{H1} are present in both equations, and their variations may affect μ^{87}Sr and μ^{84}Sr simultaneously and generate the observed correlation. To test this hypothesis, we simulated the correlation between MDFI μ^{87}Sr and μ^{84}Sr that can be caused by Faraday cup deterioration using the estimated cup efficiency changes during the analytical session (Di et al., 2021). The modelling results show that the variations of Faraday cup efficiencies can cause correlated MDFI μ^{87}Sr and μ^{84}Sr with a slope of –0.159 ± 0.008. This slope is significantly different from the observed correlation slope (–0.084 ± 0.043) by 0.075 ± 0.044. In addition, since the biases in isotopic ratios caused by Faraday cup efficiency have been substantially reduced in the multidynamic calculations, the Faraday cup deterioration degrees observed during our measurements can only account for up to 3.3 ppm variations in μ^{84}Sr, and up to 0.5 ppm variations in μ^{87}Sr, which are much smaller than the ion counting errors. Therefore, the residual Faraday cup efficiencies cannot generate the observed correlation.

4.5.3 Fractionation drift effect

According to equation (1), the relative bias in a multidynamic isotopic ratio caused by fractionation drift is proportional to the fractionation exponent (β), the time gap (d*t*), and the fractionation rate (*r*). The multidynamic ^{87}Sr/^{86}Sr and ^{84}Sr/^{86}Sr are simultaneously affected by the same fractionation rate in a measurement. Therefore, the variations of fractionation rate among measurements can generate correlated μ^{87}Sr and μ^{84}Sr values. The time gap in the multidynamic ^{87}Sr/^{86}Sr measurement is shorter by a factor of 4 than that in ^{84}Sr/^{86}Sr, and the fractionation exponent β of ^{87}Sr/^{86}Sr is approximately –1/2 of that of ^{84}Sr/^{86}Sr. Therefore, the multidynamic μ^{87}Sr and μ^{84}Sr will have a theoretical correlation slope of –0.123 due to fractionation drift. This slope is equal to the observed μ^{87}Sr vs. μ^{84}Sr correlation slope within error. The MDFI μ^{87}Sr and μ^{84}Sr values shown in Fig. 5 have been corrected for fractionation drift, but the corrections are only approximations based on the assumptions that (1) the changes in ^{88}Sr/^{86}Sr during measurements are solely caused by fractionation, and (2) they are linear along with time. Any uncorrected or overcorrected fractionation drift effect caused by noise or violation of the linear assumption may leave residual correlations between MDFI μ^{87}Sr and μ^{84}Sr with a slope of –0.123. However, the fractionation rates of SRM 987 observed in our data only cover a range of 1.24 ppm/s, which theoretically can cause variations of up to 29 ppm in μ^{84}Sr and up to 3.6 ppm in μ^{87}Sr. These variation ranges only correspond to less than a half of the observed μ^{84}Sr and μ^{87}Sr variation ranges (54 ppm and 13 ppm respectively). In addition, the fractionation drift-uncorrected MD μ^{87}Sr and μ^{84}Sr values of

SRM 987 show a correlation slope and variation ranges indistinguishable from those of the drift-corrected MDFI μ^{87}Sr and μ^{84}Sr values when they are plotted together. These observations suggest that the residual fractionation drift effect cannot fully account for the observed MDFI μ^{87}Sr vs. μ^{84}Sr correlation, and another mechanism is still required.

4.5.4 Isotopic fractionation laws

Inaccurate correction of isotopic fractionation in nature and in mass spectrometers can generate correlations between fractionation-corrected isotopic ratios and spurious isotope anomalies (e.g., O'Neil et al., 2008). Here we consider the case where the true isotopic fractionation of Sr occurring in TIMS deviates from the exponential law that has been used for fractionation correction in our measurements. Taking ^{84}Sr/^{86}Sr as an example, assuming that the true ^{84}Sr/^{86}Sr–^{88}Sr/^{86}Sr fractionation behaviour in TIMS follows a law with a similar form as the exponential law (i.e., the generalized power law, GPL, Maréchal et al., 1999), but with a different exponent $\beta_{84,\ \mathrm{law}}$, the exponential law-corrected ^{84}Sr/^{86}Sr ratio obtained in our measurements can then be expressed as:

$$({}^{84}\mathrm{Sr}/{}^{86}\mathrm{Sr})_{\mathrm{exponential}} = ({}^{84}\mathrm{Sr}/{}^{86}\mathrm{Sr})_0 \cdot \left[\frac{({}^{88}\mathrm{Sr}/{}^{86}\mathrm{Sr})_0}{({}^{88}\mathrm{Sr}/{}^{86}\mathrm{Sr})_{\mathrm{m}}}\right]^{\beta_{84,\mathrm{exponential}}-\beta_{84,\mathrm{law}}} \quad (2)$$

where "0" represents the unfractionated initial isotopic ratios and "m" represents the measured raw isotopic ratios. When $\beta_{84,\ \mathrm{law}} = \beta_{84,\ \mathrm{exponential}}$, i.e., when the true isotopic fractionation in TIMS follows the exponential law, the fractionation correction equation (2) accurately returns the unfractionated (^{84}Sr/^{86}Sr)$_0$ ratio. The partial derivative of equation (2) gives:

$$\frac{\partial({}^{84}\mathrm{Sr}/{}^{86}\mathrm{Sr})_{\mathrm{exponential}}}{({}^{84}\mathrm{Sr}/{}^{86}\mathrm{Sr})_{\mathrm{exponential}}} = -\left(\beta_{84,\mathrm{exponential}} - \beta_{84,\mathrm{law}}\right) \cdot \frac{\partial({}^{88}\mathrm{Sr}/{}^{86}\mathrm{Sr})_{\mathrm{m}}}{({}^{88}\mathrm{Sr}/{}^{86}\mathrm{Sr})_{\mathrm{m}}} \quad (3)$$

Equation (3) suggests that the relative bias in an exponential-law corrected isotopic ratio is proportional to the difference between β_{law} and $\beta_{\mathrm{exponential}}$ as well as the degree of fractionation when the true isotopic fractionation behaviour deviates from the exponential law. Since ^{87}Sr/^{86}Sr and ^{84}Sr/^{86}Sr in a measurement are simultaneously biased by the same fractionation degree, the exponential law-corrected μ^{87}Sr and μ^{84}Sr values should be correlated with a slope of $\frac{(\beta_{87,\mathrm{exponential}}-\beta_{87,\mathrm{law}})}{(\beta_{84,\mathrm{exponential}}-\beta_{84,\mathrm{law}})}$ due to the variations of fractionation degree among measurements. Table 5 compares the fractionation exponents β_{84} and β_{87} of several mass fractionation laws that are commonly used in mass spectrometry literature (Maréchal et al., 1999; Davis et al., 2015; Young et al., 2002). From Table 5, Sr isotopic fractionations in TIMS following the equilibrium law, Rayleigh law, and power law are all able to make the exponential law-corrected μ^{87}Sr and μ^{84}Sr correlated with slopes equal to our observed value (–0.084 ± 0.043) within error. Actually, in the β_{84}–β_{87} space (Fig. 6), the curve representing the generalized power law (Maréchal et al., 1999) calculated using actual atomic masses with variable parameter n is approximately linear, and has an average slope of ca. –0.12 at the range $-2 \leq n \leq 2$. Therefore, theoretically any fractionation law differing from the exponential law but following the form of GPL can generate a correlation between the exponential law-corrected μ^{87}Sr and μ^{84}Sr with a slope ≈ -0.12.

However, here we suggest that the TIMS isotopic fractionation of Sr following a law deviating from the exponential law is unlikely to be the cause of our observed μ^{87}Sr vs. μ^{84}Sr correlation for two reasons. First, the equation (3) predicts that the bias caused by incorrect fractionation correction is proportional to fractionation degree (Thirlwall, 1991; Davis et al., 2015; Wasserburg et al., 2012; Andreasen and Sharma, 2009). However, no correlation was observed between the exponential law-corrected ^{84}Sr/^{86}Sr or ^{87}Sr/^{86}Sr ratio and the measured ^{88}Sr/^{86}Sr ratio in our measurements (cf. Thirlwall, 1991; O'Neil et al., 2008; Caro et al., 2006; Fukai et al., 2017). The absence of correlation is valid both among different SRM 987 measurements and within individual SRM 987 measurements (i.e., among blocks). Second, we regressed experimental fractionation exponents for ^{87}Sr/^{86}Sr–^{88}Sr/^{86}Sr and ^{84}Sr/^{86}Sr–^{88}Sr/^{86}Sr ($\beta_{84,\ \mathrm{experiment}}$ and $\beta_{87,\ \mathrm{experiment}}$) using our SRM 987 measurements following the method of Maréchal et al. (1999) and Albarède et al. (2004) to directly test whether the Sr isotope fractionation in TIMS can be adequately described by the exponential law. The $\beta_{84,\,\mathrm{experiment}}$ and $\beta_{87,\,\mathrm{experiment}}$ values regressed using our 43 SRM 987 measurements are plotted in Fig. 6, and their weighted averages are reported in Table 5. In the β_{84}–β_{87} space, the 95% confidence ellipse of the weighted average $\beta_{84,\,\mathrm{experiment}}$ and $\beta_{87,\,\mathrm{experiment}}$ values contains the point representing the exponential law (i.e., $\beta_{84} = -1.02325$, $\beta_{87} = 0.50359$), suggesting that the experimental Sr fractionation behaviour in TIMS is consistent with the exponential law at 0.95 confidence level. A multivariate hypothesis test using the Hotelling's T^2 statistic (see Appendix F in the Supplementary Materials for details) also suggests that the observed weighted average $\beta_{84,\,\mathrm{experiment}}$ and $\beta_{87,\,\mathrm{experiment}}$ values (Table 5) are identical to the exponential law β values at 0.95 confidence level. In contrast, the experimental Sr isotopic fractionation exponents have significant differences from the β values of the equilibrium, Rayleigh, and power laws. Therefore, we confirm that the Sr isotope fractionation occurring in TIMS under our measurement conditions can be accurately described using the exponential law, consistent with the previous conclusion (Thirlwall, 1991).

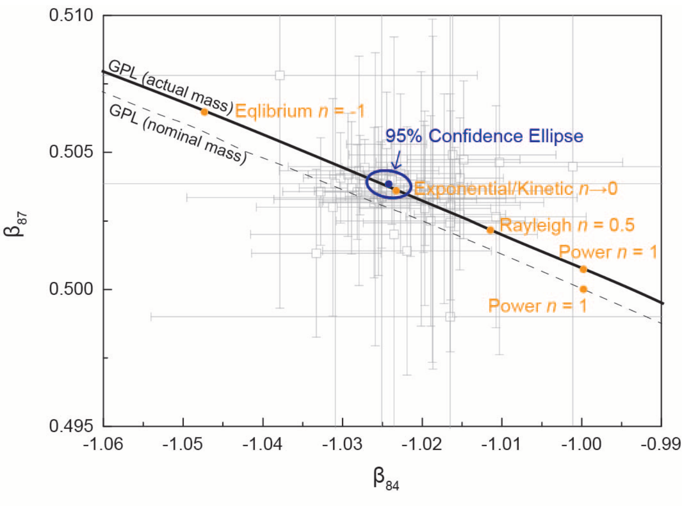

Figure 6. Experimental fractionation exponents of ^{84}Sr/^{86}Sr–^{88}Sr/^{86}Sr (β_{84}) and ^{87}Sr/^{86}Sr–^{88}Sr/^{86}Sr (β_{87}) regressed using our SRM 987 measurements. For each SRM 987 measurement, the experimental β_{84} and β_{87} values are determined by calculating the slopes of the fitted lines of ln(^{84}Sr/^{86}Sr) vs. ln(^{88}Sr/^{86}Sr) and ln (^{87}Sr/^{86}Sr) vs. ln(^{88}Sr/^{86}Sr) respectively using the

measured block average static line 1 isotopic ratios, following the fitting method of York et al. (2004). The squared reciprocals of the 2SE uncertainties of the block average isotopic ratios were used as weights in the fittings. Uncertainties of the plotted β_{84} and β_{87} values are 2SE. The blue dot represents the weighted average β_{84} and β_{87} values from all the SRM 987 measurements (Table 5), and the blue ellipse is its 95% confidence ellipse. The black solid curve represents the generalized power law (GPL, Maréchal et al., 1999) calculated using the actual atomic masses of ^{84}Sr, ^{86}Sr, ^{87}Sr, and ^{88}Sr with variable parameter n, and the orange dots on it represent the special cases of several commonly used isotope fractionation laws. The black dashed curve represents the generalized power law calculated using nominal atomic masses (i.e., integer mass numbers).

Table 5 Fractionation exponents of Sr of several commonly used mass fractionation law.

Fractionation law[a]	n[b]	$\beta_{84,\ \mathrm{law}}$	$\beta_{84,\ \mathrm{exponential}} - \beta_{84,\ \mathrm{law}}$	$\beta_{87,\ \mathrm{law}}$	$\beta_{87,\ \mathrm{exponential}} - \beta_{87,\ \mathrm{law}}$	μ^{87}Sr vs. μ^{84}Sr slope
Equilibrium	–1	–1.04731	0.02406	0.50646	–0.00287	–0.119
Exponential (or kinetic)	0[c]	–1.02325	0.00000	0.50359	0.00000	
Rayleigh	0.5	–1.01143	–0.01182	0.50216	0.00144	–0.121
Power	1	–0.99974	–0.02350	0.50072	0.00287	–0.122
Power (nominal mass)	1	–1.00000	–0.02325	0.50000	0.00359	–0.155
Experiment weighted average[d]		–1.0242 ± 0.0017	0.0009 ± 0.0017	0.50384 ± 0.00023	–0.00025 ± 0.00023	–0.26 ± 0.51

[a] Fractionation exponents are calculated using the actual atomic mass from IUPAC (Holden et al., 2018), except the power law (using nominal mass) and the experiment weighted average (derived from observations).

[b] The parameter n in the generalized power law (Maréchal et al., 1999).

[c] The exponential law, or kinetic law, corresponds to $n \rightarrow 0$.

[d] Uncertainties are 2SE.

4.5.5 Secondary mass fractionation effects

The remaining possibility that may have caused the correlation between the MDFI μ^{87}Sr and μ^{84}Sr is the secondary mass fractionation effects superimposed on the exponential law fractionation (O'Neil et al., 2008). Three types of secondary mass fractionation effects have been proposed in previous studies to explain the correlation between fractionation-corrected isotopic ratios: (1) selective ion truncation loss associated with imperfect peak alignments and/or peak shapes (Thirlwall, 1991; Albarède et al., 2004; Yobregat et al., 2017); (2) mass separation and ion loss induced by the electron deflection magnet in the Triton ion source (Caro et al., 2006); and (3) the isotope mixing of ions derived from variably fractionated sample reservoirs on the filament (Hart and Zindler, 1989; Upadhyay et al., 2008; Andreasen and Sharma, 2009). The former two effects have long been noticed and have led to extensive empirical corrections of secondary fractionation (Thirlwall, 1991; Vance and Thirlwall, 2002; Caro et al., 2003, 2006; Albarède et al., 2004). However, here we consider these two effects minor during our measurements, and rather unlikely to be the reason for the observed μ^{87}Sr vs. μ^{84}Sr correlation, because: (1) all peaks were perfectly aligned using zoom optics during measurements, and no anomalous peak and/or baseline shape was observed; and (2) no source magnet is present in our mass spectrometer. A recently-proposed additional component of secondary instrumental fractionation is linked to the accumulation of conductive materials (e.g., H_3PO_4 from activators) on the ion lens assemblage surface (Fukai and Yokoyama, 2019a); however, this effect was not observed during our study.

In contrast, the aforementioned effect (3) cannot be easily ruled out. During TIMS measurements, the samples loaded onto the filament may form several lateral or vertical domains with different fractionation rates and degrees, due to the temperature heterogeneity across the filament or the heat and sample vapour transfer from the surface of the metal to the surface of the sample load. Ions derived from domains at different fractionation stages may mix together after leaving the filament, and co-contribute to the measured ion beams. Even if the isotope fractionation during evaporation and ionization of each domain follows the same exponential law curve, the linear isotope mixing of ions from different domains will make the measured isotopic compositions deviating from the original curve (see Fig. 1 of Upadhyay et al., 2008). Fractionation correction using the exponential law (or any other fractionation laws) will generate biases in isotopic ratios. The directions of the biases are dependent on the fractionation exponent β; the bias is positive when $\beta > 1$ or $\beta < 0$, and is negative when $0 < \beta < 1$. For Sr, the biases caused by domain mixing are always positive for ^{84}Sr/^{86}Sr and negative for ^{87}Sr/^{86}Sr. The magnitudes of the biases are not easy to quantify, because they are decided by the number of domains present in the evolving sample, their individual isotopic compositions, as well as their mixing ratios, which are all difficult to characterize and control (Upadhyay et al., 2008). Nonetheless, the biases caused by domain mixing in different isotopic ratios of the element are correlated because they are derived from the same mixing process. A simple linear mixing modelling following the methods of Upadhyay et al. (2008) and Andreasen and Sharma (2009) suggests that the biases in μ^{87}Sr and μ^{84}Sr induced by domain mixing should have a theoretical correlation slope of ca. –0.12. This slope is consistent with our observed correlation slope within error. Therefore, domain mixing is a plausible mechanism to generate the observed correlation between the MDFI μ^{87}Sr and μ^{84}Sr.

The domain mixing effect in actual measurements is difficult to recognize and quantitatively correct. Upadhyay et al. (2008) found that Nd samples start to display deviations from the exponential law fractionation curve from some specific points of the measurements. Fractionation-corrected isotope ratios measured thereafter exhibit increased scatter and systematic shifts that are consistent with the predictions from isotope mixing models. These abnormal periods are accompanied by stalled or reversed fractionation degree–time trajectory, which is a definitive indicator of isotopic mixing at the ion source. In addition, Andreasen and Sharma (2009) showed that the data collected during the normal fractionation periods of measurement runs before or after reverse fractionation can also be considerably affected by domain mixing, and suggested that significant mixing effect may exist in all measurements, no matter what the fractionation trajectory looks like. Therefore, it is difficult to assess whether a measurement showing normal fractionation has been affected by domain mixing solely from its fractionation trajectory, unless other non-radiogenic isotopes are monitored at the same time (Andreasen and Sharma, 2009), which is possible for the elements with a larger number of isotopes such as Nd, but not for Sr. It is, however, interesting to notice the similarity of the in-run shifts of fractionation-corrected isotopic ratios caused by domain mixing and by the decoupled mass fractionation of even- and odd-mass isotopes. The latter effect has been detected in Pb isotope TIMS measurements (Doucelance and Manhes, 2001; Thirlwall, 2000; Amelin et al., 2005), and is characterized by the systematic shifts of fractionation-corrected isotopic ratios that involve both even- and odd-mass isotopes (i.e., ^{207}Pb/^{206}Pb and ^{205}Pb/^{206}Pb) as the sample approaches exhaustion.

The majority of our SRM 987 measurements exhibited either normal fractionation throughout the run, or normal fractionation followed by reverse fractionation that appears at a late stage of the run, similar to the cases described by Upadhyay et al. (2008). For these measurements (which we label as “normal fractionation”) we excluded the data blocks after the appearances of reverse fractionation during the data processing procedure. Inclusion of these blocks will obviously lead to erroneous isotopic fractionation correction, as well as inaccurate fractionation interpolation and fractionation rate estimation. There are also a number of SRM 987 measurements (ca. 20% of the total number) that exhibited reverse fractionation in the early or middle stages of the run, and the fractionation direction switched from normal to reverse several times. These measurements were labelled as “complex fractionation” and were discarded in the previous calculations and discussions, because their isotopic ratios were likely biased by the domain mixing effect. Actually, we found that the MDFI μ^{87}Sr and μ^{84}Sr values of the “normal fractionation” and “complex fractionation” measurements are indistinguishable when plotted together (Fig. 5). This implies that our “normal fractionation” measurements also could have been affected by the domain mixing effect, and that this effect may universally exist in our Sr isotope analyses, similar to the conclusion of Andreasen and Sharma (2009) based on Nd. The isotope mixing effect with variable degrees in different SRM 987 measurements may have generated the observed correlation between μ^{87}Sr and μ^{84}Sr, and may account for the 1.5–2 times larger standard deviations of the measured data compared to the theoretical random errors derived from ion counting and amplifier noise.

Overall, our analyses suggest that the observed negative correlation between the MDFI μ^{87}Sr and μ^{84}Sr values of SRM 987 may be a combined effect caused by ion counting statistics, residual fractionation drift effect, and isotope mixing occurring on the filament.

4.6 Inter-laboratory comparison of ^{87}Sr/^{86}Sr

As discussed in the previous sections, systematic errors can be introduced into measured isotopic ratios during TIMS analyses. These systematic errors arise from the subtle but numerous imperfections of features specific to laboratory, instrument, and the measurement and data processing protocols, including, but not limited to the position and geometry of the magnet, the tuning of the electrostatic and magnetic optic system, detector efficiencies, and the stabilities of electronic devices. They are unavoidable in many situations. Therefore, when comparing high-precision isotopic data generated at different laboratories, it is important to ensure that inter-laboratory biases are accounted for. A common way to eliminate systematic errors is to normalize the measured sample isotopic ratios using a simultaneously analysed standard (see also section 4.4 and Appendix E in the Supplementary Materials). If a common standard material is analysed by two laboratories, and the results of unknown samples from both laboratories are normalized to the same "accepted" value of the standard, the two sets of normalized sample data are directly comparable.

The analytical method reported in this paper is mainly designed for high-precision ^{87}Sr/^{86}Sr chronology and μ^{84}Sr anomaly study of meteorite samples, such as Ca–Al-rich inclusions and achondrites. In the previous early Solar System ^{87}Sr/^{86}Sr chronology studies carried out by a number of other laboratories, at least four different materials have been used as standards: NIST (NBS) SRM 987, seawater, plagioclase from the eucrite Moore County, and pyroxene from the angrite Angra dos Reis (ADOR). Standards and normalization methods differ between the more recent (e.g., SRM 987 by Hans et al., 2013) and earlier (seawater and plagioclase from Moore County eucrite by Gray et al., 1973; Podosek et al., 1991) Sr isotopic studies of the early Solar System materials. This has invoked difficulties and arguments over the selection of appropriate standards for normalization and the accurate inter-laboratory comparison of the analytical results of samples (Hans et al., 2013; Papanastassiou, 2015; Papanastassiou and Chen, 2016). A reliable comparison of our meteorite sample analytical results with the previous data, therefore, should be established on the basis of a careful cross-calibration of these standards. Moreover, using several standard materials covering a large ^{87}Sr/^{86}Sr range provides us with an opportunity to test whether the normalization method aforementioned is reliable, and whether the normalization of samples using different standards yield consistent results.

In this study, we analysed Sr isotopes in three out of the four standards: SRM 987, seawater, and ADOR pyroxene. The ^{87}Sr/^{86}Sr results of these standard materials measured by us and by several other laboratories are compared in Table 6 and Fig. 7. Our ^{87}Sr/^{86}Sr measurement results of SRM 987 and ADOR pyroxene are in excellent agreement with those reported by Hans et al. (2013) (Fig. 7b). This is probably because both studies applied multi-dynamic methods, by which the systematic biases caused by Faraday cup efficiencies and amplifier gains are eliminated. The SRM 987, seawater, and Moore County plagioclase analytical results of Podosek et al. (1991) and the CIT 1970s group (Wasserburg et al., 1977; Papanastassiou and Wasserburg, 1973; Gray et al., 1973) are consistent within error (Fig. 7a, c), but they are distinct from our results and the results of Hans et al. (2013), indicating large inter-laboratory biases between those data. Nonetheless, all the standard analytical results reported by us, Hans et al. (2013), Podosek et al. (1991), and the CIT 1970s group are consistently plotted along the same proportional normalization lines (Fig. 7). This indicates that the analytical biases of isotopic ratios in all these laboratories are proportional as expected, and confirms that the measurement results of unknown samples from these laboratories can be reliably compared after normalization to common standard values. In contrast, the standard analytical results reported by the CIT group recently (Papanastassiou and Chen, 2016) using a multidynamic method deviate from the proportional normalization lines defined by our and other laboratories in all the plots (and vice versa; Fig. 7). This suggests that the normalization and inter-laboratory comparison of their analytical results for unknown samples using different standards will result in inconsistent conclusions. The reason for this is not clear, but it undoubtedly suggests that a different normalization method need to be adopted when comparing their sample analytical results with other laboratories.

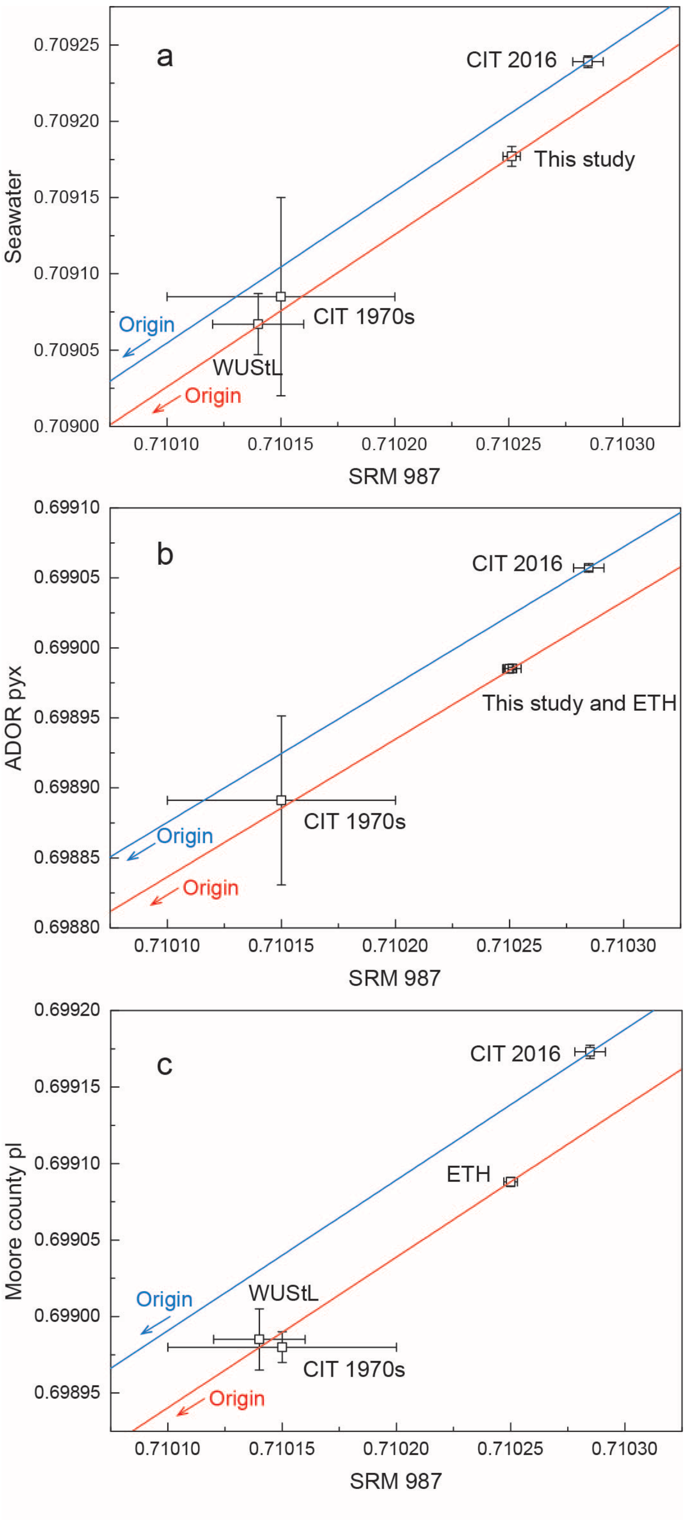

Figure 7. Comparison of the $^{87}Sr/^{86}Sr$ measurement results of several standard materials used in early Solar System $^{87}Sr/^{86}Sr$ chronology studies reported by different laboratories: (a) seawater vs. SRM 987, (b) ADOR pyroxene vs. SRM 987, (c) Moore County plagioclase vs. SRM 987. See Table 6 for the name abbreviations of the laboratories and the data sources. In

(a) and (b), the red lines are the normalization lines connecting the data points representing this study and the origin. In (c), the red line is the normalization line connecting the data point representing ETH and the origin, since Moore County plagioclase was not analysed in this study. In all the plots, blue lines are the normalization lines connecting the data point representing CIT 2016 and the origin.

Table 6 ^{87}Sr/^{86}Sr measurement results of several standard materials reported by different laboratories.

Laboratory[a]	Reference	SRM 987	2SD	Seawater[b]	2SD[b]	Moore County Pl[b,c]	2SD[b]	ADOR pyx[b,c]	2SD[b]
ANU	This study[d]	0.7102513	0.0000038	0.7091770	0.0000065	n. r.	n. r.	0.6989853	0.0000076
ETH	Hans et al., 2013	0.710250	0.000003	n. r.	n. r.	0.699088	0.000003	0.698985	0.000003
WUStL	Podosek et al., 1991[e]	0.710140	0.000020	0.709067	0.000020	0.698985	0.000020	n. r.	n. r.
CIT 2016	Papanastassiou and Chen, 2016	0.710285	0.000007	0.709239	0.000004	0.699173	0.000004	0.699057	0.000002
CIT 1970s	Papanastassiou and Wasserburg, 1973; Wasserburg et al., 1977; Gray et al., 1973	0.71015[f]	0.00005[f]	0.709085	0.000065[g]	0.69898	0.00001	0.69889	0.00006

[a] ANU = Australian National University, ETH = Eidgenössische Technische Hochschule Zürich, WUStL = Washington University St. Louis, CIT = California Institute of Technology. Data from literature are taken as originally reported without additional normalization.

[b] n. r. = not reported.

[c] Pl = plagioclase, Pyx = pyroxene.

[d] ^{87}Sr/^{86}Sr ratios are unnormalized MDFI–C ratios.

[e] Seawater and Moore County Pl data were “adjusted to an accepted SRM 987 ^{87}Sr/^{86}Sr value of 0.710140”, according to the original literature. 2SD precisions were not reported; an error of ± 0.000020 (2σ) was assigned to all measurement results, according to the original literature.

[f] 0.71015 ± 0.00005 was reported as a “preferred” SRM 987 ^{87}Sr/^{86}Sr value used for spike calibration (Papanastassiou, 2015).

[g] Total range of seawater ^{87}Sr/^{86}Sr.

5. Summary and conclusions

High-precision Sr isotope analyses were performed for the Sr standard NIST SRM 987 and a series of natural samples using a 3-line multidynamic TIMS measurement method. A linear interpolation method was developed to systematically correct the fractionation drift effect during the multidynamic measurements. The main conclusions of this study are summarized below.

(1) Among all the measurement methods, the multidynamic method with fractionation drift correction yields the best precision for both ^{84}Sr/^{86}Sr and ^{87}Sr/^{86}Sr ratios (2RSD = 29 ppm and 5 ppm respectively). During our analytical session, the reproducibility of static isotopic ratios was affected by significant Faraday cup deterioration, while the multidynamic ratios are essentially unaffected.

(2) Without correction of fractionation drift, the multidynamic μ^{87}Sr and μ^{84}Sr values of SRM 987 and terrestrial samples are correlated with fractionation rate, consistent with the theoretical predictions from the fractionation drift effect. Such correlations disappear after the effects of fractionation drift are corrected. The high fractionation rates of terrestrial samples can lead to significant overestimations of μ^{84}Sr by extents higher than the desired measurement precision of 30 ppm.

(3) Our multistatic and multidynamic μ^{84}Sr measurement results of the terrestrial samples reproduce the static–multidynamic discrepancy seen in previous studies. The discrepancy in our data can be explained by the higher fractionation rates of the terrestrial samples compared to SRM 987, and is eliminated after fractionation drift correction. We confirm that SRM 987 possesses an apparent ^{84}Sr enrichment relative to the natural samples from the Earth, and conclude that the terrestrial samples have an average μ^{84}Sr value of –31 ± 8 ppm.

(4) The two independent multidynamic ^{87}Sr/^{86}Sr ratios measured using our method exhibit a slight but resolvable offset. This offset most likely reflects the systematic errors

generated by an insufficient amplifier idle time setting during our measurements. The systematic errors can be eliminated by normalizing the isotopic ratios against the standard.

(5) The multidynamic μ^{87}Sr and μ^{84}Sr results of SRM 987 (after fractionation drift correction) show a negative correlation inconsistent with the expected correlation from ion counting random errors. This correlation also cannot be explained by inaccurate fractionation correction, because the Sr isotope fractionation behaviour in TIMS is found to be accurately described by the exponential law. The observed correlation is likely a combined effect of ion counting statistics, uncorrected (or overcorrected) fractionation drift effect, and mixing of ions evaporated from variably fractionated sample reservoirs on the filament.

(6) The measurement results of four standard materials used in previous early Solar System ^{87}Sr/^{86}Sr chronology studies reported by us, Hans et al. (2013), Podosek et al. (1991), and the California Institute of Technology laboratory in the 1970s (Papanastassiou and Wasserburg, 1973; Wasserburg et al., 1977; Gray et al., 1973) all plot along the same proportional normalization lines, indicating that the ^{87}Sr/^{86}Sr measurement results of unknown samples from these laboratories can be reliably compared after normalization to a common standard value. In contrast, the standard analytical results of Papanastassiou and Chen (2016) deviate from the normalization lines defined by all other studies, suggesting that inter-laboratory comparison with their data should be made with care.

Acknowledgements

We thank Michael Ellwood for providing the seawater sample. This project was funded through the Australian Research Council grant DP190100002 “The history of accretion in our Solar System”. We appreciate the thorough reviews and instructive comments from Marion Garçon, Tetsuya Yokoyama, and an anonymous reviewer. We also thank Don Porcelli for editorial handling.

References

Albarède, F., Telouk, P., Blichert-Toft, J., Boyet, M., Agranier, A., Nelson, B., 2004. Precise and accurate isotopic measurements using multiple-collector ICPMS. Geochimica et Cosmochimica Acta, 68(12): 2725-2744.

Amelin, Y., Davis, D.W., Davis, W.J., 2005. Decoupled fractionation of even- and odd-mass isotopes of Pb in TIMS. Geochimica Et Cosmochimica Acta, 69(10): A215-A215.

Amelin, Y., Huyskens, M., 2013. Performance of Pb Multi Ion Counting Array in Triton Plus TIMS, Goldschmidt Conference, 586.

Amelin, Y., Koefoed, P., Iizuka, T., Fernandes, V.A., Huyskens, M.H., Yin, Q.-Z., Irving, A.J., 2019. U-Pb, Rb-Sr and Ar-Ar systematics of the ungrouped achondrites Northwest Africa 6704 and Northwest Africa 6693. Geochimica et Cosmochimica Acta, 245: 628-642.

Amelin, Y., Merle, R., 2021. Isotopic analysis of potassium by total evaporation and incipient emission thermal ionisation mass spectrometry. Chemical Geology, 559: 119976.

Andreasen, R., Sharma, M., 2007. Mixing and Homogenization in the Early Solar System: Clues from Sr, Ba, Nd, and Sm Isotopes in Meteorites. The Astrophysical Journal, 665(1): 874-883.

Andreasen, R., Sharma, M., 2009. Fractionation and mixing in a thermal ionization mass spectrometer source: Implications and limitations for high-precision Nd isotope analyses. International Journal of Mass Spectrometry, 285(1): 49-57.

Archer, G.J., Mundl, A., Walker, R.J., Worsham, E.A., Bermingham, K.R., 2017. High-precision analysis of $^{182}W/^{184}W$ and $^{183}W/^{184}W$ by negative thermal ionization mass spectrometry: Per-integration oxide corrections using measured $^{18}O/^{16}O$. International journal of mass spectrometry, 414: 80-86.

Brennecka, G.A., Borg, L.E., Wadhwa, M., 2013. Evidence for supernova injection into the solar nebula and the decoupling of r-process nucleosynthesis. Proceedings of the National Academy of Sciences of the United States of America, 110(43): 17241-17246.

Burkhardt, C., Dauphas, N., Hans, U., Bourdon, B., Kleine, T., 2019. Elemental and isotopic variability in solar system materials by mixing and processing of primordial disk reservoirs. Geochimica et Cosmochimica Acta, 261: 145-170.

Carlson, R.W., 2014. 15.18 - Thermal Ionization Mass Spectrometry. In: Holland, H.D., Turekian, K.K. (Eds.), Treatise on Geochemistry (Second Edition). Elsevier, Oxford, pp. 337-354.

Caro, G., Bourdon, B., Birck, J.-L., Moorbath, S., 2003. 146Sm–142Nd evidence from Isua metamorphosed sediments for early differentiation of the Earth's mantle. Nature, 423(6938): 428-432.

Caro, G., Bourdon, B., Birck, J.-L., Moorbath, S., 2006. High-precision ^{142}Nd/^{144}Nd measurements in terrestrial rocks: Constraints on the early differentiation of the Earth’s mantle. Geochimica et Cosmochimica Acta, 70(1): 164-191.

Charlier, B.L.A., Ginibre, C., Morgan, D., Nowell, G.M., Pearson, D.G., Davidson, J.P., Ottley, C.J., 2006. Methods for the microsampling and high-precision analysis of strontium and rubidium isotopes at single crystal scale for petrological and geochronological applications. Chemical Geology, 232(3): 114-133.

Charlier, B.L.A., Parkinson, I.J., Burton, K.W., Grady, M.M., Wilson, C.J.N., Smith, E.G.C., 2017. Stable strontium isotopic heterogeneity in the solar system from double-spike data. Geochemical Perspectives Letters, 4: 35-40.

Charlier, B.L.A., Tissot, F.L.H., Dauphas, N., Wilson, C.J.N., 2019. Nucleosynthetic, radiogenic and stable strontium isotopic variations in fine- and coarse-grained refractory inclusions from Allende. Geochimica et Cosmochimica Acta, 265: 413-430.

Davis, A.M., Richter, F.M., Mendybaev, R.A., Janney, P.E., Wadhwa, M., McKeegan, K.D., 2015. Isotopic mass fractionation laws for magnesium and their effects on ^{26}Al–^{26}Mg systematics in solar system materials. Geochimica et Cosmochimica Acta, 158: 245-261.

Di, Y., Li, Z., Amelin, Y., 2021. Monitoring and quantitative evaluation of Faraday cup deterioration in a thermal ionization mass spectrometer using multidynamic analyses of laboratory standards. Journal of Analytical Atomic Spectrometry, in press.

Doucelance, R., Manhes, G., 2001. Reevaluation of precise lead isotope measurements by thermal ionization mass spectrometry: comparison with determinations by plasma source mass spectrometry. Chemical Geology, 176(1-4): 361-377.

Fukai, R., Yokoyama, T., 2019a. Assessment of the secondary instrumental fractionation in TIMS: Implication for high-precision Nd isotope analysis of geological samples. Geochemical Journal, 53(5): 333-337.

Fukai, R., Yokoyama, T., 2019b. Nucleosynthetic Sr–Nd Isotope Correlations in Chondrites: Evidence for Nebular Thermal Processing and Dust Transportation in the Early Solar System. The Astrophysical Journal, 879(2): 79.

Fukai, R., Yokoyama, T., Kagami, S., 2017. Evaluation of the long-term fluctuation in isotope ratios measured by TIMS with the static, dynamic, and multistatic methods: A case study for Nd isotope measurements. International Journal of Mass Spectrometry, 414: 1-7.

Fukami, Y., Tobita, M., Yokoyama, T., Usui, T., Moriwaki, R., 2017. Precise isotope analysis of sub-nanogram lead by total evaporation thermal ionization mass spectrometry (TE-TIMS) coupled with a ^{204}Pb–^{207}Pb double spike method. Journal of Analytical Atomic Spectrometry, 32(4): 848-857.

Garçon, M., Boyet, M., Carlson, R.W., Horan, M.F., Auclair, D., Mock, T.D., 2018. Factors influencing the precision and accuracy of Nd isotope measurements by thermal ionization mass spectrometry. Chemical Geology, 476: 493-514.

Gray, C.M., Papanastassiou, D.A., Wasserburg, G.J., 1973. The identification of early condensates from the solar nebula. Icarus, 20(2): 213-239.

Hans, U., 2013. High-precision strontium isotope measurements on meteorites: Implications for the origin and timing of volatile depletion in the inner solar system. Ph.D. thesis Thesis, ETH Zurich, Zurich.

Hans, U., Kleine, T., Bourdon, B., 2013. Rb-Sr chronology of volatile depletion in differentiated protoplanets: BABI, ADOR and ALL revisited. Earth and Planetary Science Letters, 374: 204-214.

Hart, S.R., Zindler, A., 1989. Isotope fractionation laws: a test using calcium. International Journal of Mass Spectrometry and Ion Processes, 89(2): 287-301.

Henshall, T., Cook, D.L., Garçon, M., Schönbächler, M., 2018. High-precision strontium isotope analysis of geological samples by thermal ionisation mass spectrometry. Chemical Geology, 482: 113-120.

Holden, N.E., Coplen, T.B., Böhlke, J.K., Tarbox, L.V., Benefield, J., R., d.L.J., Mahaffy, P.G., O’Connor, G., Roth, E., Tepper, D.H., Walczyk, T., Wieser, M.E., Yoneda, S., 2018. IUPAC Periodic Table of the Elements and Isotopes (IPTEI) for the Education Community (IUPAC Technical Report). Pure and Applied Chemistry, 90(12): 1833-2092.

Horan, M.F., Carlson, R.W., Walker, R.J., Jackson, M., Garçon, M., Norman, M., 2018. Tracking Hadean processes in modern basalts with 142-Neodymium. Earth and Planetary Science Letters, 484: 184-191.

Huyskens, M.H., Amelin, Y., Yin, Q.Z., 2020. Uranium Isotopic Composition of Angrites, 51st Lunar and Planetary Science Conference. Lunar and Planetary Institute, The Woodlands, Texas, Abstract #1781.

Lenz, H., Wendt, I., 1976. Use of double collector for high-precision isotope ratio measurements in geochronology, 7th International Mass Spectrometry Conference, Flornce, Italy, 565-568.

Ludwig, K.R., 1997. Optimization of multicollector isotope-ratio measurement of strontium and neodymium. Chemical Geology, 135(3): 325-334.

Makishima, A., 2016. Thermal Ionization Mass Spectrometry (TIMS): Silicate Digestion, Separation, and Measurement. John Wiley & Sons, Weinheim, Germany.

Makishima, A., Nakamura, E., 1991. Calibration of Faraday cup efficiency in a multicollector mass spectrometer. Chemical Geology: Isotope Geoscience section, 94(2): 105-110.

Maréchal, C.N., Télouk, P., Albarède, F., 1999. Precise analysis of copper and zinc isotopic compositions by plasma-source mass spectrometry. Chemical Geology, 156(1): 251-273.

Miyazaki, T., Vaglarov, B.S., Kimura, J.-I., 2016. Determination of relative Faraday cup efficiency factor using exponential law mass fractionation model for multiple collector thermal ionization mass spectrometry. Geochemical Journal, 50(5): 445-447.

Moynier, F., Day, J.M.D., Okui, W., Yokoyama, T., Bouvier, A., Walker, R.J., Podosek, F.A., 2012. Planetary-scale strontium isotopic heterogeneity and the age of volatile depletion of early Solar System materials. Astrophysical Journal, 758(1): 45.

Myojo, K., Yokoyama, T., Okabayashi, S., Wakaki, S., Sugiura, N., Iwamori, H., 2018. The Origin and Evolution of Nucleosynthetic Sr Isotope Variability in Calcium and Aluminum-rich Refractory Inclusions. The Astrophysical Journal, 853(1): 48.

O'Neil, J., Carlson, R.W., Francis, D., Stevenson, R.K., 2008. Neodymium-142 Evidence for Hadean Mafic Crust. Science, 321(5897): 1828.

Papanastassiou, D.A., 2015. Initial 87Sr/86Sr Chronology; A Journey Through 4.5 Decades, 46th Lunar and Planetary Science Conference. Lunar and Planetary Institute, The Woodlands, Texas, Abstract #2243.

Papanastassiou, D.A., Chen, J.H., 2016. Initial 87Sr/86Sr Chronology in the Solar System, 47th Lunar and Planetary Science Conference. Lunar and Planetary Institute, The Woodlands, Texas, Abstract #2650.

Papanastassiou, D.A., Wasserburg, G.J., 1973. Rb-Sr ages and initial strontium in basalts from Apollo 15. Earth and Planetary Science Letters, 17(2): 324-337.

Papanastassiou, D.A., Wasserburg, G.J., 1978. Strontium isotopic anomalies in the Allende Meteorite. Geophysical Research Letters, 5(7): 595-598.

Paton, C., Schiller, M., Bizzarro, M., 2013. Identification of an Sr-84-depleted carrier in primitive meteorites and implications for thermal processing in the solar protoplanetary disk. Astrophysical Journal Letters, 763(2): L40.

Podosek, F.A., Prombo, C.A., Amari, S., Lewis, R.S., 2004. s - Process Sr Isotopic Compositions in Presolar SiC from the Murchison Meteorite. The Astrophysical Journal, 605(2): 960-965.

Podosek, F.A., Zinner, E.K., MacPherson, G.J., Lundberg, L.L., Brannon, J.C., Fahey, A.J., 1991. Correlated study of initial Sr-87/Sr-86 and Al-Mg isotopic systematics and petrologic properties in a suite of refractory inclusions from the Allende meteorite. Geochimica et Cosmochimica Acta, 55(4): 1083-1110.

Qin, L., Carlson, R.W., Alexander, C.M.O.D., 2011. Correlated nucleosynthetic isotopic variability in Cr, Sr, Ba, Sm, Nd and Hf in Murchison and QUE 97008. Geochimica et Cosmochimica Acta, 75(24): 7806-7828.

Roth, A.S.G., Bourdon, B., Mojzsis, S.J., Touboul, M., Sprung, P., Guitreau, M., Blichert-Toft, J., 2013. Inherited ^{142}Nd anomalies in Eoarchean protoliths. Earth and Planetary Science Letters, 361: 50-57.

Roth, A.S.G., Scherer, E.E., Maden, C., Mezger, K., Bourdon, B., 2014. Revisiting the 142Nd deficits in the 1.48Ga Khariar alkaline rocks, India. Chemical Geology, 386: 238-248.

Sharma, M., Papanastassiou, D.A., Wasserburg, G.J., Dymek, R.F., 1996. The issue of the terrestrial record of ^{146}Sm. Geochimica et Cosmochimica Acta, 60(11): 2037-2047.

Shollenberger, Q.R., Borg, L.E., Render, J., Ebert, S., Bischoff, A., Russell, S.S., Brennecka, G.A., 2018. Isotopic coherence of refractory inclusions from CV and CK meteorites: Evidence from multiple isotope systems. Geochimica Et Cosmochimica Acta, 228: 62-80.

Thirlwall, M.F., 1991. Long-term reproducibility of multicollector Sr and Nd isotope ratio analysis. Chemical Geology: Isotope Geoscience section, 94(2): 85-104.

Thirlwall, M.F., 2000. Inter-laboratory and other errors in Pb isotope analyses investigated using a Pb-207-Pb-204 double spike. Chemical Geology, 163(1-4): 299-322.

Thirlwall, M.F., Anczkiewicz, R., 2004. Multidynamic isotope ratio analysis using MC–ICP–MS and the causes of secular drift in Hf, Nd and Pb isotope ratios. International Journal of Mass Spectrometry, 235(1): 59-81.

Trinquier, A., Birck, J.-L., Allègre, C.J., 2008. High-precision analysis of chromium isotopes in terrestrial and meteorite samples by thermal ionization mass spectrometry. Journal of Analytical Atomic Spectrometry, 23(12): 1565-1574.

Trinquier, A., Bouman, C., Schwieters, J., Lloyd, N., 2013. 10^{12} Ω amplifiers for high precision isotope ratio measurements of small sample sizes. Technical Note 30249, Thermo Fisher Scientific, Bremen, Germany.

Upadhyay, D., Scherer, E.E., Mezger, K., 2008. Fractionation and mixing of Nd isotopes during thermal ionization mass spectrometry: implications for high precision 142Nd/144Nd analyses. Journal of Analytical Atomic Spectrometry, 23(4): 561-568.

Vance, D., Thirlwall, M., 2002. An assessment of mass discrimination in MC-ICPMS using Nd isotopes. Chemical Geology, 185(3): 227-240.

Wasserburg, G.J., Tera, F., Papanastassiou, D.A., Huneke, J.C., 1977. Isotopic and chemical investigations on Angra-Dos-Reis. Earth and Planetary Science Letters, 35(2): 294-316.

Wasserburg, G.J., Wimpenny, J., Yin, Q.Z., 2012. Mg isotopic heterogeneity, Al-Mg isochrons, and canonical 26Al/27Al in the early solar system. Meteoritics & Planetary Science, 47(12): 1980-1997.

Wendt, I., Haase, G., 1998. Dynamic double collector measurement with cup efficiency factor determination. Chemical Geology, 146(1): 99-110.

Wielandt, D., Bizzarro, M., 2011. A TIMS-based method for the high precision measurements of the three-isotope potassium composition of small samples. Journal of Analytical Atomic Spectrometry, 26(2): 366-377.

Wieser, M.E., Schwieters, J.B., 2005. The development of multiple collector mass spectrometry for isotope ratio measurements. International Journal of Mass Spectrometry, 242(2): 97-115.

Yobregat, E., Fitoussi, C., Bourdon, B., 2017. A new method for TIMS high precision analysis of Ba and Sr isotopes for cosmochemical studies. Journal of Analytical Atomic Spectrometry, 32(7): 1388-1399.

Yokoyama, T., Fukami, Y., Okui, W., Ito, N., Yamazaki, H., 2015. Nucleosynthetic strontium isotope anomalies in carbonaceous chondrites. Earth and Planetary Science Letters, 416: 46-55.

York, D., Evensen, N.M., Martínez, M.L., De Basabe Delgado, J., 2004. Unified equations for the slope, intercept, and standard errors of the best straight line. American Journal of Physics, 72(3): 367-375.

Young, E.D., Galy, A., Nagahara, H., 2002. Kinetic and equilibrium mass-dependent isotope fractionation laws in nature and their geochemical and cosmochemical significance. Geochimica et Cosmochimica Acta, 66(6): 1095-1104.

High-precision multidynamic Sr isotope analysis using thermal ionization mass spectrometer (TIMS) with correction of fractionation drift

Yankun Di*, Evgenii Krestianinov, Sonja Zink, Yuri Amelin

Research School of Earth Sciences, Australian National University, Acton, ACT 2601, Australia

*Corresponding author, email: yankun.di@anu.edu.au

Supplementary Materials

This supplementary file contains:

Appendix A. Detailed data processing and statistical treatment procedures

At the first stage of data processing, a fractionation trajectory of block average line 1 ^{88}Sr/^{86}Sr vs. block number was plotted and checked visually. Blocks at the beginning and/or the end of the measurement where the fractionation was changing rapidly or reversing were removed to minimize the effect of secondary mass fractionation resulted from domain mixing (see section 4.5.5 in the main text, Garçon et al., 2018; Upadhyay et al., 2008; Andreasen and Sharma, 2009) and to ensure the accurate estimation of average fractionation rates. These blocks are usually measured at low ion beam intensities, and are thus associated with large standard errors of fractionation-corrected isotopic ratios. In the cases where a reverse fractionation occurred in the middle of a measurement, or the fractionation behaviour switched from normal to reverse several times during the run, or a too large fraction of the measurement (e.g., >1/4 of the total run) need to be removed, the entire measurement was discarded.

A.1 Calculation of fractionation-corrected cycle isotopic ratios

For each measurement cycle, six ^{84}Sr/^{86}Sr ratios and ten ^{87}Sr/^{86}Sr ratios were calculated using four different methods: static, multistatic (MS), multidynamic without fractionation interpolation (MD), and multidynamic with fractionation interpolation (MDFI).

A.1.1 Static and multistatic Sr isotopic ratios

The static ^{84}Sr/^{86}Sr and ^{87}Sr/^{86}Sr ratios of the 3 magnetic settings (lines) were calculated by correcting mass fractionation to ^{88}Sr/^{86}Sr = 8.375209 using the exponential law (Thirlwall, 1991) following the equations:

$$({}^{84}\mathrm{Sr}/{}^{86}\mathrm{Sr})_{\mathrm{c,static\ line}\ i} = ({}^{84}\mathrm{Sr}/{}^{86}\mathrm{Sr})_{\mathrm{m,line}\ i} \cdot [\frac{8.375209}{({}^{88}\mathrm{Sr}/{}^{86}\mathrm{Sr})_{\mathrm{m,line}\ i}}]^{\beta_{84}} \quad (1a)$$

$$({}^{87}\mathrm{Sr}/{}^{86}\mathrm{Sr})_{\mathrm{c,static\ line}\ i} = ({}^{87}\mathrm{Sr}/{}^{86}\mathrm{Sr})_{\mathrm{m,line}\ i} \cdot [\frac{8.375209}{({}^{88}\mathrm{Sr}/{}^{86}\mathrm{Sr})_{\mathrm{m,line}\ i}}]^{\beta_{87}} \quad (1b)$$

where "c" and "m" denotes "corrected" and "measured" respectively; i = 1, 2, or 3; $\beta_{84} = \frac{\ln(\mathrm{M}_{^{84}\mathrm{Sr}}/\mathrm{M}_{^{86}\mathrm{Sr}})}{\ln(\mathrm{M}_{^{88}\mathrm{Sr}}/\mathrm{M}_{^{86}\mathrm{Sr}})} = -1.02325$ and $\beta_{87} = \frac{\ln(\mathrm{M}_{^{87}\mathrm{Sr}}/\mathrm{M}_{^{86}\mathrm{Sr}})}{\ln(\mathrm{M}_{^{88}\mathrm{Sr}}/\mathrm{M}_{^{86}\mathrm{Sr}})} = 0.50359$, which were calculated using the relative atomic masses (M) of isotopes from the International Union of Pure and Applied Chemistry (IUPAC) Periodic Table of the Elements and Isotopes (IPTEI) (Holden et al., 2018): $\mathrm{M}_{^{84}\mathrm{Sr}} = 83.91343$, $\mathrm{M}_{^{86}\mathrm{Sr}} = 85.90927$, $\mathrm{M}_{^{87}\mathrm{Sr}} = 86.90888$, $\mathrm{M}_{^{88}\mathrm{Sr}} = 87.90562$.

In the static calculation, three Faraday cup efficiencies are involved in each fractionation-corrected isotopic ratio. For example, considering that Faraday cup efficiency (C) is defined as the ratio of the current flowing through the amplifier connected to the Faraday cup to the ion current injected into the Faraday cup, i.e., the measured/true ion beam current ($\mathrm{I}_{\mathrm{measured}}/\mathrm{I}_{\mathrm{true}}$), equation ($1a$) for line 1 can be rewritten as:

$$({}^{84}\mathrm{Sr}/{}^{86}\mathrm{Sr})_{\mathrm{c,static\ line\ 1}} = (\frac{\mathrm{I}_{^{84}\mathrm{Sr}}}{\mathrm{I}_{^{86}\mathrm{Sr}}})_{\mathrm{true,line\ 1}} \cdot (\frac{\mathrm{C}_{\mathrm{L1}}}{\mathrm{C}_{\mathrm{H1}}}) \cdot [\frac{8.375209}{(\frac{\mathrm{I}_{^{88}\mathrm{Sr}}}{\mathrm{I}_{^{86}\mathrm{Sr}}})_{\mathrm{true,line\ 1}} \cdot (\frac{\mathrm{C}_{\mathrm{H3}}}{\mathrm{C}_{\mathrm{H1}}})}]^{\beta_{84}}$$

$$= (\frac{\mathrm{I}_{^{84}\mathrm{Sr}}}{\mathrm{I}_{^{86}\mathrm{Sr}}})_{\mathrm{true,line\ 1}} \cdot [\frac{8.375209}{(\frac{\mathrm{I}_{^{88}\mathrm{Sr}}}{\mathrm{I}_{^{86}\mathrm{Sr}}})_{\mathrm{true,line\ 1}}}]^{\beta_{84}} \cdot \mathrm{C}_{\mathrm{L1}} \cdot \mathrm{C}_{\mathrm{H3}}^{-\beta_{84}} \cdot \mathrm{C}_{\mathrm{H1}}^{-1+\beta_{84}}$$

$$= ({}^{84}\mathrm{Sr}/{}^{86}\mathrm{Sr})_{\mathrm{c,true,line\ 1}} \cdot \mathrm{C}_{\mathrm{L1}} \cdot \mathrm{C}_{\mathrm{H3}}^{-\beta_{84}} \cdot \mathrm{C}_{\mathrm{H1}}^{-1+\beta_{84}} \qquad (1c)$$

where the "true" $^{84}\mathrm{Sr}/^{86}\mathrm{Sr}$ ratio refers to the fractionation-corrected static $^{84}\mathrm{Sr}/^{86}\mathrm{Sr}$ ratio when all Faraday cup efficiencies are unity. The equations for other lines can be rewritten with cup efficiencies similarly. Because amplifier gains were calibrated before each measurement, and the "amplifier rotation" function of Triton was activated to average the gain differences between amplifiers, the differences in amplifier gains are considered negligible here. The partial derivative of equation ($1c$) yields $\frac{\partial({}^{84}\mathrm{Sr}/{}^{86}\mathrm{Sr})_{\mathrm{c,static\ line\ 1}}}{({}^{84}\mathrm{Sr}/{}^{86}\mathrm{Sr})_{\mathrm{c,static\ line\ 1}}} / \frac{\partial \mathrm{C}_{\mathrm{L1}}}{\mathrm{C}_{\mathrm{L1}}} = 1$, $\frac{\partial({}^{84}\mathrm{Sr}/{}^{86}\mathrm{Sr})_{\mathrm{c,static\ line\ 1}}}{({}^{84}\mathrm{Sr}/{}^{86}\mathrm{Sr})_{\mathrm{c,static\ line\ 1}}} / \frac{\partial \mathrm{C}_{\mathrm{H3}}}{\mathrm{C}_{\mathrm{H3}}} = -\beta_{84} = 1.02325$, and $\frac{\partial({}^{84}\mathrm{Sr}/{}^{86}\mathrm{Sr})_{\mathrm{c,static\ line\ 1}}}{({}^{84}\mathrm{Sr}/{}^{86}\mathrm{Sr})_{\mathrm{c,static\ line\ 1}}} / \frac{\partial \mathrm{C}_{\mathrm{H1}}}{\mathrm{C}_{\mathrm{H1}}} = -1 + \beta_{84} = -2.02325$. Therefore, 100%, 102%, and –202% of the efficiency changes of cup L1, H3, and H1 can be propagated into the calculated $^{84}\mathrm{Sr}/^{86}\mathrm{Sr}$ ratio respectively.

The multistatic (MS) isotopic ratios were calculated by taking the arithmetic mean of the static isotopic ratios from the 3 lines, following the convention in the TIMS community (e.g., Fukai et al., 2017; Caro et al., 2006; Hans et al., 2013; Trinquier et al., 2008):

$$({}^{84}\mathrm{Sr}/{}^{86}\mathrm{Sr})_{\mathrm{c,MS}} = \frac{1}{3} \cdot \sum_{i=1}^{3} ({}^{84}\mathrm{Sr}/{}^{86}\mathrm{Sr})_{\mathrm{c,static\ line}\ i} \qquad (2a)$$

$$({}^{87}\mathrm{Sr}/{}^{86}\mathrm{Sr})_{\mathrm{c,MS}} = \frac{1}{3} \cdot \sum_{i=1}^{3} ({}^{87}\mathrm{Sr}/{}^{86}\mathrm{Sr})_{\mathrm{c,static\ line}\ i} \qquad (2b)$$

A.1.2 Multidynamic Sr isotopic ratios without fractionation interpolation

The simple multidynamic (MD) ^{84}Sr/^{86}Sr ratio was also calculated by correcting the instrumental mass fractionation using the exponential law. Unlike the static measurement described by equation (1*a*), the ^{84}Sr/^{86}Sr ratio measured at line 1 and the ^{88}Sr/^{86}Sr ratio measured at line 3, which were sequentially measured using the same combination of Faraday cups H1 + L1, were used in the calculation:

$$({}^{84}\mathrm{Sr}/{}^{86}\mathrm{Sr})_{\mathrm{c,MD}} = ({}^{84}\mathrm{Sr}/{}^{86}\mathrm{Sr})_{\mathrm{m,line\ 1}} \cdot \left[\frac{8.375209}{({}^{88}\mathrm{Sr}/{}^{86}\mathrm{Sr})_{\mathrm{m,line\ 3}}}\right]^{\beta_{84}} \qquad (3a)$$

where $\beta_{84} = -1.02325$. Equation (3*a*) can be rewritten with Faraday cup efficiencies:

$$({}^{84}\mathrm{Sr}/{}^{86}\mathrm{Sr})_{\mathrm{c,MD}} = \left(\frac{\mathrm{I}_{{}^{84}\mathrm{Sr}}}{\mathrm{I}_{{}^{86}\mathrm{Sr}}}\right)_{\mathrm{true,line\ 1}} \cdot \left(\frac{\mathrm{C_{L1}}}{\mathrm{C_{H1}}}\right) \cdot \left[\frac{8.375209}{\left(\frac{\mathrm{I}_{{}^{88}\mathrm{Sr}}}{\mathrm{I}_{{}^{86}\mathrm{Sr}}}\right)_{\mathrm{true,line\ 3}} \cdot \left(\frac{\mathrm{C_{H1}}}{\mathrm{C_{L1}}}\right)}\right]^{\beta_{84}}$$

$$= \left(\frac{\mathrm{I}_{{}^{84}\mathrm{Sr}}}{\mathrm{I}_{{}^{86}\mathrm{Sr}}}\right)_{\mathrm{true,line\ 1}} \cdot \left[\frac{8.375209}{\left(\frac{\mathrm{I}_{{}^{88}\mathrm{Sr}}}{\mathrm{I}_{{}^{86}\mathrm{Sr}}}\right)_{\mathrm{true,line\ 3}}}\right]^{\beta_{84}} \cdot \left(\frac{\mathrm{C_{L1}}}{\mathrm{C_{H1}}}\right)^{1+\beta_{84}} \qquad (3b)$$

The partial derivative of equation (3*b*) yields $\frac{\partial({}^{84}\mathrm{Sr}/{}^{86}\mathrm{Sr})_{\mathrm{c,MD}}}{({}^{84}\mathrm{Sr}/{}^{86}\mathrm{Sr})_{\mathrm{c,MD}}} / \frac{\partial(\frac{\mathrm{C_{L1}}}{\mathrm{C_{H1}}})}{(\frac{\mathrm{C_{L1}}}{\mathrm{C_{H1}}})} = 1 + \beta_{84} = -0.02325$. Therefore, only ca. 2.3% of the relative cup efficiency $\mathrm{C_{L1}}/\mathrm{C_{H1}}$ can be propagated into the MD ^{84}Sr/^{86}Sr ratio, and the remaining 97.7% is mathematically cancelled during the multidynamic fractionation correction.

Two MD ^{87}Sr/^{86}Sr ratios can be calculated in our 3-line method using combined lines 1 + 2 and lines 2 + 3. The first multidynamic ratio, $(^{87}\mathrm{Sr}/^{86}\mathrm{Sr})_{\mathrm{c,MD-A}}$, was calculated by taking the geometric mean of the measured ^{87}Sr/^{86}Sr ratios of line 1 and line 2, followed by mass fractionation correction using the measured ^{88}Sr/^{86}Sr ratio of line 2:

$$(^{87}\mathrm{Sr}/^{86}\mathrm{Sr})_{\mathrm{c,MD-A}} = \sqrt{(^{87}\mathrm{Sr}/^{86}\mathrm{Sr})_{\mathrm{m,line\,1}} \cdot (^{87}\mathrm{Sr}/^{86}\mathrm{Sr})_{\mathrm{m,line\,2}}}$$

$$\cdot \left[\frac{8.375209}{(^{88}\mathrm{Sr}/^{86}\mathrm{Sr})_{\mathrm{m,line\,2}}}\right]^{\beta_{87}} \quad (4a)$$

where $\beta_{87} = 0.50359$. Considering Faraday cup efficiencies, equation (4*a*) can be rewritten as:

$$(^{87}\mathrm{Sr}/^{86}\mathrm{Sr})_{\mathrm{c,MD-A}} = \sqrt{\left(\frac{\mathrm{I}_{^{87}\mathrm{Sr}}}{\mathrm{I}_{^{86}\mathrm{Sr}}}\right)_{\mathrm{true,line\,1}} \cdot \left(\frac{\mathrm{C_{H2}}}{\mathrm{C_{H1}}}\right) \cdot \left(\frac{\mathrm{I}_{^{87}\mathrm{Sr}}}{\mathrm{I}_{^{86}\mathrm{Sr}}}\right)_{\mathrm{true,line\,2}} \cdot \left(\frac{\mathrm{C_{H1}}}{\mathrm{C_{Ax}}}\right)}$$

$$\cdot \left[\frac{8.375209}{\left(\frac{\mathrm{I}_{^{88}\mathrm{Sr}}}{\mathrm{I}_{^{86}\mathrm{Sr}}}\right)_{\mathrm{true,line\,2}} \cdot \left(\frac{\mathrm{C_{H2}}}{\mathrm{C_{Ax}}}\right)}\right]^{\beta_{87}}$$

$$= \sqrt{\left(\frac{\mathrm{I}_{^{87}\mathrm{Sr}}}{\mathrm{I}_{^{86}\mathrm{Sr}}}\right)_{\mathrm{true,line\,1}} \cdot \left(\frac{\mathrm{I}_{^{87}\mathrm{Sr}}}{\mathrm{I}_{^{86}\mathrm{Sr}}}\right)_{\mathrm{true,line\,2}}} \cdot \left[\frac{8.375209}{\left(\frac{\mathrm{I}_{^{88}\mathrm{Sr}}}{\mathrm{I}_{^{86}\mathrm{Sr}}}\right)_{\mathrm{true,line\,2}}}\right]^{\beta_{87}}$$

$$\cdot \left(\frac{\mathrm{C_{H2}}}{\mathrm{C_{Ax}}}\right)^{0.5-\beta_{87}} \quad (4b)$$

Equation (4*b*) completely cancelled out the efficiency of cup H1 by taking the geometric mean of ^{87}Sr/^{86}Sr ratios measured in line 1 and line 2. The partial derivative of equation (4*b*) yields $\frac{\partial(^{87}\mathrm{Sr}/^{86}\mathrm{Sr})_{\mathrm{c,MD-A}}}{(^{87}\mathrm{Sr}/^{86}\mathrm{Sr})_{\mathrm{c,MD-A}}} / \frac{\partial\left(\frac{\mathrm{C_{H2}}}{\mathrm{C_{Ax}}}\right)}{\left(\frac{\mathrm{C_{H2}}}{\mathrm{C_{Ax}}}\right)} = 0.5 - \beta_{87} = -0.00359$. Therefore, ca. 99.6% of the relative cup efficiency $\mathrm{C_{H2}}/\mathrm{C_{Ax}}$ is mathematically cancelled. Our MD ^{87}Sr/^{86}Sr equation is different from the multidynamic ^{87}Sr/^{86}Sr equations used in previous studies (Thirlwall, 1991; Hans et al., 2013; Yobregat et al., 2017; Wendt and Haase, 1998; Carlson, 2014). Their calculation employed the ^{87}Sr/^{86}Sr and ^{87}Sr/^{88}Sr ratios measured at two lines using the same pair of Faraday cups. Their calculations lead to $\frac{\partial(^{87}\mathrm{Sr}/^{86}\mathrm{Sr})_c}{(^{87}\mathrm{Sr}/^{86}\mathrm{Sr})_c} / \frac{\partial(\frac{C_1}{C_2})}{(\frac{C_1}{C_2})} = \frac{1+\beta'_{87}}{1-\beta'_{87}} = -0.00718$, where $\beta'_{87} = \frac{\ln(M_{^{87}\mathrm{Sr}}/M_{^{86}\mathrm{Sr}})}{\ln(M_{^{87}\mathrm{Sr}}/M_{^{88}\mathrm{Sr}})} = -1.01446$; C_1 and C_2 are the efficiencies of the two cups involved. Our equation (4*a*) is thus a factor of 2 more effective in removing the cup efficiency components than the previous equations. The second multidynamic $^{87}\mathrm{Sr}/^{86}\mathrm{Sr}$ ratio, $(^{87}\mathrm{Sr}/^{86}\mathrm{Sr})_{\mathrm{c,MD\text{–}B}}$, was calculated using the measured $^{87}\mathrm{Sr}/^{86}\mathrm{Sr}$ ratios of line 2 and line 3, and the measured $^{88}\mathrm{Sr}/^{86}\mathrm{Sr}$ ratio of line 3:

$$(^{87}\mathrm{Sr}/^{86}\mathrm{Sr})_{\mathrm{c,MD\text{-}B}} = \sqrt{(^{87}\mathrm{Sr}/^{86}\mathrm{Sr})_{\mathrm{m,line\,2}} \cdot (^{87}\mathrm{Sr}/^{86}\mathrm{Sr})_{\mathrm{m,line\,3}}}$$

$$\cdot \left[\frac{8.375209}{(^{88}\mathrm{Sr}/^{86}\mathrm{Sr})_{\mathrm{m,line\,3}}}\right]^{\beta_{87}} \quad (4c)$$

where $\beta_{87} = 0.50359$. The final MD $^{87}\mathrm{Sr}/^{86}\mathrm{Sr}$ ratio was calculated by taking the geometric mean of $(^{87}\mathrm{Sr}/^{86}\mathrm{Sr})_{\mathrm{c,MD\text{–}A}}$ and $(^{87}\mathrm{Sr}/^{86}\mathrm{Sr})_{\mathrm{c,MD\text{–}B}}$, following Thirlwall (1991):

$$(^{87}\mathrm{Sr}/^{86}\mathrm{Sr})_{\mathrm{c,MD\text{-}C}} = \sqrt{(^{87}\mathrm{Sr}/^{86}\mathrm{Sr})_{\mathrm{c,MD\text{-}A}} \cdot (^{87}\mathrm{Sr}/^{86}\mathrm{Sr})_{\mathrm{c,MD\text{-}B}}} \quad (4d)$$

We note that both arithmetic mean (e.g., Hans et al., 2013; Garçon et al., 2018) and geometric mean (e.g., Thirlwall, 1991) have been used in literature to synthesize the multiple multidynamic isotopic ratios derived from different combinations of lines in a measurement cycle, but no specific rationale was provided. Here we chose to use the geometric mean so that the $(^{87}\mathrm{Sr}/^{86}\mathrm{Sr})_{\mathrm{c,MD\text{–}C}}$ ratio is directly scale to a simple cup efficiency term $(\frac{C_{H2} \cdot C_{H1}}{C_{Ax} \cdot C_{L1}})^{0.5-\beta_{87}}$, which is convenient for the subsequent quantitative modelling (see section 4.3 in the main text). In fact, the difference between arithmetic mean and geometric mean is well negligible compared to the analytical uncertainties, because the two MD $^{87}\mathrm{Sr}/^{86}\mathrm{Sr}$ ratios A and B are close enough. A relative difference of 7 ppm between the ratios A and B only causes a relative difference of 6 ppt between their arithmetic mean and geometric mean.

A.1.3 Multidynamic Sr isotopic ratios with fractionation interpolation

The MDFI ^{84}Sr/^{86}Sr and ^{87}Sr/^{86}Sr ratios were calculated in similar ways as the MD ratios, but with a linear interpolation applied to the ^{88}Sr/^{86}Sr ratios before fractionation correction. In the MDFI ^{84}Sr/^{86}Sr calculation for the cycle (k+1) in a block (k = 1, 2, …, 9), the ^{88}Sr/^{86}Sr ratio used for fractionation correction was determined by interpolating the line 3 ^{88}Sr/^{86}Sr ratio at the 1/3 point between cycle k and cycle (k+1) (i.e., 2 lines back, at the same time when ^{84}Sr/^{86}Sr was measured at line 1):

$$(^{88}\mathrm{Sr}/^{86}\mathrm{Sr})_{\mathrm{FI\ line\ 3}\rightarrow 1}[\mathrm{cycle}\ (k+1)]$$
$$=\frac{2}{3}(^{88}\mathrm{Sr}/^{86}\mathrm{Sr})_{\mathrm{m,line\ 3}}[\mathrm{cycle}\ k]+\frac{1}{3}(^{88}\mathrm{Sr}/^{86}\mathrm{Sr})_{\mathrm{m,line\ 3}}[\mathrm{cycle}\ (k+1)] \quad (5)$$

This interpolation method assumes that $(^{88}\mathrm{Sr}/^{86}\mathrm{Sr})_{\mathrm{m,line\ 3}}$ varied linearly along with time during a cycle. Replacing the $(^{88}\mathrm{Sr}/^{86}\mathrm{Sr})_{\mathrm{m,line\ 3}}$ in equation (3*a*) with the interpolated ^{88}Sr/^{86}Sr given by equation (5), the MDFI ^{84}Sr/^{86}Sr ratio of the cycle (k+1) of a block (k = 1, 2, …, 9) was calculated as:

$$(^{84}\mathrm{Sr}/^{86}\mathrm{Sr})_{\mathrm{c,MDFI}}=(^{84}\mathrm{Sr}/^{86}\mathrm{Sr})_{\mathrm{m,line\ 1}}\cdot\left[\frac{8.375209}{(^{88}\mathrm{Sr}/^{86}\mathrm{Sr})_{\mathrm{FI\ line\ 3}\rightarrow 1}}\right]^{\beta_{84}} \quad (6)$$

where $\beta_{84} = -1.02325$. No fractionation interpolation and MDFI calculation were made for the first cycle of each block.

In the MD ^{87}Sr/^{86}Sr calculation equations (4*a*) and (4*c*), the geometric means of the ^{87}Sr/^{86}Sr ratios measured at lines 1, 2 or lines 2, 3 can be regarded as hypothesized ^{87}Sr/^{86}Sr ratios "measured" at the midpoints of two lines (i.e., at line "1.5" or line "2.5"). Therefore, the ^{88}Sr/^{86}Sr ratios used for the MDFI ^{87}Sr/^{86}Sr calculations of the cycle (k+1) of a block (k = 1, 2, …, 9) were calculated by interpolating the line 2 and line 3 ^{88}Sr/^{86}Sr ratios at the corresponding 5/6 points between cycle k and cycle (k+1) (i.e., 0.5 lines back), assuming that they evolved linearly along with time during a cycle:

$$(^{88}\mathrm{Sr}/^{86}\mathrm{Sr})_{\mathrm{FI\ line\ 2}\rightarrow 1.5}[\mathrm{cycle}\ (k+1)]$$
$$=\frac{1}{6}(^{88}\mathrm{Sr}/^{86}\mathrm{Sr})_{\mathrm{m,line\ 2}}[\mathrm{cycle}\ k]+\frac{5}{6}(^{88}\mathrm{Sr}/^{86}\mathrm{Sr})_{\mathrm{m,line\ 2}}[\mathrm{cycle}\ (k+1)] \quad (7a)$$

$$({}^{88}\mathrm{Sr}/{}^{86}\mathrm{Sr})_{\mathrm{FI\ line\ 3\to2.5}}[\mathrm{cycle}\ (k+1)]$$

$$=\frac{1}{6}({}^{88}\mathrm{Sr}/{}^{86}\mathrm{Sr})_{\mathrm{m,line\ 3}}[\mathrm{cycle}\ k]+\frac{5}{6}({}^{88}\mathrm{Sr}/{}^{86}\mathrm{Sr})_{\mathrm{m,line\ 3}}[\mathrm{cycle}\ (k+1)] \quad (7b)$$

The MDFI ^{87}Sr/^{86}Sr ratios of the cycle (k+1) of a block (k = 1, 2, …, 9) were then calculated by:

$$({}^{87}\mathrm{Sr}/{}^{86}\mathrm{Sr})_{\mathrm{c,MDFI-A}}=\sqrt{({}^{87}\mathrm{Sr}/{}^{86}\mathrm{Sr})_{\mathrm{m,line\ 1}}\cdot({}^{87}\mathrm{Sr}/{}^{86}\mathrm{Sr})_{\mathrm{m,line\ 2}}}$$

$$\cdot\left[\frac{8.375209}{({}^{88}\mathrm{Sr}/{}^{86}\mathrm{Sr})_{\mathrm{FI\ line\ 2\to1.5}}}\right]^{\beta_{87}} \quad (8a)$$

$$({}^{87}\mathrm{Sr}/{}^{86}\mathrm{Sr})_{\mathrm{c,MDFI-B}}=\sqrt{({}^{87}\mathrm{Sr}/{}^{86}\mathrm{Sr})_{\mathrm{m,line\ 2}}\cdot({}^{87}\mathrm{Sr}/{}^{86}\mathrm{Sr})_{\mathrm{m,line\ 3}}}$$

$$\cdot\left[\frac{8.375209}{({}^{88}\mathrm{Sr}/{}^{86}\mathrm{Sr})_{\mathrm{FI\ line\ 3\to2.5}}}\right]^{\beta_{87}} \quad (8b)$$

$$({}^{87}\mathrm{Sr}/{}^{86}\mathrm{Sr})_{\mathrm{c,MDFI-C}}=\sqrt{({}^{87}\mathrm{Sr}/{}^{86}\mathrm{Sr})_{\mathrm{c,MDFI-A}}\cdot({}^{87}\mathrm{Sr}/{}^{86}\mathrm{Sr})_{\mathrm{c,MDFI-B}}} \quad (8c)$$

where β_{87} = 0.50359. No interpolation and MDFI calculation were made for the first cycle of each block.

A.2 Calculation of block average isotopic ratio and standard error

Once the cycle isotopic ratios were calculated, the block average isotopic ratios and their standard errors were derived by:

$$\bar{x}_{\mathrm{block}}=\frac{1}{n}\sum_{k=11-n}^{10}x_{\mathrm{cycle}\ k} \quad (9)$$

$$s_{\mathrm{block}}=\sqrt{\frac{\sum_{k=11-n}^{10}(x_{\mathrm{cycle}\ k}-\bar{x}_{\mathrm{block}})^2}{n\cdot(n-1)}} \quad (10)$$

where $x_{\mathrm{cycle}\ k}$ is the fractionation-corrected isotopic ratio of the kth cycle in a block; $\bar{x}_{\mathrm{block}}$ is the block average isotopic ratio; s_{block} is the standard error of the block average value; n = 10 for the static, MS, and MD ^{84}Sr/^{86}Sr and ^{87}Sr/^{86}Sr ratios, while n = 9 for the MDFI ratios. The block standard error quantifies how close the block average value is to the true value through *t*-distribution (degree of freedom = 9 or 8; see Appendix F for details). The term "standard error" used here has the same definition as the "experimental standard deviation of the mean" in the *Guide to the Expression of Uncertainty in Measurement* (GUM) published by the Joint Committee for Guides in Metrology (JCGM) (https://www.bipm.org/utils/common/documents/jcgm/JCGM_100_2008_E.pdf), and is used as a measure of uncertainty.

A.3 Calculation of sample weighted average isotopic ratio, weighted standard error, and weighted MSWD

The sample average isotopic ratios were calculated by averaging the block average isotopic ratios weighted by the squared reciprocals of their standard errors:

$$\bar{x}_{\text{sample}} = \frac{\sum_{k=1}^{N}[\bar{x}_{\text{block}\,k} \cdot (1/s_{\text{block}\,k}^2)]}{\sum_{k=1}^{N}(1/s_{\text{block}\,k}^2)} \qquad (11)$$

where $\bar{x}_{\text{block}\,k}$ and $s_{\text{block}\,k}$ are determined using equations (9) and (10); *N* is the number of blocks in the measurement. Equation (11) ensures that larger weights are assigned to more precisely measured blocks, and as a consequence, the sample average isotopic ratios are insensitive to the poorly analysed blocks associated with large standard errors, which may result from low ion beam intensities or accidental noises.

The weighted standard error of $\bar{x}_{\text{sample}}$ was calculated as:

$$s_{\text{sample}} = \sqrt{\frac{1}{N} \cdot \frac{\sum_{k=1}^{N}(1/s_{\text{block}\,k}^2) \cdot \sum_{k=1}^{N}[(\bar{x}_{\text{block}\,k} - \bar{x}_{\text{sample}})^2 \cdot (1/s_{\text{block}\,k}^2)]}{[\sum_{k=1}^{N}(1/s_{\text{block}\,k}^2)]^2 - \sum_{k=1}^{N}(1/s_{\text{block}\,k}^2)^2}} \qquad (12)$$

The sample standard error s_{sample} quantifies how close the sample average value $\bar{x}_{\text{sample}}$ is to the true value through *t*-distribution (degree of freedom = *N* – 1, or normal distribution when *N* is sufficiently large), and $\bar{x}_{\text{sample}} \pm 2 \cdot s_{\text{sample}}$ approximately represents a 95% confidence interval of the true isotopic ratio of the sample. The sample standard error ("internal precision”) is also an estimate of the standard deviation of the repetitive analyses of the same sample (“external precision”) when N is sufficiently large (Thirlwall, 1991).

When multiple repetitive analyses of the same sample are pooled together, the pooled weighted average isotopic ratios and weighted standard errors were calculated using equations similar to (11) and (12):

$$\bar{x}_{\text{pooled}} = \frac{\sum_{k=1}^{N}[\bar{x}_{\text{sample }k} \cdot (1/s_{\text{sample }k}^{2})]}{\sum_{k=1}^{N}(1/s_{\text{sample }k}^{2})} \qquad (13)$$

$$s_{\text{pooled}} = \sqrt{\frac{1}{N} \cdot \frac{\sum_{k=1}^{N}(1/s_{\text{sample }k}^{2}) \cdot \sum_{k=1}^{N}[(\bar{x}_{\text{sample }k} - \bar{x}_{\text{pooled}})^{2} \cdot (1/s_{\text{sample }k}^{2})]}{[\sum_{k=1}^{N}(1/s_{\text{sample }k}^{2})]^{2} - \sum_{k=1}^{N}(1/s_{\text{sample }k}^{2})^{2}}} \qquad (14)$$

where N is the number of repetitive analyses. The pooled sample standard error quantifies how close $\bar{x}_{\text{pooled}}$ is to the true value through t-distribution (degree of freedom = $N - 1$, or normal distribution when N is sufficiently large), and $\bar{x}_{\text{pooled}} \pm 2 \cdot s_{\text{pooled}}$ approximately represents a 95% confidence interval of the true isotopic ratio of the sample.

The consistency of the pooled repetitive analyses of the same sample can be evaluated using the weighted mean square weighted deviation (MSWD, also known as the reduced χ^2 statistic, see Appendix F for details):

$$\text{MSWD} = \frac{\sum_{k=1}^{N}(1/s_{\text{sample }k}^{2}) \cdot \sum_{k=1}^{N} \frac{(\bar{x}_{\text{sample }k} - \bar{x}_{\text{pooled}})^{2} \cdot (1/s_{\text{sample }k}^{2})}{s_{\text{sample }k}^{2}}}{[\sum_{k=1}^{N}(1/s_{\text{sample }k}^{2})]^{2} - \sum_{k=1}^{N}(1/s_{\text{sample }k}^{2})^{2}} \qquad (15)$$

Through the probability density function given by Wendt and Carl (1991), MSWD quantifies how well the standard deviation of the repetitive analyses of the same sample (i.e., external precision) is estimated by the standard errors of individual analyses (i.e., internal precision). MSWD should be close to 1 if the individual standard errors are compatible with the observed scatter of the repetitively measured samples. An MSWD value greater than $1 + 2(2/f)^{1/2}$ (where $f = N - 1$ is the degree of freedom) indicates that the individual standard errors (i.e., internal precision) have underestimated the standard deviation of the repetitive analyses (i.e., external precision) at >95% confidence level, which possibly reflects changes in analytical conditions unaccounted for by the individual standard errors. In contrast, a too low MSWD [e.g., $0 < \mathrm{MSWD} < 1 - 2(2/f)^{1/2}$] indicates that the individual standard errors may be too high.

A.4 Calculation of sample average fractionation rate

The rate of instrumental mass fractionation during measurement was monitored and evaluated using the block average $^{88}\mathrm{Sr}/^{86}\mathrm{Sr}$ ratios measured at line 1. The instantaneous fractionation rate at block (k+1) (k = 1, 2, …, N–1, where N is the number of blocks in the measurement) was calculated as:

$$r_{\text{block}\,(k+1)} = \frac{\dfrac{(^{88}\mathrm{Sr}/^{86}\mathrm{Sr})_{\text{block}\,(k+1)} - (^{88}\mathrm{Sr}/^{86}\mathrm{Sr})_{\text{block}\,k}}{(^{88}\mathrm{Sr}/^{86}\mathrm{Sr})_{\text{block}\,(k+1)}} \cdot 100\%}{2\ \text{amu} \cdot 1\ \text{block}} \quad (16)$$

where $(^{88}\mathrm{Sr}/^{86}\mathrm{Sr})_{\text{block}\,(k+1)}$ and $(^{88}\mathrm{Sr}/^{86}\mathrm{Sr})_{\text{block}\,k}$ are the block average $(^{88}\mathrm{Sr}/^{86}\mathrm{Sr})_{\text{line 1}}$ ratios of the (k+1)th and the kth blocks of the measurement; $r_{\text{block}\,(k+1)}$ has an unit of %/block/amu (amu = atomic mass unit). The average fractionation rate of a measurement was estimated by averaging the instantaneous fractionation rates of all N–1 blocks. Given that the average duration of one block is ca. 450 s in our measurements (considering the time used for switching between run 1 and run 2, baseline measurement, peak centring, lens focusing, inter-blocking heating, etc.), a fractionation rate of 0.045 %/block/amu approximately translates to 1 ppm/s/amu:

$$r(\text{ppm/s/amu}) = \frac{r(\text{\%/block/amu})}{0.045} \quad (17)$$

Appendix B. Comments on the cycle number used in fractionation interpolation

During TIMS measurement, the change of the measured (i.e., raw) ^{88}Sr/^{86}Sr ratio along with time is a combination of two phenomena: fractionation drift, a relatively slow change that can be reasonably well approximated by the linear model at the time scale of several cycles (i.e., several minutes), and noise, a much faster change at time scale of seconds with frequent reversals of the direction of change (see Fig. 6 of Garçon et al., 2018). The effects of noise and non-linear evolution of fractionation can make the linear fractionation interpolation method applied less accurate, i.e., make the interpolated ^{88}Sr/^{86}Sr value deviating from the true value. Noises will mainly increase the scatter of drift-corrected isotopic ratio and lead to larger uncertainty, but are unlikely to generate systematic biases. However, non-linear evolution of fractionation can introduce systematic biases, and lead to under-correction or over-correction of fractionation drift depending on the curvature of the sample's real fractionation–time trajectory. Interpolation using a small number of cycles ensures a good local linearity in the interpolated interval, but can be more strongly affected by noises; in the opposite, using a large number of cycles is less affected by noises, but is more sensitive to the linearity of fractionation in the interpolated interval. For samples with higher fractionation rates (e.g., Sr samples in this study), the fractionation monitoring isotopic ratio changes rapidly due to fractionation drift, so that the contribution from noises is less significant, while the linearity in the interpolation interval is critical. In this case, a small cycle number is preferred. For samples with lower fractionation rates and more stable fractionation–time evolution trajectories (e.g., Nd samples in the studies of radiogenic ^{142}Nd effects), fractionation has better linearity at longer time scales, while noises become the dominant source of inaccuracy in interpolation. In this case, a larger cycle number is required.

We tested interpolation with more consecutive cycles considered, using the local linear regression method similar to that described by Garçon et al. (2018). One example is shown in Fig. S1 below. With increasing cycle number in the interpolation, the MDFI ^{84}Sr/^{86}Sr value increases, suggesting under-correction induced by non-linear fractionation evolution. This is consistent with the convex shape of the fractionation–time trajectory of this sample (Fig. S1). Our applied interpolation method with 2 cycles involved is, thus, minimally affected by the systematic biases caused by non-linear fractionation evolution. The uncertainties of the drift-corrected values shown in Fig. S1 are all similar, suggesting that the values corrected using small cycle numbers are also not significantly affected by noises.

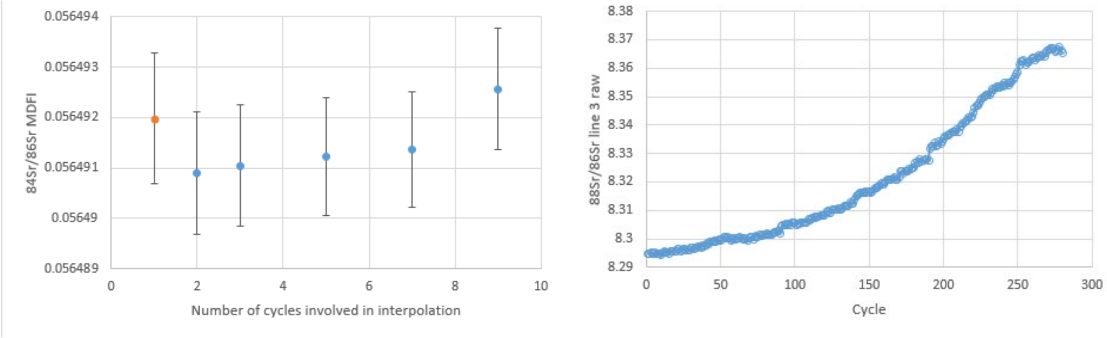

Figure S1. Left: multidynamic ^{84}Sr/^{86}Sr values of a SRM 987 measurement, calculated with different fractionation interpolation methods. The orange dot is the value not corrected for fractionation drift. Blue dots are values corrected for fractionation drift using 2, 3, 5, 7, and 9 consecutive cycles for interpolation. Right: raw ^{88}Sr/^{86}Sr ratio measured in line 3 vs. cycle of the same measured sample.

Appendix C. Chemically processed standard SRM 987

In order to test (1) whether the chemical separation procedures described in section 2 cause variations in Sr isotopic ratios, and (2) whether organic residues from chemical processing are responsible for the observed high fractionation rates of terrestrial samples (Fig. 2), the Sr standard SRM 987 was processed in the same way as the terrestrial samples, and was analysed in a separate analytical session in 2021. Between the 2019 and 2021 Sr isotope analytical sessions, our TIMS instrument experienced maintenances including cup changes, and was used for Nd and Pb isotope analyses. Since the status of the instrument and measurement conditions may have changed, the new analyses of column-processed SRM 987 were bracketed by analyses of unprocessed SRM 987. The μ^{84}Sr and μ^{87}Sr values of each column-processed standard were calculated relative to the average values of the two analyses of the unprocessed standard that bracket it.

The analytical results are shown in Fig. S2. The column-processed SRM 987 standard exhibits no difference in μ^{84}Sr and μ^{87}Sr values from the unprocessed standard under the analytical uncertainties. This is as expected given the high (>95%) chemical yield of our Sr separation procedure, and ensures that no isotopic anomaly is generated by chemical processing. In addition, the fractionation rates of column-processed SRM 987 analyses fall into the range of unprocessed SRM 987, and are not significantly elevated. This result, though derived from a relatively small number (4) of tests on column-processed SRM 987, suggests that the high fractionation rates seen in the analyses of terrestrial samples are more likely linked to residual matrix elements in the samples rather than organic materials.

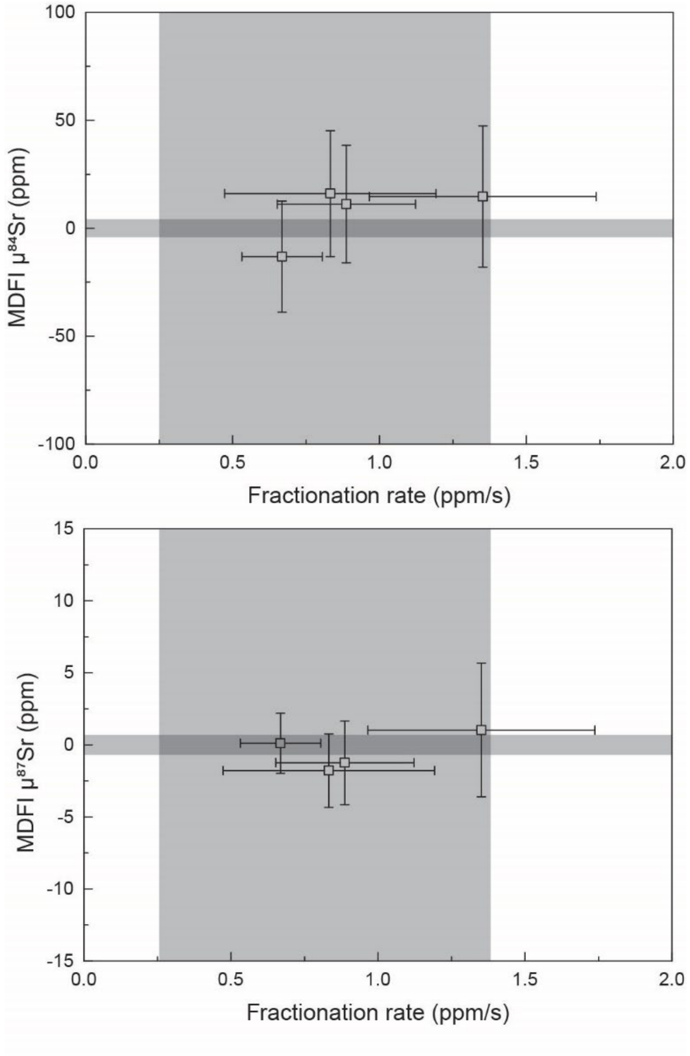

Figure S2. MDFI μ^{84}Sr and μ^{87}Sr values vs. fractionation rate of column-processed SRM 987. Uncertainties are 2SE. Grey horizontal bars represent the 2SE confidence intervals of the weighted average μ^{84}Sr or μ^{87}Sr value of unprocessed SRM 987 (from the 2019 analytical session). Grey vertical bars represent the 2SD ranges of fractionation rates of the unprocessed SRM 987.

Appendix D. Ion counting statistics model

During the measurements of ion beam intensities using Faraday cups–amplifiers, random errors are produced by two major sources: Poisson noise and Johnson–Nyquist (JN) noise. When a large number of ions are counted, the measured ion beam intensity fluctuates randomly due to these noises, following normal distributions with standard deviations predicted by (Wielandt and Bizzarro, 2011; Makishima, 2016):

$$\delta V_{\mathrm{Poisson}} = \sqrt{\frac{VRe}{t}} \quad (18)$$

$$\delta V_{\mathrm{JN}} = \sqrt{\frac{4k_B RT}{t}} \quad (19)$$

and the total fluctuation from the two noises is:

$$\delta V_{\mathrm{total}} = \sqrt{\frac{VRe + 4k_B RT}{t}} \quad (20)$$

where δV is the standard deviation of ion beam intensity induced by the noises (V), V is the ion beam intensity (V), R is the resistor value (10^{11} Ω here), e is the elementary charge (1.602×10^{-19} C), k_{B} is the Boltzmann constant (1.3806×10^{-23} J/K), T is the temperature (311. 15 K here), and t is the integration time (s).

We modelled the error correlations caused by ion counting statistics between the MDFI μ^{87}Sr and μ^{84}Sr, and between the static line 1 μ^{87}Sr and μ^{84}Sr, using a method similar to Andreasen and Sharma (2009) and Garçon et al. (2018). In the modelling, the weighted average MDFI ^{84}Sr/^{86}Sr and ^{87}Sr/^{86}Sr values (Tables 2 and 3 in the main text), and ^{88}Sr/^{86}Sr = 8.375209 were assumed as the true isotopic compositions of SRM 987. Sr was assumed to evaporate from a homogeneous reservoir, and the isotope fractionation during evaporation was fixed at ^{88}Sr/^{86}Sr = 8.375209. A constant ^{88}Sr intensity of 18 V was set, which is the average of all our actual SRM 987 measurements. The intensities of other Sr isotopes were calculated accordingly. Faraday cup efficiencies and amplifier gains were assumed to be equal in the modelling. In each simulated measurement run, the integration time of each isotope in each multidynamic line was 8.389 s multiplied by 340, the average cycle number per measurement in our actual measurements. Independent, normally-distributed random errors with standard deviations predicted by the Poisson and JN noises (equation 20) were then assigned to the ^{84}Sr, ^{86}Sr, ^{87}Sr, and ^{88}Sr intensities of the three multidynamic lines. Isotopic ratios were calculated in the same ways as in the actual measurements (Appendix A). The geometric mean of the two multidynamic ^{87}Sr/^{86}Sr ratios (i.e., MCFI–C) was taken as the MDFI ^{87}Sr/^{86}Sr result.

Fig. S3 shows the μ^{87}Sr and μ^{84}Sr results of 1000 simulated SRM 987 measurement runs. These results represent the theoretical precision and error correlation of μ^{87}Sr and μ^{84}Sr under our measurement conditions. For both the MDFI and static line 1 simulated data, μ^{87}Sr and μ^{84}Sr exhibit slightly positive correlations with linearly fitted slopes of 0.014 ± 0.008 and 0.035 ± 0.013 respectively (uncertainties are 2SE). The simulated MDFI and static measurements yield similar μ^{84}Sr precision of ca. 20 ppm (2SD). However, the static simulations show a stronger correlation between μ^{87}Sr and μ^{84}Sr and a worse μ^{87}Sr precision compared to the MDFI simulations. This is not surprising given that the calculation equations of multidynamic isotopic ratios involve more independently measured ion beam intensities, and that the MDFI ^{87}Sr/^{86}Sr was calculated as the geometric mean of two multidynamic ^{87}Sr/^{86}Sr ratios.

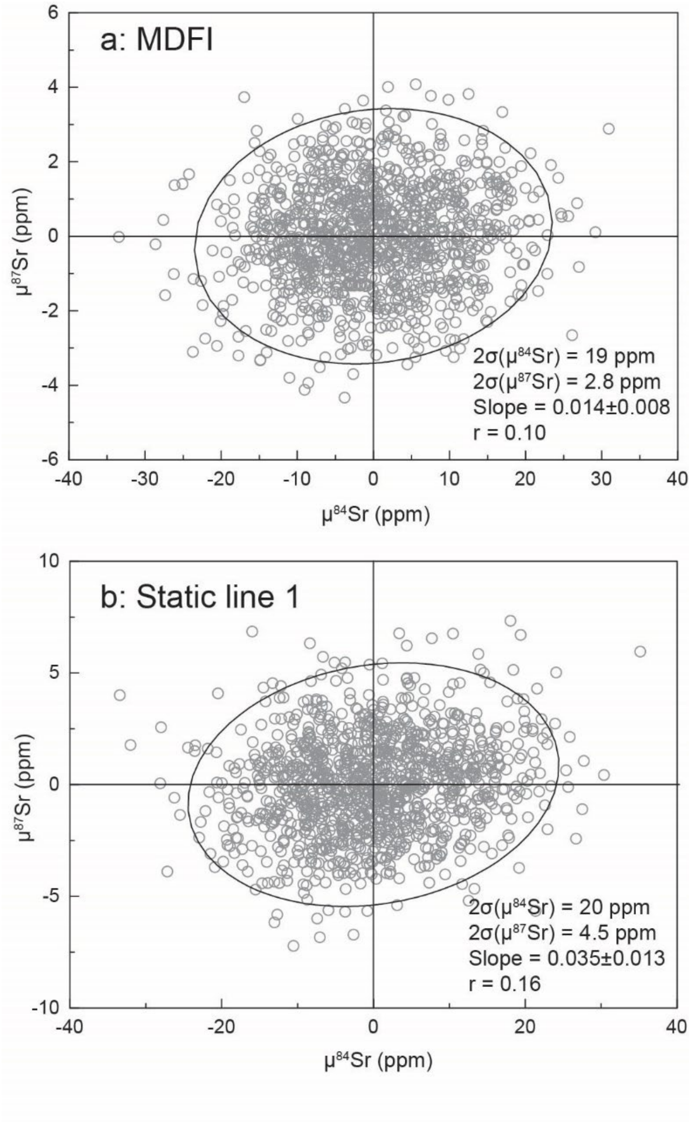

Figure S3. Correlations between (a) MDFI and (b) static (line 1) μ^{87}Sr and μ^{84}Sr values of 1000 repetitive SRM 987 measurements simulated using the ion counting statistics model. The 95% envelope ellipses of the simulated data are generated and plotted. The linearly fitted slopes of the simulated data (with their 2SE uncertainties) and correlation coefficients (r) are also shown. Theoretical 2SD precisions of μ^{87}Sr and μ^{84}Sr caused by the ion counting random errors are calculated using the simulated measurements.

Appendix E. Comments on "normalization" of isotopic data and selection of standard

The convention of reporting the radiogenic ^{87}Sr isotopic variations in the geo- and cosmochemistry community is using the ^{87}Sr/^{86}Sr ratio, rather than ε- or μ-notation. This is possibly a result of the large ^{87}Sr variation range in nature caused by the large chemical property (e.g., volatility, compatibility) contrast between Rb and Sr, and thus no object being eligible as a universal isotopic composition "baseline" (cf. Chondritic Uniform Reservoir for ^{143}Nd/^{144}Nd, Jacobsen and Wasserburg, 1980). As shown in the main text and in the literature, systematic errors can be introduced into the measured isotopic ratios during TIMS analyses. As a consequence, the evaluation of the absolute isotopic ratios of the same materials measured using different instruments by different laboratories, or using the same instrument but at different times or with different methods, would not be the same. These systematic errors arise from the subtle but numerous imperfections of features specific to laboratory, instrument, and the measurement and data processing protocols, including, but not limited to the position and geometry of the magnet, the tuning of the electrostatic and magnetic optic system, collector and amplifier gains, and stabilities of electronic devices. Due to the unavoidability of these small imperfections, more attention is paid to the reproducibility (precision) of the measurement results, rather than the absolute accuracy of isotopic ratios.

The systematic biases between laboratories become significant when studying small (e.g., ppm-level) isotopic variations in samples. For this reason, when comparing high-precision isotopic ratio data generated by different laboratories, it is important to ensure that the inter-laboratory biases in isotopic ratios are accounted for. A common way to eliminate systematic errors is to normalize the measured sample isotopic ratios using a simultaneously analysed standard (see section 4.4). The standard can be a natural or artificial material, but should have good isotope homogeneity and should be widely accepted by laboratories (for a full list of requirements for standard materials, see Teng et al., 2017). If the same standard material is analysed by two laboratories, and the results of unknown samples from both laboratories are normalized to the same "accepted" value of the standard, the two sets of normalized sample data are directly comparable. The assumption behind such normalization is that systematic errors affect all measurement results proportionally disregarding their different absolute isotopic ratios, i.e., if the isotopic ratio of a standard measured by the instrument A is higher (or lower) than the same standard measured by the instrument B by a factor of $1 + \varepsilon$, the contemporaneously measured isotopic ratio of an unknown sample by the instrument A should also be higher (or lower) by a factor of $1 + \varepsilon$ when the same sample is analysed by the instrument B. The "accepted" standard value need not accurately reflect the true isotopic composition of the standard, and it varies in literature. Therefore, we suggest that high-precision isotope data are reported in both normalized and unnormalized form, together with the analytical results of standards.

The ^{84}Sr (and a number of other isotopes) isotopic variations in extra-terrestrial samples are usually reported as ε- or μ-values relative to terrestrial standards which usually represent the bulk silicate Earth (BSE) composition. However, our data confirm that the Sr standard NIST SRM 987 possesses an apparent μ^{84}Sr enrichment of ca. 30 ppm relative to natural terrestrial samples (Moynier et al., 2012; Paton et al., 2013; Yokoyama et al., 2015). Previous investigations on stable Sr isotope fractionation found that SRM 987 has been isotopically fractionated in nature or during its production, and that the BSE has a δ^{88}Sr value of +0.27‰ with regard to SRM 987 (Moynier et al., 2010; Charlier et al., 2012). Similar mass-dependent and mass-independent stable isotopic composition differences between standards used in isotopic analyses and the BSE composition have been discovered in Nd (O'Neil et al., 2008), Ni (Steele et al., 2011), Mg (Bizzarro et al., 2011), and Cr (Qin et al., 2010) standards. Since these purified standards do not possess the same mass-independent isotopic composition as the BSE (i.e., $\mu_{\mathrm{Earth}} \neq 0$), concerns may arise during the isotope analyses of extra-terrestrial materials over whether another natural terrestrial sample, which better represents the BSE composition, should be used as the standard instead. We agree with Steele et al. (2011) that this is not necessary. The purpose of normalizing isotopic ratios against a standard is mainly to cancel out systematic errors in the measurements and to make accurate inter-laboratory comparison. The isotopic composition of a standard serves as an arbitrary reference point and need not be accurately related to specific isotope reservoirs. Therefore, it is more important for the standard material to have a homogeneous isotopic composition and wide availability, rather than an isotopic composition close to the BSE.

Appendix F. Hypothesis test and confidence interval

(Equations in this Appendix are not numbered, as it is unnecessary.)

F.1 Univariate hypothesis test and confidence interval

Assume X is a normally distributed random variable: $X \sim N(\mu, \sigma^2)$, where μ and σ^2 represent the population mean and variance. Given a sample of size n, μ and σ^2 can be estimated by $\overline{X}$ (sample mean) and s^2 (sample variance):

$$\bar{X} = \frac{1}{n} \cdot \sum_{i=1}^{n} X_i$$

$$s^2 = \frac{1}{n-1} \cdot \sum_{i=1}^{n} (X_i - \bar{X})^2$$

It can be proved that $\overline{X}$ has a normal distribution: $\overline{X} \sim N(\mu, \sigma^2/n)$. The quantity $\sqrt{s^2}$ is also known as the sample standard deviation (SD) and $\sqrt{s^2/n}$ is the sample standard error of the mean (SE or SEM). The question being concerned here is how well the sample mean $\overline{X}$ estimates the unknown population mean μ.

If σ^2 is known, the random variable

$$\eta = \frac{\bar{X} - \mu}{\sqrt{\frac{\sigma^2}{n}}}$$

has the standard normal distribution $N(0, 1)$. Under a given confidence level $1 - \alpha$ (usually $\alpha = 0.05$), let $\eta_{\text{crit},\alpha}$ be the critical η where the probability of $|\eta| \leq \eta_{\text{crit},\alpha}$ is $1 - \alpha$. For standard normal distribution with $\alpha = 0.05$, $\eta_{\text{crit}} \approx 1.96$. If infinitely many repeated samples (size = n) are taken, a fraction of $1 - \alpha$ of the samples would satisfy

$$|\eta| \leq \eta_{\text{crit},\alpha}$$

$$\Leftrightarrow \bar{X} - \eta_{\mathrm{crit},\alpha} \cdot \sqrt{\frac{\sigma^2}{n}} \le \mu \le \bar{X} + \eta_{\mathrm{crit},\alpha} \cdot \sqrt{\frac{\sigma^2}{n}}$$

The above inequation can be equivalently expressed as: the population mean is contained within the interval $\bar{X} \pm \eta_{\mathrm{crit},\alpha} \cdot \sqrt{\frac{\sigma^2}{n}}$. For a given sample, this interval is called the 1 – α confidence interval of the population mean. Note again that the meaning of the confidence interval is that when infinitely many repeated samples (size = n) are taken and the 1 – α confidence interval are computed for each sample, a fraction of 1 – α of those confidence intervals would contain the population mean. However, it does not necessarily mean that for a given confidence interval, there is a 1 – α probability that the population mean lies within the interval.

To test if the sample mean $\bar{X}$ is compatible with a hypothesized population mean μ_0, we can test the null hypothesis: $\mu = \mu_0$. Under the null hypothesis, if the calculated $|\eta| > \eta_{\mathrm{crit},\alpha}$, an event with a small probability (α) would have occurred, and the null hypothesis should be rejected: $\mu \neq \mu_0$.

If σ^2 is unknown, it can be substituted by the sample variance s^2. In this case, the statistic

$$t = \frac{\bar{X} - \mu}{\sqrt{\frac{s^2}{n}}}$$

has the t-distribution with $n - 1$ degrees of freedom:

$$p_{n-1}(t) = \frac{\Gamma\left(\frac{n}{2}\right)}{\sqrt{(n-1)\pi} \cdot \Gamma\left(\frac{n-1}{2}\right)} (1 + \frac{t^2}{n-1})^{-\frac{n}{2}}$$

Similarly, under a given confidence level 1 – α, we can find the critical $t_{\mathrm{crit},\alpha,n-1}$ where the probability of $|t| \le t_{\mathrm{crit},\alpha,n-1}$ is 1 – α. The 1 – α confidence interval of μ can then be computed as:

$$\bar{X} - t_{\text{crit},\alpha,n-1} \cdot \sqrt{\frac{s^2}{n}} \le \mu \le \bar{X} + t_{\text{crit},\alpha,n-1} \cdot \sqrt{\frac{s^2}{n}}$$

When $n \rightarrow \infty$, the *t*-distribution is reduced to the standard normal distribution, and $t_{\text{crit},\alpha,n-1} \rightarrow 1.96$ when $\alpha = 0.05$. Therefore, the sample mean ± 2 standard error (2SE) is usually accepted as a 95% confidence interval of the population mean, and 2SE is used as the measurement uncertainty. It should be noted, however, that the correspondence between 2SE and 95% confidence interval is valid only when n is sufficiently large ($n \rightarrow \infty$). When the sample size n is small, the 95% confidence interval of the population mean should be generated using the above method following the *t*-distribution.

Given the null hypothesis: $\mu = \mu_0$, if the calculated $|t| > t_{\text{crit},\alpha,n-1}$, an event with a small probability (α) would have occurred, and the null hypothesis should be rejected: $\mu \neq \mu_0$. The above hypothesis test is also known as the Student's *t* test.

The statistic

$$\chi^2 = \frac{(n-1)s^2}{\sigma^2}$$

has the χ^2 (chi-squared) distribution with $n - 1$ degrees of freedom:

$$p_{n\text{-}1}(\chi^2) = \begin{cases} \dfrac{1}{2^{\frac{n-1}{2}} \cdot \Gamma\left(\frac{n-1}{2}\right)} (\chi^2)^{\frac{n-3}{2}} e^{-\frac{\chi^2}{2}}, & \chi^2 > 0 \\ 0, & \chi^2 \le 0 \end{cases}$$

The probability density function of the reduced χ^2 statistic, MSWD = χ^2/f where f is the degree of freedom, has been given by Wendt and Carl (1991). The statistic MSWD has an expectation of 1, so it is more perceptual when comparing samples with different sizes compared to the χ^2 statistic which has an expectation of $n - 1$. Under a given confidence level $1 - \alpha$, we can find the critical $\text{MSWD}_{\text{crit},\alpha,n-1}$ where the probability of $\text{MSWD} \le \text{MSWD}_{\text{crit},\alpha,n-1}$ is $1 - \alpha$. Given the null hypothesis $\sigma^2 \le \sigma_0^2$, if the calculated $\text{MSWD} > \text{MSWD}_{\text{crit},\alpha,n-1}$, an event with a small probability (α) would have occurred, and the null hypothesis should be rejected:

$\sigma^2 > \sigma_0^2$. The high MSWD suggests that the observed sample is more scattered than what was predicted using the hypothesized population variance.

F.2 Multivariate hypothesis test and confidence region

When determining the confidence intervals or carrying out hypothesis tests for *k*-dimension multivariate random vectors, it is tempting to separately calculate confidence intervals or perform individual *t*-tests for each variable as in the univariate case. The overall null hypothesis is then rejected if any one of the *k* univariate tests rejects its null hypothesis. The problem of this method, however, is that if the same reject probability α is used in all *k* tests, the probability of multivariate null hypothesis being rejected becomes $1 - (1 - \alpha)^k$, which is much higher than α. For this reason, a corrected reject probability $\alpha' = 1 - (1 - \alpha)^{1/k}$ should be used in the *k* individual univariate tests instead of α. However, this correction is only reliable when the *k* random variables are independent so that probabilities can be simply multiplied. Since it is common to generate observations in which the random variables x_i in $\boldsymbol{X}$ are not independent, it is better to calculate 1 – α confidence regions and carry out multivariate hypothesis tests with all the *k* variables taken into account simultaneously.

Assume $\boldsymbol{X} = [x_1, x_2, \ldots, x_k]^T$ is a $k \times 1$ random vector having the multivariate normal distribution $\mathcal{N}(\boldsymbol{\mu}, \boldsymbol{\Sigma})$:

$$p(\boldsymbol{x}) = \frac{1}{(2\pi)^{\frac{k}{2}}|\boldsymbol{\Sigma}|^{\frac{1}{2}}} e^{-\frac{1}{2}(\boldsymbol{x}-\boldsymbol{\mu})^T\boldsymbol{\Sigma}^{-1}(\boldsymbol{x}-\boldsymbol{\mu})}$$

where $\boldsymbol{\mu}$ is the $k \times 1$ population mean vector and $\boldsymbol{\Sigma}$ the $k \times k$ population covariance matrix. For a sample of size *n*, $\boldsymbol{\mu}$ and $\boldsymbol{\Sigma}$ can be estimated by $\overline{\boldsymbol{X}}$ (sample mean vector) and $\boldsymbol{S}$ (sample covariance matrix):

$$\overline{\boldsymbol{X}} = \frac{1}{n} \cdot \sum_{i=1}^{n} \boldsymbol{X}_i$$

$$\boldsymbol{S} = \frac{1}{n-1} \cdot \sum_{i=1}^{n} (\boldsymbol{X}_i - \overline{\boldsymbol{X}})(\boldsymbol{X}_i - \overline{\boldsymbol{X}})^T$$

It can be proved that $\bar{\boldsymbol{X}}$ has a multivariate normal distribution $\mathcal{N}(\boldsymbol{\mu}, \boldsymbol{\Sigma}/n)$. The question being concerned here, again, is how well the sample mean $\bar{\boldsymbol{X}}$ estimates the population mean $\boldsymbol{\mu}$.

If $\boldsymbol{\Sigma}$ is known, the statistic

$$y = n(\bar{\boldsymbol{X}} - \boldsymbol{\mu})^T \boldsymbol{\Sigma}^{-1} (\bar{\boldsymbol{X}} - \boldsymbol{\mu})$$

has the χ^2 distribution with k degrees of freedom. Under a given confidence level $1 - \alpha$, we can find $y_{\text{crit},\alpha,k}$ where the probability of $y \leq y_{\text{crit},\alpha,k}$ is $1 - \alpha$. If infinitely many repeated samples (size = n) are taken, a fraction of $1 - \alpha$ of the samples would satisfy

$$n(\bar{\boldsymbol{X}} - \boldsymbol{\mu})^T \boldsymbol{\Sigma}^{-1} (\bar{\boldsymbol{X}} - \boldsymbol{\mu}) \leq y_{\text{crit},\alpha,k}$$

In the 2-dimentional case $\bar{\boldsymbol{X}} = \begin{bmatrix} \bar{x}_1 \\ \bar{x}_2 \end{bmatrix}$ and $\boldsymbol{\mu} = \begin{bmatrix} \mu_1 \\ \mu_2 \end{bmatrix}$, the above inequation can be rewritten as:

$$[\bar{x}_1 - \mu_1 \quad \bar{x}_2 - \mu_2] \begin{bmatrix} a & b \\ c & d \end{bmatrix} \begin{bmatrix} \bar{x}_1 - \mu_1 \\ \bar{x}_2 - \mu_2 \end{bmatrix} \leq \frac{y_{\text{crit},\alpha,k}}{n}$$

$$\Leftrightarrow a(\bar{x}_1 - \mu_1)^2 + (b + c)(\bar{x}_1 - \mu_1)(\bar{x}_2 - \mu_2) + d(\bar{x}_2 - \mu_2)^2 \leq \frac{y_{\text{crit},\alpha,k}}{n}$$

where $\begin{bmatrix} a & b \\ c & d \end{bmatrix}$ represents $\boldsymbol{\Sigma}^{-1}$. The above inequation can be equivalently expressed as: in the x_1–x_2 space, the point representing the population mean (μ_1, μ_2) is contained within the ellipse region defined by

$$a(x_1 - \bar{x}_1)^2 + (b + c)(x_1 - \bar{x}_1)(x_2 - \bar{x}_2) + d(x_2 - \bar{x}_2)^2 = \frac{y_{\text{crit},\alpha,k}}{n}$$

$$\Leftrightarrow \begin{cases} x_1 = \begin{cases} \bar{x}_1 + \sqrt{\dfrac{\frac{y_{\text{crit},\alpha,k}}{n}}{a + (b + c)\tan\theta + d\tan^2\theta}}, & \theta \in (-\frac{\pi}{2}, \frac{\pi}{2}) \\ \bar{x}_1 - \sqrt{\dfrac{\frac{y_{\text{crit},\alpha,k}}{n}}{a + (b + c)\tan\theta + d\tan^2\theta}}, & \theta \in (\frac{\pi}{2}, \frac{3\pi}{2}) \end{cases} \\ x_2 = \bar{x}_2 + (x_1 - \bar{x}_1)\tan\theta, \qquad \theta \in (-\frac{\pi}{2}, \frac{\pi}{2}) \cup (\frac{\pi}{2}, \frac{3\pi}{2}) \end{cases}$$

For a given sample, this ellipse is called the $1 - \alpha$ confidence ellipse of the population mean. Similar to the 1-dimentional confidence interval, if infinitely many repeated samples (size = n) are taken, and the $1 - \alpha$ confidence ellipses are computed for each sample, a fraction of $1 - \alpha$

of those ellipses would contain the population mean. Note that a confidence ellipse *does not* contain 1 – α fraction of the observations in a sample (cf. envelope ellipse in section 3). In the case of higher dimensions ($k > 2$), the confidence region is a k-dimension hyper-ellipsoid.

Given the null hypothesis: $\boldsymbol{\mu} = \boldsymbol{\mu}_0$, if the calculated $y > y_{\mathrm{crit},\alpha,k}$, an event with a small probability (α) would have occurred, and the null hypothesis should be rejected: $\boldsymbol{\mu} \neq \boldsymbol{\mu}_0$.

If $\boldsymbol{\Sigma}$ is unknown, it can be substituted by the sample covariance matrix $\boldsymbol{S}$. In this case, the statistic T^2 is defined as:

$$T^2 = n(\overline{\boldsymbol{X}} - \boldsymbol{\mu})^T \boldsymbol{S}^{-1} (\overline{\boldsymbol{X}} - \boldsymbol{\mu})$$

and the statistic

$$F = \frac{(n-k)}{k(n-1)} T^2$$

has the F-distribution with the degrees of freedom of (k, $n - k$). Note that the F-distribution can be regarded as the ratio of two reduced χ^2 distribution, or the squared t-distribution. When $n \to \infty$, the F-distribution is reduced to the reduced χ^2 (MSWD) distribution. Under the given confidence level 1 – α, we can find $F_{\mathrm{crit},\alpha,k,n-k}$ where the probability of $F \leq F_{\mathrm{crit},\alpha,k,n-k}$ is 1 – α. The 1 – α confidence ellipse of $\boldsymbol{\mu}$ can then be computed by:

$$\frac{n(n-k)}{k(n-1)} (\overline{\boldsymbol{X}} - \boldsymbol{\mu})^T \boldsymbol{S}^{-1} (\overline{\boldsymbol{X}} - \boldsymbol{\mu}) \leq F_{\mathrm{crit},\alpha,k,n-k}$$

Given the null hypothesis: $\boldsymbol{\mu} = \boldsymbol{\mu}_0$, if the calculated $F > F_{\mathrm{crit},\alpha,k,n-k}$, an event with a small probability (α) would have occurred, and the null hypothesis should be rejected: $\boldsymbol{\mu} \neq \boldsymbol{\mu}_0$. The above hypothesis test in the 2-demensional case is also known as the Hotelling's T^2 test, a 2-dimensional extension of the Student's t test.

F.3 Covariance matrix, envelope ellipse, and linear fitting

An observed 2-dimensional sample dataset (x_1, x_2) may show correlation between the two variables x_1 and x_2 due to their non-zero covariance ($\sigma_{x_1 x_2}$). This correlation can be described using either an envelope ellipse derived from the covariance matrix of the observed data, or a straight line fitted using the least-square (LSQ) method. Here we will show that the major axis of the envelope ellipse usually does not overlap the conventional LSQ straight line fitted using *vertical offsets* (Fig. S4a). For simplicity, here we assume that the sample size $n \to \infty$ and there is no difference between the sample and population mean or covariance matrix.

For a random vector $\boldsymbol{X}$ with a 2-dinensional normal distribution $\mathcal{N}(\boldsymbol{\mu}, \boldsymbol{\Sigma})$, the statistic

$$y = (\boldsymbol{X} - \boldsymbol{\mu})^T \boldsymbol{\Sigma}^{-1} (\boldsymbol{X} - \boldsymbol{\mu})$$

has the χ^2 distribution with 2 degrees of freedom. Let $y_{\text{crit},\alpha,2}$ be the critical y value when the probability of $y \leq y_{\text{crit},\alpha,2}$ is $1 - \alpha$. For a sample of $\boldsymbol{X}$ (size $n \to \infty$), a fraction of $1 - \alpha$ of the observations should satisfy

$$(\boldsymbol{X} - \boldsymbol{\mu})^T \boldsymbol{\Sigma}^{-1} (\boldsymbol{X} - \boldsymbol{\mu}) \leq y_{\text{crit},\alpha,2}$$

From the distribution function of χ^2 distribution (degree of freedom = 2), when $\alpha = 0.05$, $y_{\text{crit},\alpha,2} \approx 5.99$. In other words, the ellipse

$$(\boldsymbol{X} - \boldsymbol{\mu})^T \boldsymbol{\Sigma}^{-1} (\boldsymbol{X} - \boldsymbol{\mu}) = 5.99$$

$$\Leftrightarrow a(x_1 - \mu_1)^2 + (b + c)(x_1 - \mu_1)(x_2 - \mu_2) + d(x_2 - \mu_2)^2 = 5.99$$

should cover 95% of the observations in the sample (Fig. S4b). Here $\begin{bmatrix} a & b \\ c & d \end{bmatrix} = \boldsymbol{\Sigma}^{-1} = \frac{1}{|\boldsymbol{\Sigma}|} \begin{bmatrix} \sigma_{x_2x_2} & -\sigma_{x_1x_2} \\ -\sigma_{x_2x_1} & \sigma_{x_1x_1} \end{bmatrix}$, while the covariance matrix $\boldsymbol{\Sigma} = \begin{bmatrix} \sigma_{x_1x_1} & \sigma_{x_1x_2} \\ \sigma_{x_2x_1} & \sigma_{x_2x_2} \end{bmatrix}$. This ellipse is called 95% envelope ellipse. Note that the 95% envelope ellipse and the 95% confidence ellipse (see section 2) have similar expressions, but differ in size by a factor of n (sample size, or number of observations). When $n \to \infty$, the 95% confidence ellipse is infinitely close to the point representing the population mean, but the 95% envelope ellipse is unchanged. Since the envelope ellipse is statistically generated using the covariance matrix, the direction of the ellipse major axis naturally represents the correlation trend of the two variables. When $b, c \neq 0$, (i.e., when the two variables x_1 and x_2 are correlated), the major axis of the envelope ellipse deviates from the positive x_1-axis with an angle ϕ (Fig. S4b). The slope of the ellipse major axis, tanϕ, can be calculated from the ellipse equation:

$$\tan\phi = \begin{cases} -\dfrac{a-d}{b+c} + \sqrt{\left(\dfrac{a-d}{b+c}\right)^2 + 1}, & b, c > 0 \\ -\dfrac{a-d}{b+c} - \sqrt{\left(\dfrac{a-d}{b+c}\right)^2 + 1}, & b, c < 0 \end{cases}$$

On the other hand, if the observed data are linearly fitted using the conventional LSQ method that minimizes the sum of the squares of the *vertical offsets* from data points to the line (e.g., York et al., 2004), the slope of the fitted line is given by:

$$\text{slope} = \frac{\sigma_{x_1x_2}}{\sigma_{x_1x_1}} = -\frac{b}{d}$$

It can be proved that when plotted together with the envelope ellipse (Fig. S4b), this fitted line connects the two points on the ellipse that are *horizontally* farthest from the ellipse centre, not the two ellipse vertices. Also, the slope of this fitted line is usually unequal to the slope of the ellipse major axis (tanϕ) and has a smaller absolute value. The two lines overlap when b, $c = 0$, $a < d$ (i.e., $r^2 = 0$, when the two variables are not correlated, and the ellipse is longer in the horizontal direction) or when $bc = ad$ (i.e., $r^2 = 1$, when the envelope ellipse reduces to a straight line). The fitted line and the ellipse major axis become significantly apart when the square of the correlation coefficient $[r^2 = \frac{(\sigma_{x_1x_2})^2}{\sigma_{x_1x_1}\cdot\sigma_{x_2x_2}}]$ deviates from 1 (Fig. S4c), and they becaome perpendicular when b, $c = 0$, $a > d$ (i.e., $r^2 = 0$, when the two variables are not correlated, and the ellipse is longer in the vertical direction). In contrast, if another straight line is fitted for the data using the LSQ method that minimizes the sum of the squares of *perpendicular offsets* (Fig. S4a) from the data points to the line (e.g., Sampaio, 2006; Sardelis and Valahas, 2019; Johansen, 2016; Weisstein, 2002), this fitted line will overlap the ellipse major axis.

The limitations of the conventional LSQ fitting method using vertical offsets have been examplified by Johansen (2016). The major argument is that in the conventional LSQ fitting, the statuses of the independent (x_1) and the dependent (x_2) variables are asymmetric, so that the fitted line is not consistent in rotation or invertion operations. Furthermore, our Fig. S4 shows that the slope of the conventional LSQ-fitted line does not provide an accurate description of the correlation trend of the data when they have a correlated 2-dimensional normal distribution; it underestimates the absolute value of the correlation slope when the squared correlation coefficient is small. The direction of the ellipse major axis, or the perpendicular offset-fitted line, can synthesize the random deviations in both horizontal and vertical directions, and provide a better description of this correlation.

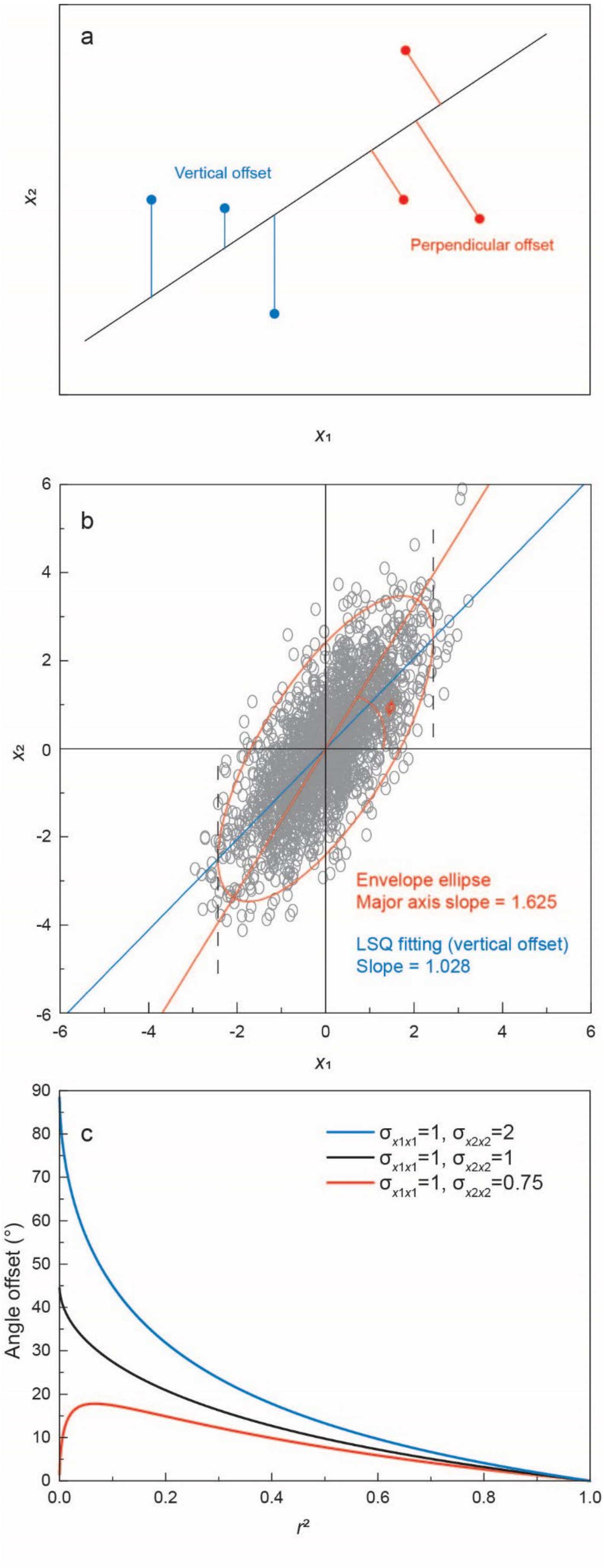
a
Vertical offset
Perpendicular offset
x_2
x_1
b
Envelope ellipse
Major axis slope = 1.625
LSQ fitting (vertical offset)
Slope = 1.028
θ
x_2
x_1
6
4
2
0
-2
-4
-6
-6
-4
-2
0
2
4
6
c
σ_{x1x1}=1, σ_{x2x2}=2
σ_{x1x1}=1, σ_{x2x2}=1
σ_{x1x1}=1, σ_{x2x2}=0.75
Angle offset (°)
r^2
90
80
70
60
50
40
30
20
10
0
0.0
0.2
0.4
0.6
0.8
1.0

Figure S4. Illustrations of the relation between linear fitting and envelope ellipse. (a) the difference between *vertical offset* and *perpendicular offset* from data points to a line, which are used in different least square (LSQ) fitting methods. (b) 2000 randomly generated data points following a correlated 2-dimensional normal distribution with mean values at (0, 0). Red ellipse is the 95% envelope ellipse of the data generated using the covariance matrix; red line is the direction of the ellipse major axis; blue line is the straight line fitted using the LSQ method that minimizes the sum of the squares of the vertical distances from the data points to the line; black dashed lines show that the LSQ-fitted line connects the two points on the ellipse that are horizontally farthest from the ellipse centre. Note the offset between the ellipse major axis and the LSQ-fitted line. (c) Relation between the angle offset of the two lines (i.e., the angle of ellipse major axis with the positive x_1-axis minus the angle of LSQ-fitted line with the positive x_1-axis) and the square of correlation coefficient. Three different scenarios with different x_1 variances ($\sigma_{x_1x_1}$) and x_2 variances ($\sigma_{x_2x_2}$) are shown. Only the cases where b, $c > 0$ (i.e., x_1 and x_2 are positively correlated) are considered here.

References

Andreasen, R., Sharma, M., 2009. Fractionation and mixing in a thermal ionization mass spectrometer source: Implications and limitations for high-precision Nd isotope analyses. International Journal of Mass Spectrometry, 285(1): 49-57.

Bizzarro, M., Paton, C., Larsen, K., Schiller, M., Trinquier, A., Ulfbeck, D., 2011. High-precision Mg-isotope measurements of terrestrial and extraterrestrial material by HR-MC-ICPMS—implications for the relative and absolute Mg-isotope composition of the bulk silicate Earth. Journal of Analytical Atomic Spectrometry, 26(3): 565-577.

Carlson, R.W., 2014. 15.18 - Thermal Ionization Mass Spectrometry. In: Holland, H.D., Turekian, K.K. (Eds.), Treatise on Geochemistry (Second Edition). Elsevier, Oxford, pp. 337-354.

Caro, G., Bourdon, B., Birck, J.-L., Moorbath, S., 2006. High-precision ^{142}Nd/^{144}Nd measurements in terrestrial rocks: Constraints on the early differentiation of the Earth's mantle. Geochimica et Cosmochimica Acta, 70(1): 164-191.

Charlier, B.L.A., Nowell, G.M., Parkinson, I.J., Kelley, S.P., Pearson, D.G., Burton, K.W., 2012. High temperature strontium stable isotope behaviour in the early solar system and planetary bodies. Earth and Planetary Science Letters, 329: 31-40.

Fukai, R., Yokoyama, T., Kagami, S., 2017. Evaluation of the long-term fluctuation in isotope ratios measured by TIMS with the static, dynamic, and multistatic methods: A case study for Nd isotope measurements. International Journal of Mass Spectrometry, 414: 1-7.

Garçon, M., Boyet, M., Carlson, R.W., Horan, M.F., Auclair, D., Mock, T.D., 2018. Factors influencing the precision and accuracy of Nd isotope measurements by thermal ionization mass spectrometry. Chemical Geology, 476: 493-514.

Hans, U., Kleine, T., Bourdon, B., 2013. Rb-Sr chronology of volatile depletion in differentiated protoplanets: BABI, ADOR and ALL revisited. Earth and Planetary Science Letters, 374: 204-214.

Holden, N.E., Coplen, T.B., Böhlke, J.K., Tarbox, L.V., Benefield, J., R., d.L.J., Mahaffy, P.G., O'Connor, G., Roth, E., Tepper, D.H., Walczyk, T., Wieser, M.E., Yoneda, S., 2018. IUPAC Periodic Table of the Elements and Isotopes (IPTEI) for the Education Community (IUPAC Technical Report). Pure and Applied Chemistry, 90(12): 1833-2092.

Jacobsen, S.B., Wasserburg, G.J., 1980. Sm-Nd isotopic evolution of chondrites. Earth and Planetary Science Letters, 50(1): 139-155.

Johansen, C., 2016. Least Squares Fitting - Perpendicular Offsets, http://claus-jo.dk/LeastSquaresFittingPerpendicularOffsets.html#t2.

Makishima, A., 2016. Thermal Ionization Mass Spectrometry (TIMS): Silicate Digestion, Separation, and Measurement. John Wiley & Sons, Weinheim, Germany.

Moynier, F., Agranier, A., Hezel, D.C., Bouvier, A., 2010. Sr stable isotope composition of Earth, the Moon, Mars, Vesta and meteorites. Earth and Planetary Science Letters, 300(3-4): 359-366.

Moynier, F., Day, J.M.D., Okui, W., Yokoyama, T., Bouvier, A., Walker, R.J., Podosek, F.A., 2012. Planetary-scale strontium isotopic heterogeneity and the age of volatile depletion of early Solar System materials. Astrophysical Journal, 758(1): 45.

O'Neil, J., Carlson, R.W., Francis, D., Stevenson, R.K., 2008. Neodymium-142 Evidence for Hadean Mafic Crust. Science, 321(5897): 1828.

Paton, C., Schiller, M., Bizzarro, M., 2013. Identification of an Sr-84-depleted carrier in primitive meteorites and implications for thermal processing in the solar protoplanetary disk. Astrophysical Journal Letters, 763(2): L40.

Qin, L., Alexander, C.M.O.D., Carlson, R.W., Horan, M.F., Yokoyama, T., 2010. Contributors to chromium isotope variation of meteorites. Geochimica et Cosmochimica Acta, 74(3): 1122-1145.

Sampaio, J.H.B., 2006. An iterative procedure for perpendicular offsets linear least squares fitting with extension to multiple linear regression. Applied Mathematics and Computation, 176(1): 91-98.

Sardelis, D., Valahas, T., 2019. Least Squares Fitting-Perpendicular Offsets, https://www.researchgate.net/publication/315069657_Least_Squares_Fitting-Perpendicular_Offsets.

Steele, R.C.J., Elliott, T., Coath, C.D., Regelous, M., 2011. Confirmation of mass-independent Ni isotopic variability in iron meteorites. Geochimica et Cosmochimica Acta, 75(24): 7906-7925.

Teng, F.-Z., Dauphas, N., Watkins, J.M., 2017. Non-Traditional Stable Isotopes: Retrospective and Prospective. Reviews in Mineralogy and Geochemistry, 82(1): 1-26.

Thirlwall, M.F., 1991. Long-term reproducibility of multicollector Sr and Nd isotope ratio analysis. Chemical Geology: Isotope Geoscience section, 94(2): 85-104.

Trinquier, A., Birck, J.-L., Allègre, C.J., 2008. High-precision analysis of chromium isotopes in terrestrial and meteorite samples by thermal ionization mass spectrometry. Journal of Analytical Atomic Spectrometry, 23(12): 1565-1574.

Upadhyay, D., Scherer, E.E., Mezger, K., 2008. Fractionation and mixing of Nd isotopes during thermal ionization mass spectrometry: implications for high precision 142Nd/144Nd analyses. Journal of Analytical Atomic Spectrometry, 23(4): 561-568.

Weisstein, E.W., 2002. Least Squares Fitting--Perpendicular Offsets, https://mathworld.wolfram.com/LeastSquaresFittingPerpendicularOffsets.html.

Wendt, I., Carl, C., 1991. The statistical distribution of the mean squared weighted deviation. Chemical Geology: Isotope Geoscience section, 86(4): 275-285.

Wendt, I., Haase, G., 1998. Dynamic double collector measurement with cup efficiency factor determination. Chemical Geology, 146(1): 99-110.

Wielandt, D., Bizzarro, M., 2011. A TIMS-based method for the high precision measurements of the three-isotope potassium composition of small samples. Journal of Analytical Atomic Spectrometry, 26(2): 366-377.

Yobregat, E., Fitoussi, C., Bourdon, B., 2017. A new method for TIMS high precision analysis of Ba and Sr isotopes for cosmochemical studies. Journal of Analytical Atomic Spectrometry, 32(7): 1388-1399.

Yokoyama, T., Fukami, Y., Okui, W., Ito, N., Yamazaki, H., 2015. Nucleosynthetic strontium isotope anomalies in carbonaceous chondrites. Earth and Planetary Science Letters, 416: 46-55.

York, D., Evensen, N.M., Martínez, M.L., De Basabe Delgado, J., 2004. Unified equations for the slope, intercept, and standard errors of the best straight line. American Journal of Physics, 72(3): 367-375.